Gillis, K., Mével, C., Allan, J., et al., 1993
Proceedings of the Ocean Drilling Program, Initial Reports, Vol. 147

3. SITE 894[1]

Shipboard Scientific Party[2]

HOLE 894A

Date occupied: 3 December 1992

Date departed: 4 December 1992

Time on hole: 23 hr, 00 min

Position: 2°18.030′N, 101°31.490′W

Bottom felt (rig floor, m; drill-pipe measurement): 3023.0

Distance between rig floor and sea level (m): 10.9

Water depth (drill-pipe measurement from sea level, m): 3012.1

Total depth (rig floor, m): 3029.0

Penetration (m): 6.0

Number of cores (including cores with no recovery): 1

Total length of cored section (m): 6.0

Total core recovered (m): 6.2

Core recovery (%): 104

Oldest sediment cored:
Depth (mbsf): 6.0
Nature: foraminifer-bearing igneous lithic breccia

Comments: Camera survey; test hole.

HOLE 894B

Date occupied: 4 December 1992

Date departed: 5 December 1992

Time on hole: 1 day, 00 hr, 15 min

Position: 2°17.960′N, 101°31.564′W

Bottom felt (rig floor, m; drill pipe measurement): 3031.0

Distance between rig floor and sea level (m): 10.9

Water depth (drill pipe measurement from sea level, m): 3020.1

Total depth (rig floor, m): 3038.0

Penetration (m): 7.0

Number of cores (including cores with no recovery): 1

Total length of cored section (m): 7.0

Total core recovered (m): 0.1

Core recovery (%): 2

Igneous section:
Depth top (m): 0.0
Depth bottom (m): 7.0
Nature: gabbro

Comments: Test hole; camera survey; Scripps OBS recovered.

HOLE 894C

Date occupied: 5 December 1992

Date departed: 6 December 1992

Time on hole: 1 day, 8 hr, 15 min

Position: 2°17.952′N, 101°31.545′W

Bottom felt (rig floor, m; drill pipe measurement): 3044.0

Distance between rig floor and sea level (m): 10.9

Water depth (drill pipe measurement from sea level, m): 3033.1

Total depth (rig floor, m): 3075.0

Penetration (m): 31.0

Number of cores (including cores with no recovery): 1

Total length of cored section (m): 31.0

Total core recovered (m): 0.2

Core recovery (%): 0

Comments: Lost guide base, broken drill collar; camera survey. Samples collected (gabbro) represent bit recovery and are not cored.

HOLE 894D

Date occupied: 6 December 1992

Date departed: 7 December 1992

Time on hole: 17 hr, 30 min

Position: 2°18.091′N, 101°31.590′W

Bottom felt (rig floor, m; drill pipe measurement): 3024.0

Distance between rig floor and sea level (m): 10.9

Water depth (drill pipe measurement from sea level, m): 3013.1

Total depth (rig floor, m): 3043.5

Penetration (m): 19.5

Number of cores (including cores with no recovery): 2

Total length of cored section (m): 19.5

Total core recovered (m): 1.5

Core recovery (%): 7

Oldest sediment cored:
Depth (mbsf): 10.0
Nature: nannofossil foraminifer sand and clay-bearing foraminifer nannofossil ooze

Igneous section:
Depth top (m) 10.0
Depth bottom (m): 19.5
Nature: basalt

Comments: Test hole; camera survey.

HOLE 894E

Date occupied: 6 December 1992

---

[1] Gillis, K., Mével, C., Allan, J., et al., 1993. *Proc. ODP, Init. Repts.*, 147: College Station, TX (Ocean Drilling Program).

[2] Shipboard Scientific Party is as given in the list of participants preceding the contents.

Date departed: 7 December 1992

Time on hole: 1 day, 13 hr, 45 min

Position: 2°18.059′N, 101°31.526′W

Bottom felt (rig floor, m; drill pipe measurement): 3024.6

Distance between rig floor and sea level (m): 10.9

Water depth (drill pipe measurement from sea level, m): 3013.7

Total depth (rig floor, m): 3053.3

Penetration (m): 28.7

Number of cores (including cores with no recovery): 3

Total length of cored section (m): 28.7

Total core recovered (m): 3.0

Core recovery (%): 10

Oldest sediment cored:
Depth (mbsf): 9.3
Nature: foraminifer sand, foraminifer nannofossil ooze, basaltic sand, and breccia

Igneous section:
Depth top (m): 9.3
Depth bottom (m): 28.7
Nature: basalt, gabbro

Comments: Test hole; camera survey.

HOLE 894F

Date occupied: 7 December 1992

Date departed: 8 December 1992

Time on hole: 23 hr, 45 min

Position: 2°17.977′N, 101°31.555′W

Bottom felt (rig floor, m; drill pipe measurement): 3035.5

Distance between rig floor and sea level (m): 10.9

Water depth (drill pipe measurement from sea level, m): 3024.6

Total depth (rig floor, m): 3061.2

Penetration (m): 25.7

Number of cores (including cores with no recovery): 3

Total length of cored section (m): 25.7

Total core recovered (m): 1.8

Core recovery (%): 7

Igneous section:
Depth top (m): 0.0
Depth bottom (m): 25.7
Nature: basalt, gabbro

Comments: Test hole.

HOLE 894G

Date occupied: 8 December 1992

Date departed: 30 December 1992

Time on hole: 21 days, 10 hr

Position: 2°17.977′N, 101°31.555′W

Bottom felt (rig floor, m; drill pipe measurement): 3034.4

Distance between rig floor and sea level (m): 11.0

Water depth (drill pipe measurement from sea level, m): 3023.4

Total depth (rig floor, m): 3188.9

Penetration (m): 154.5

Number of cores (including cores with no recovery): 20

Total length of cored section (m): 127.5

Total core recovered (m): 45.8

Core recovery (%): 35

Igneous section:
Depth top (m): 0.0
Depth bottom (m): 154.5
Nature: gabbronorite, basalt, olivine gabbronorite, olivine gabbro, gabbro

Comments: Drilled: 27.0 m, cored: 127.5 m, recovered: 45.1 m, wash core recovered: 0.6 m.

Principal results: Site 894 is located close to the summit of the intrarift ridge in Hess Deep, at approximately 2°18.0′N, 101°31.5′W. The objective of drilling at Site 894 was to sample a section of oceanic gabbros created at a fast-spreading mid-ocean ridge, by starting a hole directly on gabbros exposed at the top of the ridge.

Six camera surveys were conducted at this site, covering a total area of 1.0 x 1.2 km, and seven sites were selected for test drilling to locate appropriate rock types and optimal drilling conditions. Shallow holes were drilled on the flat, slightly sedimented summit of the ridge (Holes 894A, 894D, 894E) and on ledges close to the southern edge of the summit (Holes 894B, 894F). An attempt to start Hole 894C with a hard-rock guide base failed. A second hard-rock guide base was successfully deployed to start Hole 894G, close to test Hole 894F.

Holes 894A, 894D, and 894E recovered short sections of sediment consisting of foraminiferal ooze, basalt cobbles, basaltic lithic breccias, basaltic sand, and foraminiferal sand. The basaltic and foraminiferal sand is interpreted as turbidites that may have been deposited in a basin, before the uplift of the intrarift ridge. In Hole 894A, this formation overlies a monomict igneous breccia consisting of basaltic fragments altered to greenschist facies assemblages, which are interpreted as being locally derived. Highly metamorphosed gabbro fragments, many of which are cataclastically deformed, were recovered in Holes 894B, 894E, and 894F.

As Holes 894F and 894G are only 18 m apart, their stratigraphy is considered together. The igneous plutonic rocks recovered at Holes 894F and 894G, in order of decreasing abundance, are gabbronorite, gabbro, olivine gabbro and gabbronorite, and oxide gabbro and gabbronorite. The gabbros occur in the upper parts of the section, and gabbronorites first appear at 45 mbsf. These plutonic rocks are nonlayered, showing textural variations from ophitic to equigranular and grain size variations from fine- to coarse-grained. Some of the textural variability is related to the presence of patches, pockets, and veins of more coarse-grained gabbronorite hosted in finer-grained gabbros and gabbronorites. Zircon and apatite are abundant in many of these coarser-grained pockets. The lack of layering, the textural variability, and the presence of coarse-grained pockets in the recovered rocks are most similar to gabbroic rocks found in the upper parts of many plutonic sequences of ophiolite complexes.

Although layering is not apparent, magmatic penetrative fabrics are defined by the preferred orientation of euhedral plagioclase in many of the plutonics. A steeply dipping, magmatic foliation defined by mineral alignment is regularly present, and the trend of the lineations is subvertical. In fine-grained gabbros, the foliation is oblique to, and crosscut by, coarser-grained gabbronorite, which exhibits an irregularly distributed steeply dipping fabric. Although most medium-grained gabbronorites possess orthopyroxene oikocrysts, these noticeably disappear where a strong magmatic foliation is developed. This feature suggests that the foliation may have formed as a result of deformation of partly crystallized magma, and that deformation locally played a role in expelling evolved interstitial liquid.

Several units of basalt were recovered at Site 894. In two cases, the basalts are olivine, plagioclase, and spinel phyric and represent dikes chilled against the plutonic rocks. The other occurrences represent volcanic rocks that may be associated with Cocos-Nazca rifting.

At least 80% of the rocks recovered at Site 894 are moderately altered to greenschist to amphibolite facies mineral assemblages. The metamorphism and associated vein formation observed in the Site 894 plutonics require the migration of hydrothermal fluids through the gabbros from

>500°C to ambient temperatures. The extent of alteration increases with increasing grain size and does not correlate with depth (mbsf). Metamorphic textures consist of pseudomorphic replacement of primary igneous minerals. Amphibolite facies mineral assemblages define the earliest alteration and include amphibole, metamorphic clinopyroxene, magnetite, and secondary plagioclase. These minerals are overgrown by transition to the amphibolite and greenschist-facies mineral assemblages dominated by actinolite, minor sodic plagioclase, and rare chlorite. The latest alteration includes replacement of plagioclase by zeolites and of clinopyroxene, orthopyroxene, and olivine by smectite.

Several networks of filled tensile fractures that are devoid of displacement crosscut the Site 894 core. Cataclastic zones occur primarily in the upper part of the section and are related to steeply dipping normal faults. Three types of macroscopic veins (≥0.1 mm wide) postdate the early amphibolite facies mineral assemblages. The earliest veins range from continuous and sharp-sided to discontinuous and wispy and are filled primarily by green amphibole. Associated minerals may include pale brown amphibole, chlorite, and sphene. A second set of veins forms a much more regular, abundant, steeply dipping (40°–60°) network associated with strong greenschist facies wall-rock alteration, and contains chlorite with varying amounts of prehnite, actinolite, and epidote. Reorientation of this vein network relative to the stable remanent magnetization direction indicates a consistent west–northwest to east–southeast trend that is parallel to the Hess Deep rift valley. These veins and associated wall-rock alteration also occur near zones of cataclastic deformation. The youngest veins are filled by assemblages of layer silicates (chlorite to smectite), zeolites, and calcite. Veins of this type exhibit a wide range of dips and are associated with variable wall-rock alteration.

Paleomagnetic measurements show that the average intensity of natural remanent magnetization and magnetic susceptibility of samples from Hole 894G are 2.0 A/m and 0.016 SI units, respectively. The ratio of these two parameters suggests that the in-situ magnetization of this crustal section is dominated by remanent magnetization, rather than magnetization induced by the Earth's field. Overall, these magnetic property values are similar to those observed on gabbros recovered from slow-spreading ridges as well as on most oceanic basalts. The remanent magnetization is observed to be very stable with respect to both alternating field and thermal demagnetization, and the demagnetization data indicate that nearly pure magnetite is the only significant carrier of remanence. The stable direction of magnetization dips downward at an average of 40° and is significantly different from the value expected for crust formed at this latitude (0°). Therefore, it seems likely that this crustal section experienced substantial tectonic rotation.

Physical properties are strongly dependent on the intensity of metamorphism. The average wet-bulk density is 2.92 g/cm^3 ± 0.09 g/cm^3. Porosity values center on a mean value of 1.2%, whereas the water content mean value is 0.4%. The most altered samples have the lowest densities and highest porosities. Compressional-wave velocities measured at atmospheric pressures and temperatures in horizontally oriented, water-saturated samples have a mean of 6600 m/s ± 500 m/s, with values ranging from 5330 m/s in the most altered zones to 7335 m/s for the freshest rocks. Velocities measured in several vertical samples do not show any significant anisotropy relative to adjacent horizontal samples. Thermal conductivity measurements have a mean value of 2.22 W/m°C. Thermal conductivity increases from fine-grained dikes through altered gabbro to fresher gabbronorites. Separating the measurements by intensity of metamorphism shows that the heat flux through altered zones is mostly controlled by convective rather than conductive heat flow. Electrical resistivity measurements performed in several water-saturated minicores show a strong inverse correlation with porosity, which suggests that ionic pore fluid conduction dominates in these samples. Values ranging from 10,700 Ωm to 19.8 Ωm fall within values previously measured for these types of oceanic rock.

OPERATIONS

Leg 147 of the Ocean Drilling Program began at 0745 local time (L), 1545 Universal Time Coordinated (UTC), on 22 November 1992, with the first mooring line at San Diego harbor, California. After the completion of port call activities, the ship got under way at 1700L, 25 November 1992, (0100UTC, 26 November). The sea voyage from San Diego to Hess Deep covered 2034 nmi in 178 hr at 11.4 knots average.

Because of the rugged topography and the poor results from existing sea surface seismic surveys at this site, no seismic survey was run. A beacon was dropped on Global Positioning System (GPS) coordinates for Site 894, as determined from the SeaBeam bathymetric map, at 1045UTC, 3 December 1992. The beacon landed close to the ridge summit at 2°18.040'N, 101°31.569'W.

Site 894 is located on the summit of the intrarift ridge, on whose flanks gabbro outcrops were observed during *Nautile* dives. With the subsea camera deployed on the drill string, six surveys were conducted along the flat-lying summit from 3 to 11 December 1992 to select potential sites for deployment of a hard-rock guide base (HRB). The drill string was run with a 9-7/8-in. rotary core barrel (RCB) bit and bottom-hole assembly (BHA) so spot coring could be conducted as required during the survey. An area of 1000 m (north–south) by 1220 m (east–west) was surveyed with a total track line length of 13.4 km (Fig. 1). Positions were determined using an X (north) and Y (east) grid by calculating the position of the ship relative to the beacon and the vibration isolation tool (VIT) frame (used to mount the video camera) relative to the ship. A GPS location for each hole also was determined. Depths were recorded during the survey by the drill string length at touch downs or by adding the camera frame winch wire length, depth from bottom determined from the subsea sonar, and a factor that accounts for the difference in length between the drill string and the winch wire. During the surveys, the morphology of the seafloor was recorded, including the distribution of outcrop and talus and the slope of the terrain. Punch tests were conducted periodically to determine the competency of outcrops and sediment thickness. When a potential site was found, a test spud-in was performed to test the lithology and drilling conditions.

Part way through these surveys, a discrepancy was noted between the GPS fix and the X–Y coordinates for these test holes such that the GPS position was offset ~60 m southeast of the X–Y position. Comparison of the depths recorded during the survey with the bathymetric map indicated that the GPS positions were correct and that the beacon location was incorrect. Shifting the X–Y map by this offset allowed a better, although not perfect, consistency in the bathymetry between the SeaBeam map and the depth recorded during the survey.

The water depths recorded during the survey allowed construction of a more accurate bathymetric map of the ridge summit, despite the irregular distribution of data. Figure 2 shows the contours drawn from the measured depths and the SeaBeam map. The data obtained during the surveys show that the summit is actually shallower than indicated by the SeaBeam map (the shallowest depth recorded is 3011 m). The survey data also suggest that the summit has a more triangular shape than indicated by the SeaBeam map, as well as the existence of a ravine on the southern flank. The seven holes drilled at Site 894 are plotted in Figure 2 by GPS coordinates. The GPS and acoustic navigation positions of the holes differ by up to 30 m even after the application of the 60-m shift in the beacon position to remove systematic error. The sediment thicknesses measured are discussed in the "Sediments" section of this chapter.

Along these 13.4 km of survey, no gently dipping unsedimented area was observed. Therefore, we had to deploy the guide base on a sedimented spot.

In this section, time is recorded in UTC and depth in meters below sea level (mbsl).

Survey 1

Survey 1 was conducted from 1736 hr, 3 December 1992, to 0424 hr, 4 December 1992, and covered an area of 600 m (north–south) by 1200 m (east–west). The top of the intrarift ridge was surveyed, starting at the beacon, along 500- to 600-m-long lines trending ~280°. Very

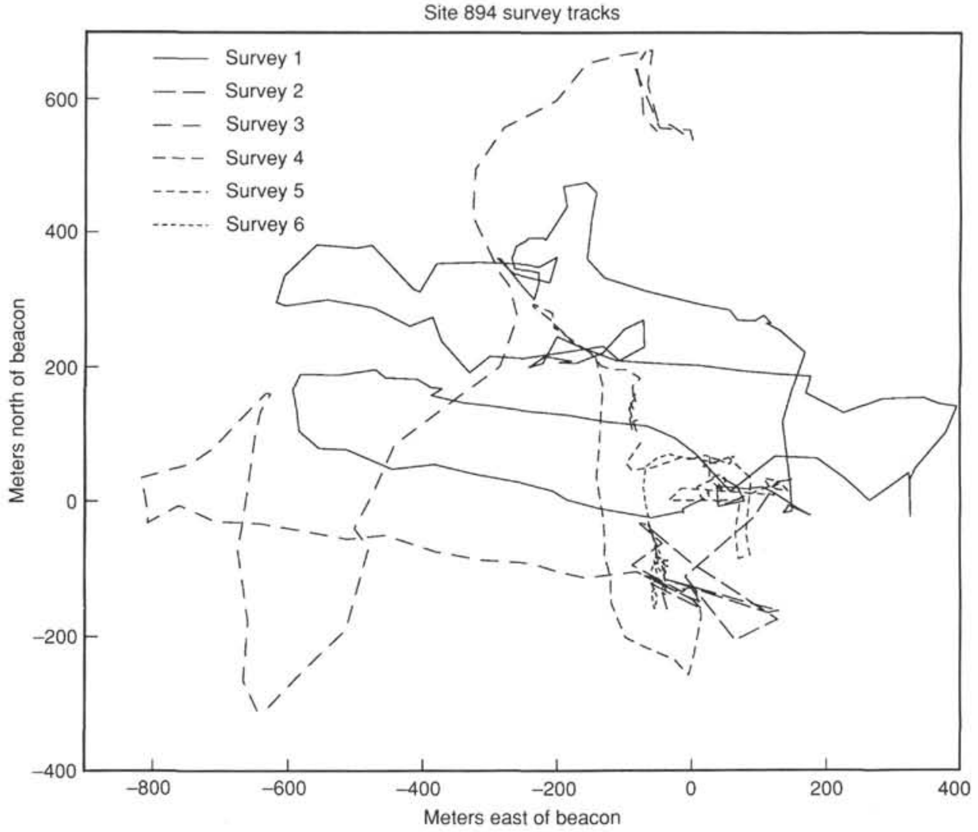

Figure 1. Map of the survey tracks on the summit of the intrarift ridge.

few competent outcrops were observed as the surface was dominantly sediment-covered and had isolated degraded outcrops or talus piles. The talus varied in size from large (1–2 m) blocks to small fragments (centimeter sized). Sediment thickness determined by punch tests was generally thinner (1–3 m) along the southern side of the surveyed area than on the northern side (3–>6 m). However, this thickness likely corresponds only to the light pelagic ooze and does not include rubble piles. Along the eastern side of the survey, a flat-lying ledge above a 1- to 3-m-high ridge was observed at the shallowest part of the survey. Punch tests indicated 1 to 1.5 m of sediment cover. This location was selected for the first test spud-in.

Hole 894A

Hole 894A was spudded at 0645 hr, 4 December 1992, at 2°18.030′N, 101°31.490′W, in 3012 m water depth. The bit was punch cored 2 m and dry cored 2 m in a special effort to recover sediments. Core 147-894A-1R (3012.0–3018.0 mbsl; 0.0–6.0 mbsf) cored 6.0 m and recovered 6.24 m (Table 1) of foraminifer-bearing igneous lithic breccia. The bit cleared the seafloor at 0845 hr, 4 December 1992, ending Hole 894A.

Survey 2

Survey 2 was conducted from 1033 hr to 1200 hr, 4 December 1992. The track extended from Hole 894A to a 230-m (north–south) by 240-m (east–west) area, centered due south of the beacon (Fig. 1). We observed numerous blocky to flat-lying outcrops having a thin sediment cover (<1 m thick) and discontinuous talus trains. A series of gently sloping ledges (<10°–15° south–southwest) is offset by steep scarps that trend approximately east–west. A punch test indicated a sediment thickness of 1 m on one of these gently sloping ledges (<10°–15°), about 15 m north of an east–west trending scarp. A second test spud-in was conducted at this location.

Hole 894B

Hole 894B was spudded at 1330 hr, 4 December 1992, at 2°17.960′N, 101°31.564′W, in 3020.0 m water depth. The bit was punch cored 1.5 m and dry cored 1.5 m to recover sediments. Core 147-894B-1R (3020.0–3027.0 mbsl; 0.0–7.0 mbsf) cored 7.0 m and recovered 0.14 m (two fragments of metamorphosed gabbro) (Table 1). The bit cleared the seafloor at 1500 hr, 4 December, ending Hole 894B. Hole conditions were very good and it was decided that this was an appropriate location to deploy a hard-rock guide base (HRB).

Survey 3 and Scripps OBS Recovery

Survey 3 was conducted from 1641 hr to 1905 hr, 4 December 1992, to investigate the area southwest of the beacon where plutonic rocks were recovered at the end of *Nautile* Dive 5 (see "Geologic and Tectonic Setting" section, "Introduction and Principal Results" chapter, this volume). The area is covered by flat-lying to gently sloping sediment with isolated talus piles and degraded outcrops. Within the southwest corner of the surveyed area, isolated ridges trending east–west with slabby, tabular blocks that dip to the south were observed; these ridges are similar to outcrops in the vicinity of *Nautile* Dive 5. The slope and slabby nature of these outcrops made them inappropriate for drilling. After we concluded that no suitable site would be found in this area, the ship headed northeast at 1905 hr to search for an ocean-bottom seismograph (OBS) belonging to the Scripps Institution of Oceanography that was lost in April 1992 during a site survey for Leg 147. The OBS was reported at 2°18.338′N, 101°31.583′W. The terrain along this transect was predominantly flat-lying sediment

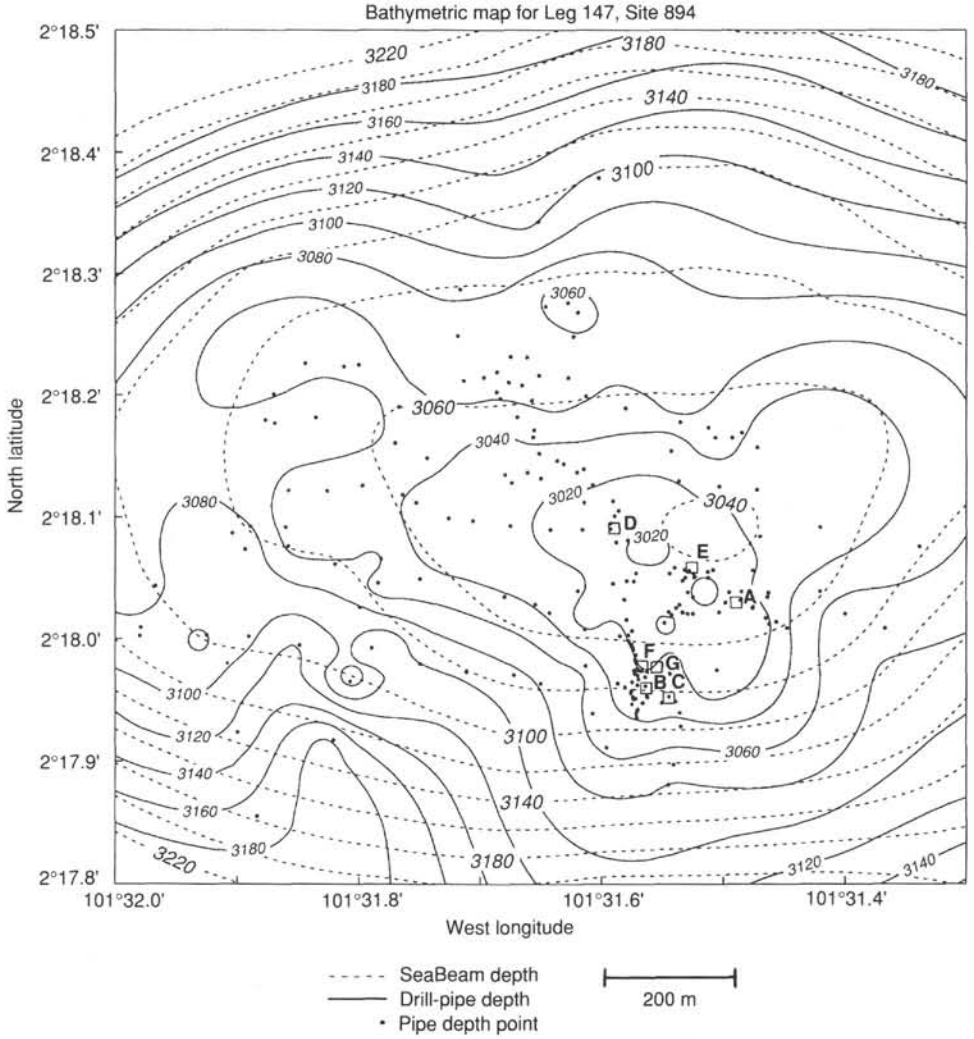

Figure 2. Refined bathymetric map of the intrarift ridge summit obtained from the depth measured during the survey, compared with the SeaBeam bathymetric map (Cruise Report, *Sonne 60,* 12 March 1988–1 January 1989). Bathymetry in meters.

with isolated degraded outcrops and talus piles. After a 30-min search, the OBS was located at 2132 hr, ~575 m due north of the beacon, at 2°18.329′N, 101°31.564′W. The subsea camera frame was pulled, a fishing tool with hooks specially designed for the operation was dropped, and the subsea camera was rerun. After several tries, the OBS was hooked at 0258 hr, 5 December 1992, and successfully brought to the ship with only minimal damage.

Hole 894C

Hole 894B appeared to be the best site for a HRB deployment, so the ship was moved back there during retrieval of the OBS. The HRB was deployed with a 20-in./16-in. Dril-Quip running tool with the cam-actuated drill ahead (CADA) feature. We could not see around the HRB with the TV camera; therefore, the HRB had to be set on bottom at the intended location based on X–Y coordinates from the subsea camera frame and the location of the beacons relative to the ship. After several tries, the HRB was set down with two legs downslope, at a water depth of 3033 m. The tilt beacon, one bullseye tiltmeter, and the cone position indicated that the tilt of the HRB was about 9°, although the general slope of the area seemed to be 15°–20°.

The 20-in./16-in. Dril-Quip running tool and the CADA feature did not permit unlatching for TV surveys and relatching to move the base if necessary. The Dril-Quip running tool was released and the CADA tool unjayed for drilling. Hole 894C was spudded at 0400 hr, 6 December, in 3033 m water depth. The 14-3/4-in. hole was drilled from 3033–3064 mbsl. When we washed to bottom after a wiper trip, the bottom was not found at 3064 mbsl. The subsea camera was run, and the HRB was found lying on its side with obvious sediment slump features above and below. The bit, bit sub assembly, Dril-Quip running tool, CADA tool, and two 8-1/2-in. drill collars were lying downslope to the south. A TV survey showed that the HRB had been set by mistake on a sedimented slope about 60 m east and 20 m downslope from the intended hard-rock ledge of Hole 894B. Circulation while drilling had destabilized the sediment slope, causing it to slump. Probably when the bit was pulled out to the seafloor for a wiper trip, the HRB cone and base tilted further, bowed, and broke the BHA, allowing the HRB to topple over downslope to the south. The HRB appeared to be undamaged, and, therefore, could be salvaged in the future. This event illustrates the difficulty of placing a HRB on a small target because of the uncertainty of acoustic positioning associated with the effects of currents and ship heave on the ship transducer array. Two fragments

Table 1. Coring summary for Site 894, Holes 894A through 894F.

Core	Date (1992)	Time (UTC)	Depth (mbsf)	Length cored (m)	Length recovered (m)	Recovery (%)
147-894A-						
1R	4 Dec.	0815	0.0–6.0	6.0	6.24	104.0
Coring totals				6.0	6.24	104.0
147-894B-						
1R	4 Dec.	1445	0.0–7.0	7.0	0.14	2.0
Coring totals				7.0	0.14	2.0
147-894C-						
1M	4 Dec.	1730	0.0–31.0	31.0	0.17	0.6
Coring totals				31.0	0.17	0.5
147-894D-						
1R	7 Dec.	0635	0.0–10.0	10.0	1.36	13.6
2R	7 Dec.	1040	10.0–19.5	9.5	0.16	1.7
Coring totals				19.5	1.52	7.8
147-894E-						
1R	7 Dec.	2000	0.0–9.3	9.3	2.37	25.5
2R	7 Dec.	2200	9.3–18.9	9.6	0.11	1.1
3R	8 Dec.	0050	18.9–28.7	9.8	0.55	5.6
Coring totals				28.7	3.03	10.6
147-894F-						
1R	8 Dec.	1000	0.0–9.3	9.3	0.34	3.7
2R	8 Dec.	1400	9.3–16.8	7.5	0.45	6.0
3R	8 Dec.	1705	16.8–25.7	8.9	1.01	11.3
Coring totals				25.7	1.80	7.0

of metamorphosed gabbros were found jammed into the broken end of the drill collar, which tagged the seafloor near Hole 894C (Table 1).

Survey 4

Survey 4 was conducted from 0008 hr to 0259 hr, 6 December 1992. The area surrounding Hole 894C was surveyed and a 550 (north–south) by 260 m (east–west) area north of Hole 894C and northwest of Hole 894A was investigated to assess the viability of placing a reentry cone on a flat-lying sedimented area. Except for a few rubble ridges, the whole area appeared sedimented. Punch tests indicated sediment thicknesses of about 5.5 to 6 m.

Hole 894D

Hole 894D was spudded at 0500 hr, 6 December 1992, on a flat, continuously sedimented terrain near the crest of the intrarift ridge summit at 2°18.091′N, 101°31.590′W, in 3013 m water depth. Cores 147-894D-1R to -2R (3013.0–3032.5 mbsl; 0–19.5 mbsf) cored 19.5 m and recovered 1.52 m (Table 1) of nannofossil foraminifer sand and clay-bearing foraminiferal nannofossil ooze. The hole was abandoned because of very unstable drilling conditions, which ruled out the possibility of using a reentry cone.

Survey 5

Survey 5 was conducted from 1238 hr to 1614 hr, 7 December 1992, to investigate a 240 m (north–south) by 180 m (east–west) area centered at the crest of the intrarift ridge between Holes 894A and 894D (Fig. 2). The terrain was similar to that observed during Survey 4 with flat-lying sediment (<5° slope), sediment thickness of 2–3 m, and isolated talus piles. A site was selected on the top of the summit for the fifth test spud-in.

Hole 894E

Hole 894E was spudded at 1815 hr, 7 December 1992, on a flat continuously sedimented terrain at the summit of the intrarift ridge at 2°18.059′N, 101°31.526′W, in 3013.6 m water depth. Cores 147-894E-1R to -3R (3013.6–3042.3 mbsl; 0(28.7 mbsf) cored 28.7 m and recovered 3.03 m (Table 1) of foraminiferal nannofossil ooze, foraminiferal sand, basaltic sand, basaltic lithic breccia, and a fragment of metamorphosed gabbro. The hole was abandoned because of bad drilling conditions (7 m fill), which ruled out the possibility of using a reentry cone.

Survey 6

Survey 6 from 0150 hr to 0530 hr, 8 December, covered a 30-m (north–south) by 130-m (east–west) area southwest of Hole 894E (Fig. 1) to investigate an area that inadvertently had been missed because of the discrepancy in the X–Y grid relative to the GPS position. A ledge about 60 m in length was identified with flat-lying blocky outcrops covered by a 1-m-thick soft sediment layer.

Hole 894F

Hole 894F was spudded at 0730, 8 December, at 2°17.978′N, 101°31.567′W, in 3024.5 m water depth just north and upslope of Hole 894B. Cores 894F-1R to -3R (3024.5–3050.2 mbsl; 0–25.7 mbsf) cored 25.7 m and recovered 1.80 m (Table 1) of deformed, metamorphosed gabbros and oxide-bearing gabbros. As hole conditions were good, we decided to mark the spot precisely for HRB deployment. A commandable release beacon attached to the subsea camera frame was successfully deployed (for the first time from a subsea camera frame) 1 m south of Hole 894F.

Hole 894G

The problem in locating the HRB on Hole 894C led to the decision to use the 20/16-in. Dril-Quip running tool in the run/release/rerun mode (rather than the CADA tool in the drill-ahead mode) so a TV survey could verify the location before committing to a site. After several tries, the HRB was set about 5 m north–northeast of Hole 894F in 3023.4 m water depth, with two legs downslope, at 2°17.977′N, 101°31.555′W. The Dril-Quip running tool released smoothly, and a short TV survey was conducted to verify the location. Leg penetration into the soft sediment was uniformly 1 m. The tilt beacons read 20° and 11°, and the tilt chains read 15° and 5° on the north–south and east–west sides of the HRB, respectively.

Hole 849G was spudded at 0130 hr, 10 December 1992. The 14-3/4-in. hole was drilled without coring in 10.75 hours from 3023.4–3042.0 mbsl (0–18.6 mbsf). Hole conditions were good with no fill on the short trip.

An attempt to case the hole was made with a 17.68-m-long, 13-3/8-in. casing string. The casing stopped on the lip of the hard-rock portion of the hole at 3024.4 m (Fig. 3). It was assumed that the hole was misaligned because of the changing positioning of the ship (because of variable surface currents). The 13-3/8-in. casing was pulled, and the 14-3/4-in. bit was rerun, reentering the HRB at 1745 hr, 11 December 1992. The bit stopped at 3024.4 mbsl and would not reenter the old hole, even though the ship was moved for realignment. The top few meters drilled very hard with high torque and overpull, but the bottom of the hole was clean. The hole was conditioned, and a second attempt was made to run casing. The 13-3/8-in. casing was shortened to 16.67 m so a 12-1/4-in. pilot bit could be extended 0.15 m below the casing. The casing stopped 1.25 m below the top of the hard rock, and attempts to realign the casing, cone throat, and hole by offsetting the ship north, east, south, and west were unsuccessful.

Because it was not possible to run the 13-3/8-in. casing, and because we were unwilling to place the 10-3/4-in. casing at such a shallow depth, we decided to core ahead with a 9-7/8-in. bit to determine deeper hole conditions. The bit tagged fill at 4 mbsf, and the hole was quickly cleaned out to the bottom. Cores 147-894G-1R to -3R (3042.0–3063.0 mbsl; 18.6–39.6 mbsf) cored 21.0 m and recovered 3.85 m of metamorphosed and sheared gabbro with an interval of porphyritic basaltic dike. Drilling conditions were good to 20 mbsf; however, the formation changed to fractured rock below this

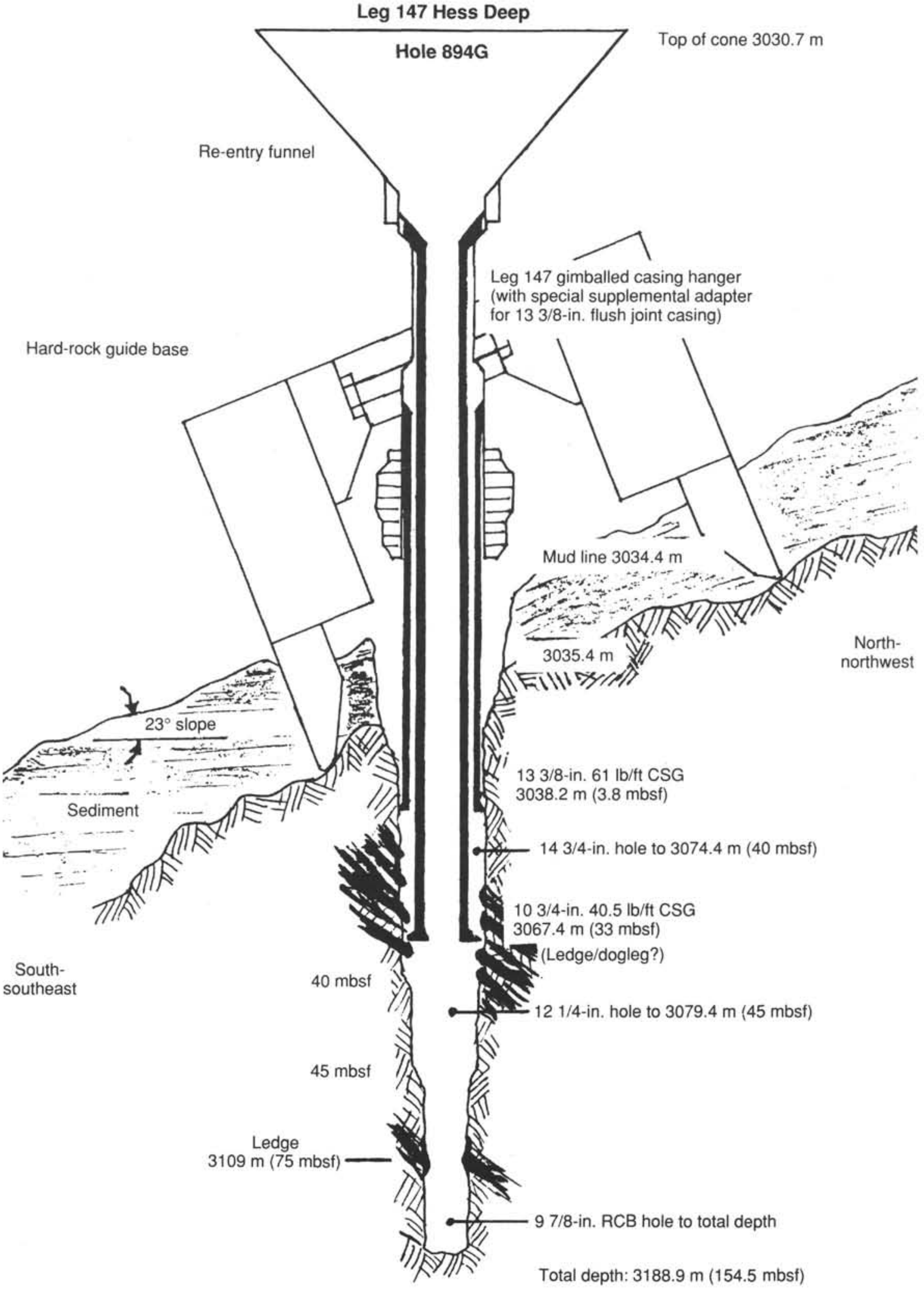

Figure 3. Artist's view of the hard-rock guide base at Hole 894G. Depths are given as mbrf (meters below rig floor). To obtain mbsl (meters below sea level), subtract 11 m.

depth, and drilling conditions deteriorated. Dislodged fragments of fractured gabbro and basalt started falling into the hole (a piece of the wall was recovered in Core 147-894G-3R). The hole was reamed and rereamed for 5.4 hours. Coring was continued; however, 1.4 m into Core 147-894G-3R high torque forced a halt to coring. The unstable hole conditions confirmed the necessity of casing before deepening the hole. A non-concentric hole/cone throat was considered to be the major problem in running the first 13-3/8-in. casing; therefore, the 14-3/4-in. drill bit was rerun with the Dril-Quip CADA running tool. The 14-3/4-in. bit encountered hard drilling conditions for the entire 40 m of hole.

A sediment slump crack 1 m upslope (north) of the HRB had been monitored since drilling commenced and indicated that soft sediment was sloughing downslope as circulation washed out the supporting sediment below. The new 14-3/4-in. hole was open above 3048 m, but had to be drilled out twice to bottom. The hole could only be kept open to 3056 mbsl; therefore, 31 m of 13-3/8-in. casing was spaced out with a 12-1/4-in. bit in an attempt to work the casing to bottom. The casing was worked down with rotation and circulation to 5 mbsf. The casing would go no further, so it was pulled.

A 5.88-m 13-3/8-in. casing was run in an attempt to pin the HRB before trying to clean out the hole for 10-3/4-in. casing. The HRB was reentered at 0135 hr, 17 December 1992, and the casing was landed at 3027.15 mbsl (3.75 mbsf) and released.

A 12-1/4-in. tricone bit was run to clean out the hole from 3045 to 3063 m; however, the persistence of a ledge from 3056–3058 mbsl required repeated reaming before the hole was deepened to 3068.4 mbsl. A 41.56-m 10-3/4-in. casing string was then run with a 12-1/4-in. pilot bit, but it would not pass the ledge at 3056 mbsl despite rotation. The 10-3/4-in. casing was pulled, and 7 m was cut off the casing shoe. The 35.56 m of casing was successfully emplaced at 0600 hr, 18 December 1992. Figure 3 shows a view of the guide base on a slightly sedimented slope, with the two strings of casing.

After a pipe trip to install a RCB bit, coring started on 19 December 1992. Core 147-894G-4R to -13R (3068.4–3136.5 mbsl; 45.0–113.1 mbsf) penetrated 68.1 m and recovered 31.8 m of gabbronorite, olivine gabbronorite, and gabbro. Because hole conditions were deteriorating, it was necessary to wipe out, ream, and clean the hole after each core to reach the bottom again. Conditions became worse after Core 147-894G-13R, so the bit was changed.

The hole was reentered with a new RCB bit on 21 December 1992; however, bad hole conditions made continued coring impossible. Core 147-894G-14R (3136.5–3142.3 mbsl; 113.1–118.8 mbsf) penetrated only 5.7 m and recovered gravel interpreted as cuttings that had fallen into the hole and 0.52 m of gabbronorite. Again we decided to change the bit.

On 22 December 1992, while the pipe was being tripped, the three beacons released simultaneously for no apparent reason. They were recovered; the ship returned to the GPS position for Hole 894G, and a new beacon was dropped. The hole was reentered with a new RCB bit, and the hole was reamed and cleaned again. Core 147-894G-15R (3142.2–3146.2 mbsl; 118.8–122.8 mbsf) penetrated 4 m and recovered 0.83 m, possibly partly rubble. Subsequently, despite wiping, reaming, and attempts to clean the hole, it was impossible to reach bottom. Core 147-894G-16W recovered 0.40 m of cuttings while unsuccessfully trying to reach bottom. The pipe was tripped out. The wear pads on the bit were worn off, and the body was worn down during hole cleaning.

To wipe out the ledges and clean the hole, a 9-3/4-in. tricone drill bit was run. After the hole was cleaned, the bit penetrated 3 m below the bottom (3149.2 mbsl).

Coring started again on 25 December 1992 with a new RCB bit. Cores 147-894G-17R to -19R (3149.2–3169.0 mbsl; 125.8–145.6 mbsf) penetrated 19.8 m and recovered 5.69 m of gabbronorite crosscut by a porphyritic dike in the lower part. The hole could not be reamed back to bottom. The bit showed vertical abrasion caused by bad hole conditions.

The hole was reentered on 26 December 1992 with a new RCB bit equipped with stabilizer blades to clean out the hole to the bottom and core ahead. The hole had to be reamed and cleaned before coring started. Core 147-894G-20R (3169.0–3177.9 mbsl; 145.6–154.5 mbsf) penetrated 8.9 m and recovered a total of 2.40 m in four successive trips of the core barrel. The core barrel, equipped with a center bit, was then dropped to drill the rubble before reaching bottom. During the reaming and cleaning of the hole, the drill pipe got stuck for a half hour, so the pipe was tripped and the drill bit was inspected. The top stabilizer appeared severely damaged. We decided to run a RCB bit without stabilizers and core ahead; however, bad hole conditions prevented reaching bottom. The drill pipe got stuck for 2.50 hr on 28 December 1992 before it was finally set free. After these repeated attempts to clean the hole and reach bottom, it became obvious that hole conditions were too bad. Therefore, the hole was abandoned after a reduced suite of logging, and we moved to Site 895.

At Hole 894G we penetrated a total of 154.4 mbsf, cored 127.5 m, and recovered 45.15 m (35.4% average recovery) (Table 2). Regular steel barrels and chromium barrels were used alternatively without a plastic liner. The very bad hole conditions that caused us to abandon the hole are thought to result from a combination of factors: a large cavity at the top, which may have caused problems in the evacuation of the cuttings; high fracture density in the gabbros, which may have caused hole deviation and produced ledges; and stress release within the formation at the bottom of the hole.

Logging: First Phase

The logging program was cut back significantly, and radioactive sources were not used because of hole conditions. Two preliminary runs were designed to check hole conditions prior to running the tools used to obtain structural data (BHTV or FMS).

Run 1

The first tool string was made of HLDT, LSS-SDT, NGTC, and TLT (see "Downhole Measurements" section, "Explanatory Notes"

Table 2. Coring summary for Hole 894G.

Core	Date (1992)	Time (UTC)	Depth (mbsf)	Length cored (m)	Length recovered (m)	Recovery (%)
147-894G-						
			0.0–18.6	18.6		(drilled)
1R	13 Dec.	0810	18.6–28.6	10.0	0.15	1.5
2R	13 Dec.	1410	28.6–38.2	9.6	3.59	37.4
3R	13 Dec.	2045	38.2–39.6	1.4	0.11	7.9
			39.6–45.0	5.4		(drilled/reamed)
4R	19 Dec.	2300	45.0–50.0	5.0	2.48	49.6
5R	20 Dec.	0045	50.0–54.8	4.8	0.27	5.6
6R	20 Dec.	0610	54.8–64.8	10.0	2.92	29.2
7R	20 Dec.	1215	64.8–68.5	3.7	1.86	50.3
8R	20 Dec.	1600	68.5–74.4	5.9	2.13	36.0
9R	20 Dec.	2300	74.4–79.1	4.7	5.46	116.0
10R	21 Dec.	0100	79.1–84.1	5.0	1.59	31.8
11R	21 Dec.	0610	84.1–93.8	9.7	3.38	34.8
12R	21 Dec.	1100	93.8–103.40	9.6	7.85	81.8
13R	21 Dec.	1530	103.4–113.1	9.7	3.86	39.8
14R	22 Dec.	0430	113.1–118.8	5.7	0.52	9.1
15R	23 Dec.	0910	118.8–122.8	4.0	0.83	20.7
16W	24 Dec.	0030	122.8–122.8	0.0	0.40	(wash core)
			122.8–125.8	3.0		(drilled)
17R	25 Dec.	1200	125.8–130.9	5.1	2.36	46.3
18R	25 Dec.	1715	130.9–140.5	9.6	2.24	23.3
19R	26 Dec.	0430	140.5–145.6	5.1	1.15	22.5
20R	26 Dec.	2330	145.6–154.5	8.9	2.40	26.9
21W	28 Dec.	1900	154.5–154.5	0.0	0.23	(wash core)
			Coring totals	127.5	45.15	35.4
			Washing totals	0.0	0.63	
			Drilled	27.0		
			Combined totals	154.5	45.78	

Note: Cores 2R, 4R, 5R, 6R, 7R, 9R, 11R, 12R, 13R, 14R, 15R, 17R, and 18R cored with chrome core barrel.

chapter, this volume). The HLDT was run without a source to obtain caliper data. Driller data located the mud line at 3023.4 mbsl, the bottom of casing at 3056.4 mbsl, and the bottom of the drill pipe at 3057.4 mbsl (i.e., 1 m below casing). The tool string was rigged up on 29 December 1992 at 0330 hr. Before the tool string was sent down the pipe, the NGT was changed. The mud line was reached at 0525 hr, and open hole at 0535 hr. Ledges stopped the descent at 3083.8, 3094, 3105, and 3107 mbsl (these and all subsequent depths are now logging cable depths unless otherwise specified). Despite 20 min of trial, the last ledge could not be passed; therefore, the hole was logged up from 3107 mbsl to 3023 mbsl (i.e., expected mud line). The string was then lowered again in a second attempt to reach bottom but would not pass on a ledge at 3080 mbsl. A repeat section was then logged from 3080 mbsl to 3052 mbsl, and the tool string pulled out of the hole. The tool string reached the rig floor at 0755 hr on 29 December 1992. Caliper readings showed that the hole diameter varied widely and was larger than 15 in. for most of the logged interval; therefore, Formation MicroScanner (FMS) logging was ruled out. Sonic data located the bottom of the pipe at 3051 mbsl.

Run 2

This run aimed at reaching a deeper part of the hole. The pipe was lowered to 3092 mbsl (driller depth), and the tool string was shortened both to make it easier to pass ledges and because the sonic data of Run 1 were of poor quality because of the large hole diameter. The second tool string was thus made of HLDT, NGTC, and a second TLT. The string was rigged up on 29 December 1992 at 1030 hr. Mud line was reached at 1200 hr and open hole at 1210 hr. The string could not pass a ledge at 3094 mbsl even after the drill pipe had been raised to 3086 mbsl. Run 2 was then aborted at 1255 hr, and the tool string was pulled out of the hole. Water leaked into the TLT and its data were lost.

Drift survey

To constrain the hole deviation, a drift survey was conducted inside the pipe using a Kuster multishot tool from 74.0 mbsf to the mud line. The results show a systematic increase from 0°–5° over this depth interval (Table 3). Given these data, it can be assumed that the deviation was probably significantly greater at the bottom of the hole.

Run 3

The string used on this run was the LDEO digital borehole televiewer (BHTV). The tool string was sent downhole on 29 December 1992 at 1700 hr. During the down-going log, communication was lost with the string in pipe around 1600 mbsl at 1810 hr. After unsuccessful attempts to resume communications, the tool string was pulled out of the hole and reached rig floor at 2230 hr. Suspected causes of the failure were overheating of a surface unit during logging and a slight leak (20 MΩ) that was detected in the pigtail (i.e., the Schlumberger wireline to GO head adaptor) after the tool reached the rig floor. The pigtail was then changed, and even though communications problems persisted for a while, they were finally overcome, and the tool was sent downhole again at 0030 hr, 30 December 1992. Transmission showed some error, was interrupted at 729 mbsl but resumed, and logging downward was possible to 1497 mbsl, where communication was lost again and never recovered. Run 3 then was aborted, and the tool was pulled out of the hole at 0353 hr and rigged down at 0530 hr. The logging program was terminated. Later checking of the pigtail showed all wires to be shorted to shield.

Table 3. Hole deviation measurements.

Depth (mbsf)	Hole deviation
0.0	0°
54.0	3°
64.0	4°
74.0	5°

Logging: Second Phase

After Hole 895F was abandoned on 14 January 1993, the ship was moved back to Hole 894G for a second phase of logging. The second logging program was designed to gather orientation and magnetic data. Only one run was conducted, using a FMS tool string (NGT-GPIT-MESTB) to which the LDEO TLT was attached. The pipe was lowered 5 m below mud line, and the tool string was sent downhole on 14 January 1993 at 1055 hr. The string reached mud line at 1205 hr and stopped at 3106.7 mbrf (logging depth) at 1215 hr. The string could not pass that depth, which corresponds to the same ledge as during the first phase of logging. The hole was logged five times from that depth up to 3070 mbrf. During the fifth pass, the tool string was blocked by a ledge at 3076 mbrf, which was passed only after a 7000-lb pull. The caliper pads then refused to close against the FMS body while reaching the bottom of the pipe. The tool string was pulled into casing and then into pipe by a 9000-lb pull. Because the tool string would not go any further, the wireline was crimped and cut, and the tool was brought back with the pipe after the casing string was latched.

Retrieval of the HRB at Hole 894G

After the logging program ended with the FMS stuck in the drill pipe, the 10-3/4-in. casing string was successfully latched and pulled out of the hole. The pipe was tripped and the casing, bit, and tool string reached the rig floor on 15 January 1993 at 0100 hr. The FMS was recovered with one of the caliper arms bent upward and wedged against the bit. The hole was reentered with the Dril-Quip running tool, and the HRB was latched successfully and brought back to the ship at 1330 hr, 15 January 1993. The HRB was disassembled, and at 0300 hr on 16 January 1993, the ship departed for a five-day transit to Panama.

SEDIMENTS

Introduction

Sediments were recovered in short cores from Holes 894A, 894D, and 894E. The holes were drilled as part of a general survey of the seafloor that utilized video imaging and exploratory drilling to locate stable bedrock with a minimum of surficial sediment on which to place a hard-rock guide base. The taped video images reveal a thin but widespread blanket of light-colored (reflective) sediment on the summit of the intrarift ridge and outcrops to the south and southwest. During the course of the survey, the drill string was lowered numerous times to probe the sediment thickness. The accuracy of these measurements, however, is questionable. In an area across the summit and slightly down the north slope, the drill pipe penetrated at least 2 m of soft material, ooze, or mud, and averages 3.4 ± 0.9 m in thickness for 19 measurements. Hole 894D is in this area, and Hole 894A is on its edge. Sediment cover to the south and southwest is quite uneven. Outcrops are more frequent, although measurements of 6–10 m were recorded, but these may include stabs where the drill string actually "walked" down steep rock surfaces. This is where Holes 894B, 894C, 894F, and 894G were emplaced.

Information about sediment in Hess Deep is scant. Francheteau et al. (1990) mention that the floor of the Deep at 5454 m is "ubiquitously covered by brown-colored, turbidite-like sediment on which large boulders of gabbroic and doleritic rocks shed from the north flank of Hess Deep are found" (p. 285–286). Blum (1991) describes 3.5 kHz records showing a maximum of 20 m of sediment at the bottom of the Deep. Hydrothermal material (pyrrhotite, pyrite, silica) was found in igneous and sedimentary materials recovered from the floor of the Deep (Rudnik, 1976; Murdmaa and Rozanova, 1976). Hydrothermal serpentine was recovered in two sediment cores (Schmitz et al., 1982; Blum, 1991; Eckhardt, 1992). None of these deposits are described as laterally extensive. Indeed, basaltic and plutonic rock crop out at numerous localities on the south flank of the intrarift ridge (Francheteau et al., 1990), and no accumulations of sediment are detected by 3.5 kHz sounding on the ridge.

Other information pertinent to sedimentation in Hess Deep is as follows. Site 894, located at 2°18′N, is within the belt of equatorial high productivity that results from welling up and westward equatorial flow of the nutrient-rich, cold-water Peru current (Moore et al., 1973). Heightened productivity of both siliceous and calcareous micro-organisms and flora results in rapid accumulation of sediment in the equatorial region. A thick belt of biogenic sediment lies west of the East Pacific Rise (the "equatorial sediment bulge"), and the high surface productivity has created great thicknesses of biogenic sediment on the shallow ridges bounding the Panama Basin east of the East Pacific Rise (e.g., van Andel, Heath, et al., 1973). The calcium carbonate compensation depth (CCD) near Site 894 is about 4.5 km (Berger and Winterer, 1974). Mean sediment accumulations for the past 5 Ma near Site 894 are 29 m/Ma at Site 503 (4°03′N, 95°38′W; Prell, Gardner, et al., 1982) and 50 m/Ma at Site 504 at 1°14′N, 83°44′W, on the Costa Rica Rift, eastern Panama Basin (Beiersdorf and Natland, 1983). The two sites are in almost identical water depths (3672 m at Site 503; 3640 m at Site 504). The summit of the intrarift ridge at Hess Deep is less than 3020 m, well above the CCD, whereas the bottom of the Deep, at 5450 m, is well below it. At Site 894, present-day biogenic/pelagic accumulation rates should be in excess of 30 m/Ma.

Hole 894A

In Hole 894A, more than 6 m of sediment was recovered. The upper 1 m is composed of highly disturbed foraminiferal sand with a significant fraction (>40%) of sand-sized grains derived from igneous sources. Some small lumps of pale brown ooze also are dispersed in the sand. Below this for the remainder of the core is a coarse igneous lithic breccia containing angular fragments of basalt up to 5 cm in diameter. Most of the material is in the size range of coarse sand to pebbles. Thin sections of two larger clasts and epoxy-mounted sand reveal the breccia to be virtually monomict. Almost all the sand grains in the sections are simply smaller fragments of the larger pebbles, having similar grain size, primary mineralogy (plagioclase, relict pyroxene, and oxide minerals), and metamorphic characteristics (presence of chlorite, green amphibole after pyroxenes, and titanite after ilmenite exsolved from titanomagnetite). Rare sand grains were derived from fine-grained metamorphosed basalt. These are also chloritic, and have similar, but smaller, titanite-magnetite intergrowths. Fine fractions are composed of plagioclase, pyroxene, amphibole, chlorite, and clays.

The lithological character of the lithic breccia on the seafloor is difficult to determine because of drilling disturbance. Several fining-upward graded sequences were noticed, but these probably resulted from hydraulic separation of coarse and fine particles as seawater was pumped into an unstable hole during coring. Without question, however, the fragmental aspect of the breccia existed before coring.

The lithological consistency of sand-sized grains in the breccia may be contrasted with the lithic fraction of the foraminiferal sand at the top of the hole. The latter contains not only grains similar to those in the breccia, but also fresh and even partly glassy aphyric basalt. Because drilling disturbance reduced this sediment to the consistency of soup, those sand grains similar to the lithic breccia probably were mixed in during drilling. The foraminiferal sand thus carries a distinctive lithic fraction of fresh, aphanitic basalt, and was deposited on top of the coarse lithic breccia. The breccia itself was derived from quite different greenschist-facies metamorphosed basalt. The lithological consistency of the coarse, poorly sorted breccia, and its absence in other holes 75–170 m away, suggests derivation from sources in the immediate vicinity of the hole.

Hole 894D

In 10 m penetrated, only 1.3 m of mixed calcareous sediment was recovered in Core 147-894D-1R of Hole 894D. The recovered sediment is highly disturbed, but not so much that distinctive sedimentary facies are totally obscured. There are two medium-fine foraminiferal sand layers, both of which grade to finer material upward, with now-disturbed basaltic sand at their bases. Most of the rest of the core is vari-colored brown to pinkish gray foraminifer-nannofossil ooze. The darkest brown ooze was measured to have 68.5% $CaCO_3$. An angular basalt clast is found at 105–110 cm in the core. Igneous pebbles in the core catcher are diverse and include a quite fresh, densely olivine phyritic basalt with limpid green olivines speckled with Cr-spinel. Cobble- and pebble-sized rock fragments in Core 147-894D-2R include one uniformly fine-grained aphyric basalt, and a spherulitic fragment from a pillow rind. Thus they constitute a coarse polymict basaltic conglomerate beneath calcareous sediments at this location.

The significance of the foraminiferal sand in Hole 894A became evident with recovery of these cores. The fining-upward foraminiferal sands are the deposits of turbidity currents that entrained both basaltic and carbonate material. The beds reflect both size concentration of medium-fine foraminifers and basaltic sand, and density separation of basaltic from foraminiferal sand particles. The basal conglomerate comprises size- and density-sorted igneous cobbles in the same bedding sequence.

Between the sandy layers, calcareous ooze was deposited in a quieter depositional regime, both as the distal, finer-grained, nannofossil-rich portions of turbidites (lighter-colored ooze), and as simple pelagic accumulations. Darker clay-bearing nannofossil oozes suggest deposition below the foraminiferal lysocline, and perhaps near the CCD.

Hole 894E

At Hole 894E, 2.4 m of varied calcareous and lithic igneous lithologies overlies igneous lithologies that include coarse-grained gabbronorite and brecciated, cataclastic gabbro metamorphosed to greenschist facies assemblages.

The upper 1.2 m of sediment was recovered as very soupy foraminiferal sand with no intact bedding features, but containing a small percentage of basaltic sand grains. Sediments below this, though highly disturbed, retain several obvious contacts, some of them highly disturbed by a combination of protrusion of soft sediment into the liner, and twisting of beds by frictional adherence to the liner as it rotated. The contacts are between beds having different proportions of foraminiferal sand, or juxtaposing varieties of calcareous ooze against basaltic sand that grades upward in disturbed fashion to foraminiferal sand. Below 1.5 m, the core contains two horizontal beds of igneous lithic breccia having fragments of fresh aphyric basalt up to 1.0 cm. The core bottoms in coarse basaltic lithic breccia with a cobble of fresh, aphyric, fine-grained basalt in the core catcher.

Discussion

Recovered at these three holes were two principal sedimentary facies: (1) an association of basalt cobbles, basaltic lithic breccias, basaltic sand, and foraminiferal sand in grading-upward sequences, found in all three holes; and (2) poorly sorted nearly monomict igneous breccia consisting of greenschist-facies basalt with intergranular textures and rare fine-grained metamorphosed basalt with variolitic to microlitic textures. The latter appears to be locally derived, whereas the turbidites were transported for some distance. Because all plutonic igneous basement cored at Site 894 has a sub-

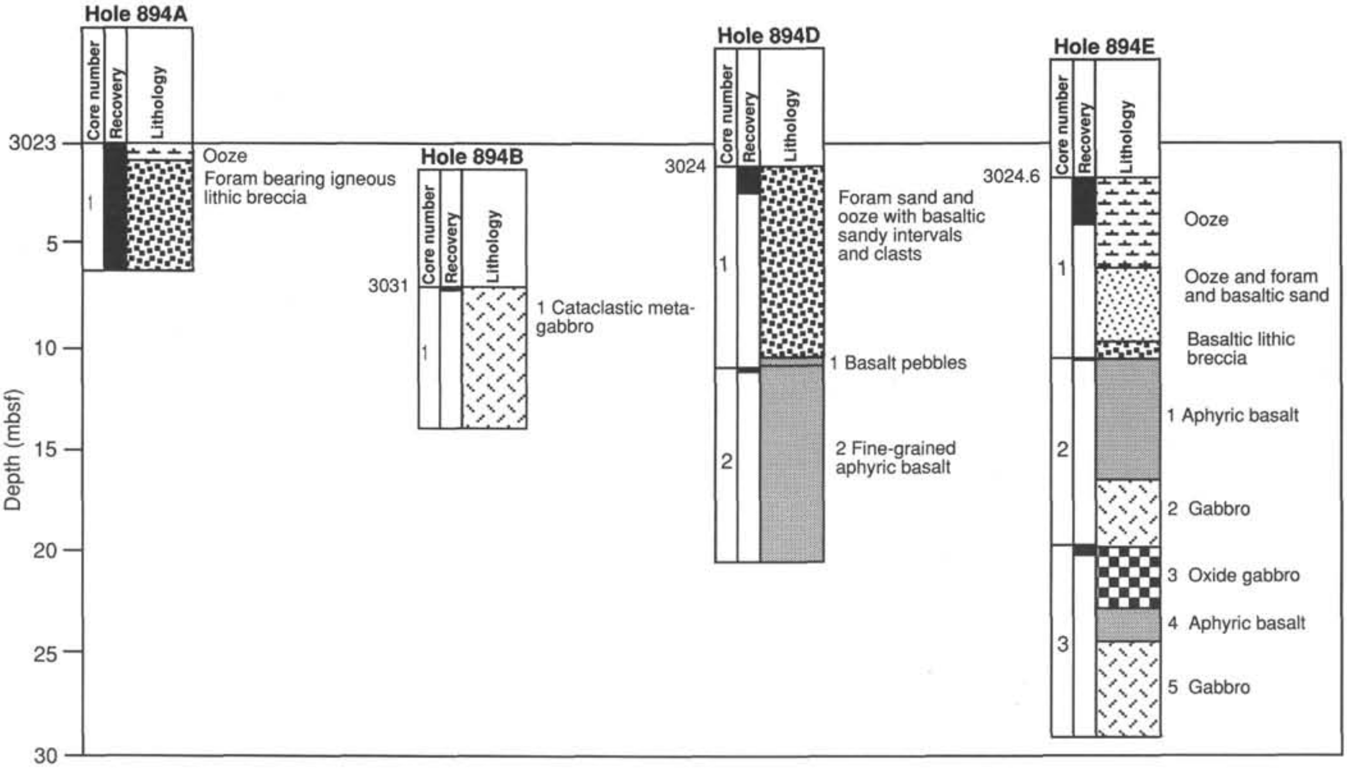

Figure 4. Igneous lithostratigraphy of Holes 894A, -B, -D, and -E. Note that the depth of each hole (mbsl) is shown at the top of each lithologic column.

stantial greenschist-facies overprint, a local source for the breccia in Hole 894A is suggested. If the diabase is of local origin, however, then this small area consists of both gabbro and diabase, suggesting a high structural level—toward the gabbro-dike transition—in this block of ocean crust. The mechanism of disaggregation of the breccia is uncertain, but it could represent a regolith produced by crushing along a faulted interface, which both slopes of the intrarift ridge must represent in some fundamental way. Therefore, the extensive cataclasis and brecciation in metamorphosed gabbros in Holes 894F and 894G may simply reflect less disruption of the fault surface, or more complete cementation by hydrothermal veins.

The occurrence of coarse basaltic-foraminiferal turbidites at the summit of the intrarift ridge is important because such material, presumably entrained from debris flows that cascaded from the high rifted cliffs of basalt and sediment to the north and south, cannot climb this ridge now. More likely, the coarse materials were deposited when the ridge summit actually was still in a basin in which the turbidites could pond. By this interpretation, they are relict deposits, and cessation of their deposition records the relative or actual uplift of the intrarift ridge.

Similarly, the oldest such deposits record the earliest exposure of this feature by rifting. Lonsdale (1988) dates the crust here at 1 Ma, and Francheteau et al. (1990) consider that rifting was initiated about 0.5 Ma. Exposures of this age at 3000 m should be covered with approximately 15 m of calcareous ooze, based on regional sediment accumulation rates summarized earlier. At the comparatively flat summit of the intrarift ridge, they are only 2–4 m thick, and mainly consist of transported turbidites. Alternatively, sediments might have been redeposited from ridges by currents into thicker accumulations in deep ponds. However, the maximum accumulation in Hess Deep proper is only 20 m (Blum, 1991), with nearly bare surrounding ridges. All this suggests that the intrarift ridge in Hess Deep was exposed by tectonic processes in the very recent past, perhaps as recently as 50,000–100,000 years ago. Dating of the calcareous sediments of Site 894 is obviously important to pursue with shore-based studies.

PETROGRAPHY OF HOLES 894A–894E

Hole 894A

Hole 894A recovered a single core of foraminifer ooze and igneous lithic breccia. Within the breccia are matrix-supported angular clasts (up to 5 cm in size) of massive, fine-grained to microcrystalline aphyric basalt, as well as abundant smaller fragments of fine-grained and glassy basalt (Fig. 4). Examination in thin section of both larger clasts and smaller, subcentimeter fragments shows that they exhibit variolitic, microlitic, and intergranular textures, with the coarser samples containing up to 12% magnetite and ilmenite. Tabular to lath-like plagioclase and subhedral, anhedral, and plumose clinopyroxene are the sole primary silicate phases; occasional, subhedral to euhedral plagioclase and clinopyroxene phenocrysts up to 1 mm in size are found within some samples. Anhedral pyrite and chalcopyrite are found together as trace accessories, occurring up to 0.2 mm in size. The abundance of oxides in all of the samples (5%–12% by mode) suggests that these fragments and clasts represent ferrobasalts.

Metamorphic alteration of these fragments is moderate. Clays (both chloritic and mixed-layer smectite/chlorite?) replace mesostasis, clinopyroxene, and plagioclase, and thin sections of grain mounts show that secondary amphibole replaces clinopyroxene in many of the smaller fragments. Secondary pyrite occurs in trace quantities.

Hole 894B

Hole 894B recovered three fragments of medium-grained, cataclastic gabbro in a single core (Fig. 4). Where relatively undeformed, the rock contains nearly equal amounts of subhedral tabular to anhedral zoned plagioclase and anhedral clinopyroxene in a hypidiomorphic granular texture. Minor amounts (to 5%) of anhedral orthopyroxene are inferred to have been in the mode, although no fresh orthopyroxene is visible. Minor amounts (about 1% or less) of interstitial magmatic oxides (to 1.3 mm; originally ilmenite and magnetite in a 4:1 ratio) and trace sulfides (to 0.01 mm) also occur, with the oxides exhibiting lattice exsolution.

Metamorphic alteration in these rocks is high to pervasive. Cataclastic shearing has resulted in intense grain size reduction of all phases, accompanied by pervasive alteration. Some areas of the rock consist of a matrix-supported cataclasite, whereas others contain thin, irregular shear zones with development of a proto-cataclasite texture, with plagioclase and clinopyroxene exhibiting extinction. Plagioclase is altered extensively to secondary plagioclase, clays, and green amphibole, with amphibole often occurring in crosscutting veins. Clinopyroxene is pervasively altered to intergrown fibrous mats of pale green amphibole, oxides, and clay, with minor amounts of secondary clinopyroxene. Orthopyroxene is completely altered to chlorite, clay, and trace amounts of cummingtonite. Trace amounts of epidote occur, as do anastomosing veins of actinolite and prehnite.

Hole 894C

Two fragments of aphyric basalt and sheared, pervasively metamorphosed gabbro constitute the recovery from Hole 894C. Both samples were caught in the drill string after loss of the bottom-hole assembly and represent miscellaneous (noncored) samples. The basalt (Piece 1) is brecciated, cut by chloritic veins, and holocrystalline, with its intergrown plagioclase and clinopyroxene highly altered to amphibole, clays, and secondary plagioclase. The sheared gabbro is nearly completely altered to amphibole, secondary plagioclase, and chlorite, with both intense shearing and veining by clay/chlorite assemblages.

Hole 894D

Two cores were recovered during the coring of Hole 894D (Fig. 4). Nannofossil foraminifer sand and ooze compose the upper part of the section, containing an angular, 4-cm fragment of aphyric basalt. Beneath the sediments, two types of basalt occur. In the core catcher of Section 147-894D-1R-1, two 1- to 4-cm fragments of fresh, fine-grained, highly olivine-phyric basalt were recovered. These fragments contain abundant (15%–20%), large (to 5 mm) euhedral crystals of olivine peppered with Cr-spinel inclusions (to 0.25 mm). The abundance of large olivine phenocrysts indicates that they are picritic.

Massive, sparsely plagioclase-phyric to aphyric basalt also occurs as two centimeter-sized fragments in the core catcher of Section 147-894D-1R-1, and composes the two large pieces of Section 147-894D-2R-1. The plagioclase phenocrysts are euhedral to subhedral and up to 2 mm in size, and occur in a fresh to slightly altered, glassy to fine-grained and holocrystalline matrix. Glassy selvages on individual pieces indicate that they could represent fragments from a pillowed flow.

Hole 894E

Aphyric, massive, slightly altered fine-grained basalt constitutes Piece 1 of Section 147-894E-2R-1 (Unit 1 in core), and similar basaltic clasts and fragments compose a breccia recovered at the base of Core 147-894E-1R. Basaltic sand also was recovered in Core 147-894E-1R (see "Sediments" section, this chapter; Fig. 4).

Unit 2, comprising fine-grained, intergranular gabbro, is defined solely by several small fragments of Section 147-894E-2R-1 (Piece 2). These fragments are oxide-rich, containing up to 5% Fe-Ti oxides. They also are highly metamorphosed, with secondary plagioclase, secondary clinopyroxene, actinolite, and chlorite replacing nearly half of the plagioclase and most of the clinopyroxene.

Varitextured, medium-grained oxide gabbro constitutes Unit 3, defined in core by Section 147-894E-3R-1 (Pieces 1 through 4). Subhedral to anhedral plagioclase and anhedral clinopyroxene (some grains as oikocrysts) make up the bulk of the rock and occur in approximately equal proportion, with plagioclase exhibiting a crude magmatic flow alignment. Plagioclase shows minor fracturing and undulatory extinction, and contains rounded inclusions of clinopyroxene. Magnetite and ilmenite occur together as anhedral, interstitial grains (to 5 mm), and have a modal abundance of up to 8%. Pyrite with associated trace chalcopyrite is a minor component (to 0.6 mm), and euhedra of apatite (to 0.05 mm) occur in trace amounts. Overall, Unit 3 is highly metamorphosed, with clinopyroxene pervasively metamorphosed to amphibole, secondary clinopyroxene, oxides, and clay. Plagioclase is moderately metamorphosed to secondary plagioclase, amphibole, and clays, and is cut by fine veinlets filled with possible chlorite.

Massive, holocrystalline and microcrystalline aphyric basalt makes up Unit 4, defined by Pieces 5 and 6 of Section 147-894E-3R-1. It contains sparse phenocrysts of euhedral plagioclase (to 2 mm) and subhedral clinopyroxene (to 1 mm) in a highly altered groundmass, and could represent a dike.

Unit 5 is a medium-grained, variably textured gabbro, defined by Pieces 7 through 11 of Section 147-894E-3R-1. Subhedral-tabular to anhedral plagioclase grains commonly enclose inclusions of clinopyroxene and constitute 50%–55% of the rock. Clinopyroxene composes only a slightly smaller portion of the unit, forming oikocrysts enclosing both plagioclase and smaller grains of clinopyroxene as well as more granular grains. Magnetite and ilmenite form irregular, anhedral interstitial grains to 2 mm in size, and small (<0.5 mm), irregular grains of pyrite and chalcopyrite are trace and rare accessories, respectively.

Unit 5 is moderately brecciated and veined with prehnite, chlorite, calcite, and amphibole. It is highly metamorphosed, with plagioclase moderately to highly metamorphosed to secondary plagioclase, clay, amphibole, and chlorite; clinopyroxene is pervasively metamorphosed to amphibole, oxides, secondary green and brown clinopyroxene, and clays.

IGNEOUS PETROGRAPHY OF HOLES 894F AND 894G

Introduction

Holes 894F and 894G provided the most significant recovery of igneous rocks from Site 894. Hole 894F represents a section of rock types equivalent to that which was drilled but not cored in Hole 894G between the seafloor and 18.60 mbsf (Fig. 5). Thus we describe the lithologies of these two holes as part of one continuous section. The rocks in Hole 894F and in the upper part of Hole 894G are strongly deformed and have been transformed locally to cataclasites. Parts of the core consequently were difficult to classify, and it also was difficult to determine the igneous protolith with certainty.

The igneous lithologies recovered in Hole 894F are gabbro, olivine gabbro, and basalt. Hole 894G also yielded gabbroic rocks and two basaltic dikes that have chilled contacts against the gabbroic host. Above 45 mbsf, the upper part of Hole 894G is dominated by gabbros and olivine gabbros that are similar to lithologies recovered from Hole 894F. Further downhole, gabbronorites and olivine gabbronorites are the principal igneous lithologies, although intervals of gabbro reappear locally below about 80 mbsf. A summary of igneous lithostratigraphic units for Holes 894F and 894G is given in Tables 4 and 5 respectively, and shown diagramatically in Figures 5 and 6. Percentages of each major lithology calculated for the core from Hole 894G are tabulated in Table 6. The rocks recovered from the two holes do not show modal layering, although concentrations of both olivine and oxides can be seen in a few thin sections and also locally in the core. The lithologic types exhibit a significant range in textural characteristics and grain size. A description of the principal lithologies (in order of their abundance in the core), the primary silicates, oxide minerals, sulfide minerals, and accessory minerals of the rocks, and the observed relationships among different lithologies are provided below.

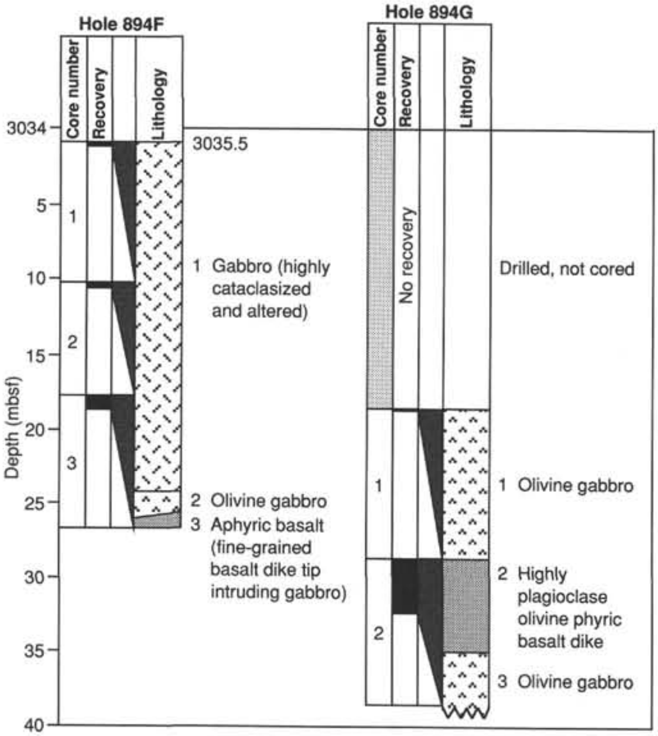

Figure 5. Igneous lithostratigraphy of Hole 894F and the uppermost units of Hole 894G. Note that the depth of each hole (mbsl) is shown at the top of each lithologic column. The complete lithostratigraphy of Hole 894G is shown in Figure 6.

Petrography of the Main Plutonic Lithologies

Primary modes for each piece of core recovered were estimated by visual inspection and averaged for each section of core. These results are recorded in the HARVI database and, where significant, variations in these abundances have been noted in the comments section of those reports. Table 7 presents primary modal mineralogies either point counted with a minimum of 1500 points and a counting interval of 0.5 mm or visually estimated from thin sections of each of the lithologic types.

Gabbronorites

Gabbronorites represent the most voluminous of the lithologies recovered at Site 894. With the exception of four samples that appear to have anomalously high proportions of plagioclase (possibly due to accumulation), modal contents of clinopyroxene in the gabbronorites exhibit a consistent average of 31% with a standard deviation (s.d.) of 3.5%. Likewise, plagioclase modal contents are consistently 53% (s.d. = 4.4%). Orthopyroxene abundance is more variable with an average of 14% (s.d. = 4.4%).

One of the most outstanding features of the gabbronorites is the diversity in grain size present at the core, section, piece, and thin-section scale, despite the relative consistencies in modal abundances. Many of the gabbronorites sampled exhibit poikilitic textures characterized by anhedral clinopyroxene and orthopyroxene, all ranging in grain size from 2 to 10 mm and enclosing anhedral to subhedral crystals of olivine and plagioclase (Fig. 7A, -B). In places, euhedral to subhedral plagioclase crystals are separated by finer-grained anhedral clinopyroxene crystals, forming an intergranular texture. In many samples, plagioclase and clinopyroxene crystals approach similar average grain sizes, approximately 2 to 3 mm. Plagioclase is euhedral to subhedral, and clinopyroxene is anhedral. This association of

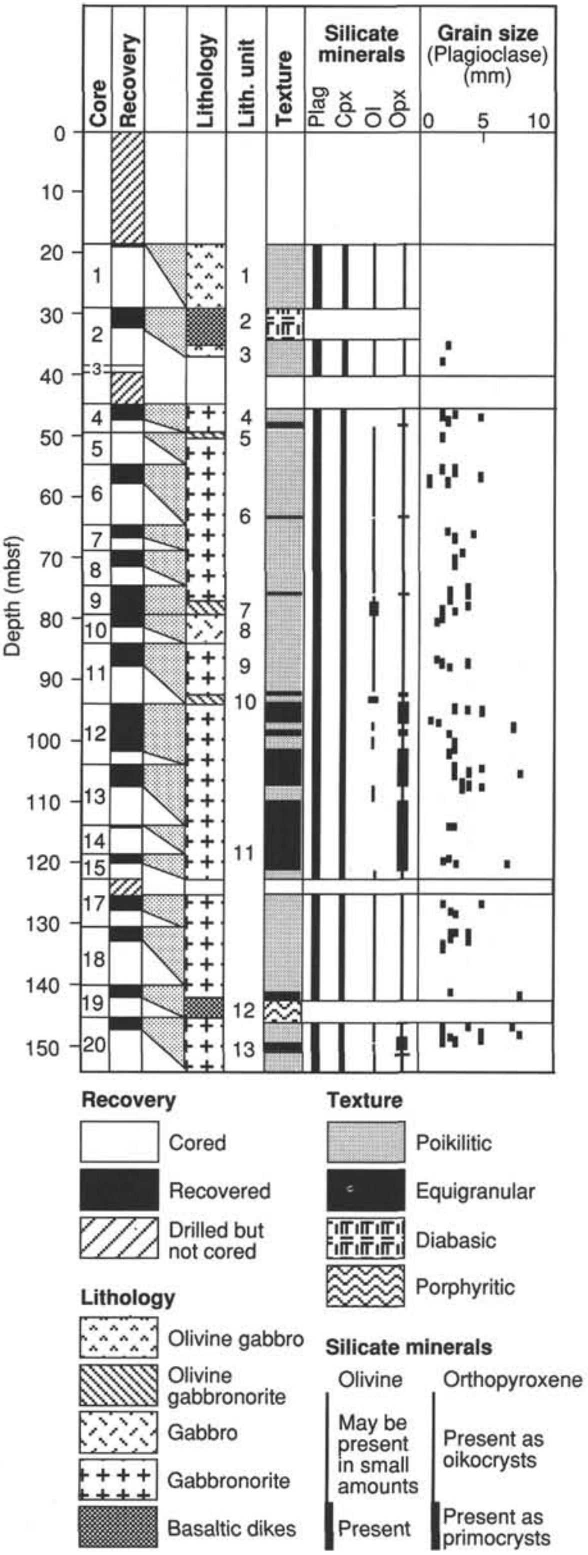

Figure 6. Summary of the igneous lithostratigraphy of Hole 894G. Plag = plagioclase, Cpx = clinopyroxene, Ol = olivine, Opx = orthopyroxene; grain size represents average plagioclase grain size.

Table 4. Summary of igneous lithostratigraphic units for Hole 894F.

		Top of unit			Bottom of unit					Contact description[a]					
Unit no.	Lithology	Core, section, piece	cm[b]	Depth (mbsf)[c]	Core, section, piece	cm[b]	Depth (mbsf)[c]	Expanded depth (mbsf)[d]	Curated thickness	Type	Nature	Morphology	Texture[e]	Grain size[f]	Notes
1	Gabbro	1R-1, 1	0	0	3R-1, 16	96	17.76	23.48	1.93	M			V	M	Many pieces are intensely metamorphosed and sheared cataclasites.
2	Olivine gabbro	3R-1, 17	96.0	17.76	3R-1, 19	112	17.92	24.59	0.16	S	I	I	V	M	Contains 5%–10% black olivine pseudomorphs and a trace of fresh olivine.
3	Basalt	3R-1, 19	112	17.92	3R-1, 20	128	18.08	25.70	0.16	S	I	I	M	F	Sharp, intrusive contact in unoriented Piece 19.

[a] Contact description: Type: S = sharp, M = missing. Nature: I = intrusive. Morphology: I = irregular.
[b] cm = depth in core measured from top of section.
c mbsf = curated depth in hole.
[d] See "Igneous Petrography" section, "Explanatory Notes" chapter for definition.
[e] Texture: V = varitextured, M = microcrystalline.
[f] Grain size: M = medium, F = fine.

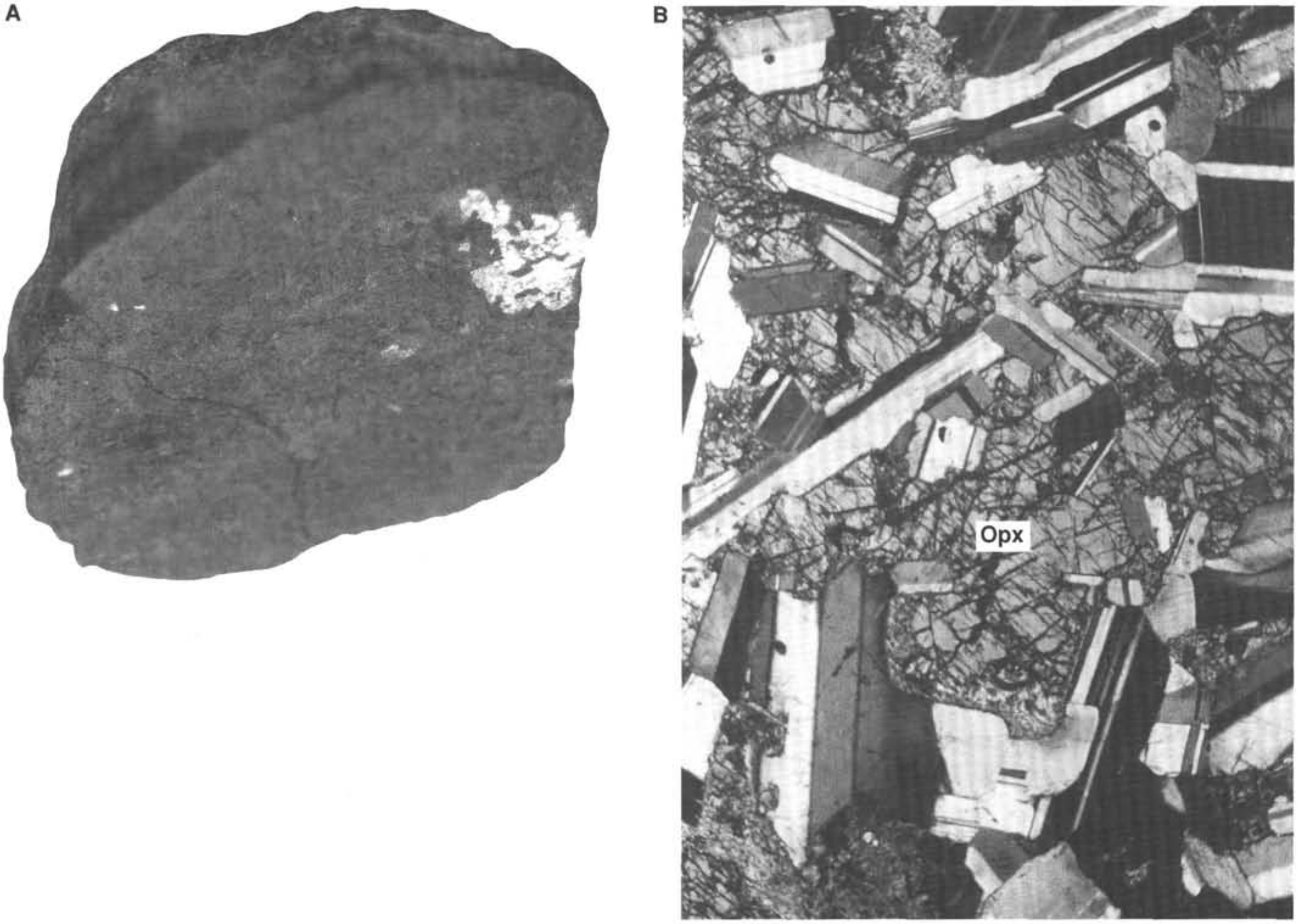

Figure 7. **A.** Photograph of a typical poikilitic gabbronorite. Note reflection of light from an orthopyroxene oikocryst. **B.** Photomicrograph of a typical poikilitic gabbronorite with chadacrysts of plagioclase included in an oikocryst of orthopyroxene (Opx) (from Sample 147-894G-4R-1, Piece 16, 113–120 cm; field of view is 5 mm across).

generally equigranular clinopyroxene and plagioclase is referred to as hypidiomorphic granular texture. Orthopyroxene tends to maintain a poikilitic habit throughout the core and is generally the most coarse-grained primary phase. These textures are end members, and most gabbronorites exhibit gradational textures between them. Many of the gabbronorites contain accessory amounts of olivine.

Some gabbronorites are more plagioclase-rich than others. The plagioclase in these gabbronorites is medium- to coarse-grained and is more euhedral. Clinopyroxene in these rocks is subhedral to intergranular, and orthopyroxene occurs as either subhedral, tabular crystals or as large oikocrysts (Fig. 8A, -B).

Fe-Ti oxide minerals are commonly 1–2 modal percent and vary between a uniform and patchy distribution throughout the gabbronorites. These phases are characterized by interstitial, subrounded magnetite intergrown with laths and discrete blebs of ilmenite in variable proportions, with ilmenite usually predominating. Fe-Ti oxide min-

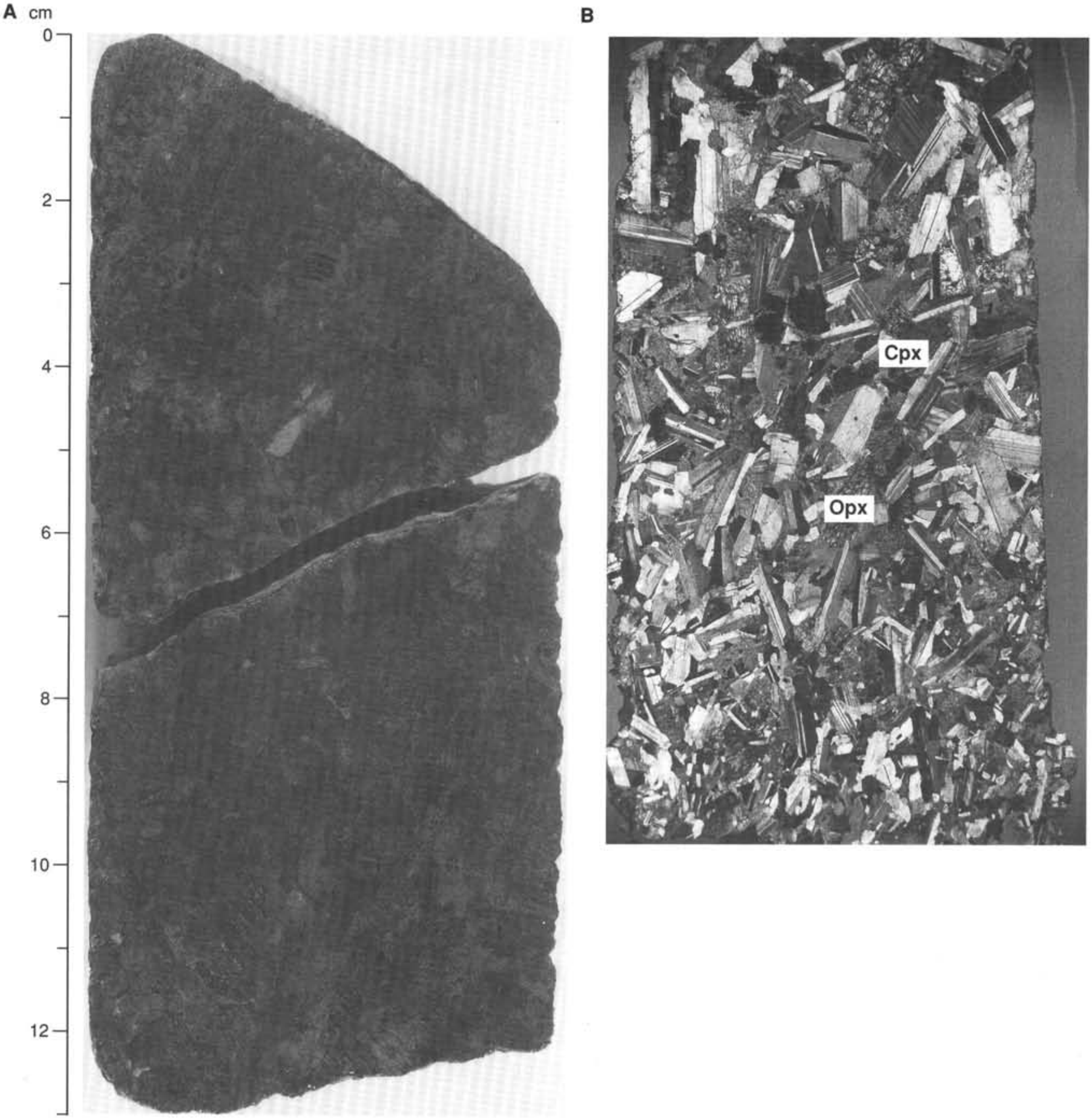

Figure 8. **A.** Photograph of an equigranular gabbronorite with subhedral orthopyroxene and clinopyroxene crystals. **B.** Photomicrograph of an equigranular gabbronorite showing tabular plagioclase and subhedral orthopyroxene (Opx) and clinopyroxene (Cpx) crystals (from Sample 147-894G-11R-3, Piece 6A, 45–49 cm; field of view is 40 mm across).

erals generally range in size up to 1 mm but occasionally reach 3 mm. Trace amounts of secondary pyrite, chalcopyrite, and rare pyrrhotite are recognized as spongy to subangular, very fine-grained crystals particularly common along exsolution lamellae and silicate mineral margins. These sulfide minerals rarely exceed 0.5 mm in size and most commonly are about 0.2 mm in size.

Sporadic enrichment of Fe-Ti oxide minerals occurs in gabbronorites. Patches of oxide gabbronorites (when the modal abundance exceeds 5%) have the same textural variability as gabbronorites. For the most part, they are marked by patchy concentrations of interstitial, subrounded intergrowths of magnetite and ilmenite (Fig. 9). Grain sizes of these oxide minerals are generally greater than the average size of the same minerals in the rest of the core. One interval (147-894G-13R, 130–137 cm; 103.4 mbsf) has a clearly defined layer at least 20 mm thick with 15 modal percent ilmenite at the base of a piece that averages 8 modal percent Fe-Ti oxide minerals. The top of this layer has a dip of 40° relative to a plane perpendicular to the axis of the core.

Olivine Gabbronorites

Olivine gabbronorites have plagioclase and clinopyroxene modal abundances similar to gabbronorite (Table 7), exhibit quite variable orthopyroxene modal abundances, and include between 5 and 10 modal percent olivine (Fig. 10). These rocks are generally poikilitic

Table 5. Summary of Hole 894G igneous lithostratigraphic units.

		Top of unit			Bottom of unit					Contact description[a]		
Unit	Lithology	Core, section, piece	cm[b]	Depth (mbsf)[c]	Core, section, piece	cm[b]	Depth (mbsf)[c]	Expanded depth (mbsf)[d]	Curated thickness	Type	Nature	Morphology
	Drilled, not cored.			0.00			18.60	18.60				
1	Olivine gabbro	1R-1, 1	0	18.60	2R-1, 2	14	28.74	28.91	0.34	M		
2	Plagioclase-olivine-phyric basalt	2R-1, 3	15	28.75	2R-2, 17	127	31.40	34.97	2.62	M		
3	Olivine gabbro	2R-2, 18	128	31.41	2R-3, 14	121	32.81	38.20	1.38	M		
	Rubble	3R-1, 1	0		4R- 1, 5	28	45.28	45.54	0.40			
	Drilled not cored.			39.60			45.0					
4	Gabbronorite	4R-1, 6	28	45.28	4R-2, 14	122	47.56	50.02	2.28	M		
5	Olivine gabbronorite	5R-1, 1	0	50.00	5R-1, 2	15	50.15	52.11	0.15	M		
6	Gabbronorite	5R-1, 3	15	50.15	9R-3, 5f	97	77.95	77.26	11.6	S	SI	I
7	Olivine gabbronorite	9R-3, 5f	97	77.95	9R-5, 3	32	79.14	79.10	2.20	M		
8	Gabbro	10R-1, 1	0	79.10	10R-2, 5	43	79.95	84.13	1.8	M		
9	Gabbronorite	11R-1, 1	0	84.10	11R-3, 3	27	87.29	92.48	3.16	M		
10	Olivine gabbronorite	11R-3, 4	31	87.33	11R-3, 10	76	87.78	93.80	0.45	M		
11	Gabbronorite	12R-1, 1	0	93.80	14R-1, 11	73	113.83	118.80	12.85	M		
	Rubble	15R-1, 1	0	118.80	15R-1, 6	38	119.18	120.28	0.38			
11	Gabbronorite	15R-1, 7	38	119.18	15R-1, 16	103	119.83	122.80	0.65	M		
	Wash	16W-1, 1	0		16W-1, 7	46						
	Drilled, not cored.			122.80			125.80					
11	Gabbronorite	17R-1, 1	0	125.80	19R-1, 8	48	140.98	142.26	5.58	M		
12	Olivine-plagioclase-phyric basalt	19R-1, 9	48	140.98	19R-1, 20	139	142.19	145.60	0.91	S	I	I
13	Gabbronorite	20-1, 1	0	145.60	20R-3, 17	147	148.91	150.47	3.28	M		
	Wash	21W-1, 1	0	154.50	21W-1, 5	28	154.78					

[a] Contact description: Type: (S) sharp, (M) missing. Nature: (SI) sutured igneous, (I) intrusive. Morphology: (I) irregular, (P) planar.
[b] cm = depth in core measured from top of section.
[c] mbsf = curated depth in hole.
[d] See "Igneous Petrography" section, "Explanatory Notes" chapter for definition.
[e] Texture: P = poikilitic; E = equigranular; Po = porphyritic; V = varitextured.
[f] Grain size: F = fine; M = medium; C = coarse.

with large anhedral pyroxenes enclosing chadacrysts of tabular plagioclase and rounded olivine. Olivine also occurs as typically subhedral to subrounded, 1- to 2-mm-sized grains and is usually partly or completely replaced by amphibole. Secondary sulfide grains often occur in the centers of these altered olivines. Orthopyroxene is commonly in contact with variably degraded olivines.

Gabbros

Many of the gabbros in Hole 894F are strongly metamorphosed and deformed. As a result, identification of primary mineralogy, particularly pyroxene, is difficult. Those gabbros with relatively well-preserved primary igneous mineralogies almost ubiquitously contain some orthopyroxene, generally as oikocrysts.

In several intervals within Hole 894G, foliated, orthopyroxene-poor, medium-grained gabbros contain patches of coarser-grained gabbronorite on a centimeter scale. The sutured igneous contacts between the two lithologies can be either gradational or sharp and in places can be traced through several sequential pieces of core.

Fe-Ti oxide minerals account for generally less than 1 modal percent of this lithology. As in the gabbronorites, these oxide minerals vary between a uniform and a patchy distribution. Characteristically, interstitial magnetite is intergrown with laths and discrete blebs of ilmenite in varying proportions. Fe-Ti oxide minerals range in size up to 1 mm. Spongy to subangular, very fine-grained crystals of pyrite and chalcopyrite are common along exsolution lamellae and silicate mineral margins. These sulfide minerals rarely exceed 0.5 mm in size and average approximately 0.2 mm.

Olivine Gabbro

The best example of olivine gabbro from the two holes studied is a nearly fresh sample with originally 8 modal percent olivine that was sampled from the lowermost part of Section 147-894F-3R-1 (Piece 17) (Fig. 11). Half of the thin section contains medium- to coarse-grained (up to 4.5 mm in size) clinopyroxene and orthopyroxene, which poikilitically enclose small, tabular to subequant plagioclase crystals. Some clusters of plagioclase laths are present, completely surrounded by pyroxene. Particularly near the margins of the large pyroxenes, elongate plagioclase laths are only partially enclosed in pyroxene to form subophitic textures. The other half of the thin section contains much smaller pyroxene crystals and substantially less orthopyroxene in addition to about 15 modal percent olivine. The clinopyroxenes exhibit poikilitic textures enclosing small, subrounded olivine crystals; subophitic and ophitic textures also are common.

Primary Mineralogy

Olivine

Olivine is present throughout the core with a maximum abundance of 10 modal percent in the olivine gabbros. Olivine is typically very altered (see "Metamorphism" section, this chapter), the maximum amount of fresh olivine in Site 894 plutonic rocks being approximately 5 modal percent. Olivine in general displays anhedral to resorbed morphologies and is either rimmed by orthopyroxene or enclosed within large orthopyroxene oikocrysts. This suggests that olivine is in a reaction relationship with the crystallizing evolved

Table 5 (continued).

Unit	Texture[e]	Grain size[f]	Notes
1	P	M	With 2.5% orthopyroxene, 7% olivine, 0.25 oxides (TS 2R-1, 8-10 cm).
2	Po	F	Variable Cr-spinel.
3	V	M	With 1%-10% olivine and trace orthopyroxene (TS).
			Piece 1 is plagioclase-phyric basalt with concave drilled surface and is cleary a piece of breakout. Mixture of gabbronorite, olivine gabbro, basalt fragments.
4	V	M-C	Poikilitic zones (4R-1, 27.5 cm – 4R-2, 40.0 cm; 4R-2, 65.5-121 cm); with <1% oxides; <5% olivine.
5	P	M	<10% olivine pseudomorphs in Piece 1.
6	V	M-C	Poikilitic zones (5R-1, 14.5 cm – 6R-1, 80.0 cm; 6R-2, 38.0 cm – 118.0; 7R-1, 73.0 cm – 9R-3, 33.0 cm); with 5%-15% orthopyroxene; 0.5-2% oxides; <1% olivine; weakly foliated fault breccia at 6R-2, Piece 4; coarse-grained zone at 9R-3, 26-90 cm: with zircon, apatite, sphene, hydrothermal clinopyroxene (TS); 10% oxides in 9R-3, Piece 5.
7	E	M	With 5%-20% orthopyroxene; 5%-10% olivine; 0.1-0.5% oxide.
8	E	M	With 1% oxides; orthopyroxene oikocrysts 10R-1, Piece 11b; magmatic foliation in 10R-1, Pieces 11-13.
9	V	M-C	With 0%-3% olivine; <1-2% oxides.
10	E	M	With <7% olivine; 15% orthopyroxene oikocrysts; <0.5% oxides.
11	V	M-C	With 15%-20% orthopyroxene, <1% oxide; oxide-rich zones in 9R-3, 74-77 cm, and 13R-1, 130-136 cm; 2-4 cm wide, sub-vertical zones of coarse-grained gabbronorite in contact with foliated gabbro (12R-2, 87-120 cm, and 13R-1, 78-94 cm); sharp contact between medium-coarse grained gabbronorite and foliated gabbro (12R-3, 136-150 cm); magmatic foliation well developed in 894G-12R-5, 76-89 cm; poikilitic zones (12R-2, 68 cm – 12R-3, 78.0 cm; 13R-28.5-114 cm; 13R-3, 106-130 cm).
			Gabbronorite fragments.
11	P	M	With 15%-20% orthopyroxene, 1%-2% oxides; sharp contact between coarse- and medium-grained zones in 15R-1, 67-72 cm.
			Assorted rubble.
11	V	M-C	With 3%-20% orthopyroxene; <1% olivine; coarse-grained, oxide-rich zones with apatite, at 17R-1, 79-86 cm; 17R-1, 106-112 cm; slightly coarser grained zones have sharp, sub-horizontal contact with medium-grained host at 18R-2, 21-30 cm.
12	Po	F	Undulatory, brecciated chilled contact with gabbronorite at 61-67 cm, 73-78 cm, 98-102 cm; 109-112 cm, contact is subvertical from 73-78 cm; trace spinel; Piece 13 is coarse-grained gabbronorite.
13	V	M-C	With <2% olivine, 1% oxides; Poikiolitic zones: 20R-1, 6-139 cm; 20R-2, 12 cm – 20R-3, 26.5 cm; 20R-3, 33-128 cm; coarse-grained, oxide-rich zones with apatite and zircon: 20R-1, 0-5 cm; 20R-2, 0-18 cm; 20R-3, 28-33 cm; contact between gabbronorite and foliated gabbro at 20R-2, 16-19 cm.
			Assorted gabbronorite rubble.

Table 6. Summary of recovered rock types for Site 894G.

	Curated thickness (m)	Number of units	Recovery (%)
Olivine gabbro	1.72	2	3.48
Gabbronorite	39.39	5	80.03
Olivine gabbronorite	2.79	3	5.67
Gabbro	1.80	1	3.66
Basalt	3.52	2	7.15
Total	49.22	13	100.00

magma. The olivine has a slightly pale yellowish color in plane-polarized light, which suggests that it is relatively Fe-rich.

Orthopyroxene

Orthopyroxene in the Site 894 gabbronorites has a maximum modal abundance of 20% (15% fresh), occurring as either large anhedral oikocrysts or as euhedral to subhedral granular "primocrysts." Orthopyroxene is unzoned and displays exsolution textures. It is strongly pleochroic with X = pale pink, Y = pale yellow, and Z = pale green. Orthopyroxene also is characterized by high relief and a relatively high birefringence (~0.016–0.018). Combined with an estimated $2V_x$ of ~55°, this suggests that it is hypersthene to ferrohypersthene with $Mg/(Mg + Fe^{2+})$ (Mg#) of 60–40.

Plagioclase

Plagioclase is generally the least altered of the silicate phases and on average represents 53% of the mode of the plutonic rocks. In general, it exhibits tabular, lath-like, subhedral to euhedral morphologies. Plagioclase always displays some form of zoning, most commonly oscillatory but also more complex types. Because of the marked zoning in the plagioclase, it is difficult to determine an average composition. An attempt was made to optically estimate plagioclase compositions on relatively unzoned euhedral plagioclases throughout the core. This estimate provided an average anorthite content of between An_{40-50} (andesine) and as low as An_{30} (oligoclase) in the coarse-grained, oxide-rich intervals. However, due to the evident strong and complex zoning present in the plagioclase, a wide range in compositions is probably present, even in single thin sections.

Clinopyroxene

Clinopyroxene on average accounts for 32 modal percent of the plutonic rocks. It displays anhedral morphologies, occurring as large oikocrysts and as equigranular grains with plagioclase. It is unzoned, displaying numerous exsolution lamellae. Clinopyroxene has a pale pleochroism to light greenish tinge, heightened by the formation of secondary oxides along cleavage planes and exsolution lamellae, suggesting an augitic composition.

Oxide Minerals

The plutonic rocks contain primary igneous ilmenite and magnetite, which commonly occur together and are now affected by exsolution and alteration. The abundance of oxide minerals is quite variable; little evidence of secondary remobilization is present. Patches of oxide gabbronorite with more than 5% oxide minerals occur in Hole 894G, in which most of the plutonic rocks have less than 2% oxide minerals by volume. Between Sections 147-894G-12R-5 and 147-894G-13R-1 (101 to 103 mbsf), oxide minerals are more abundant than elsewhere in the core and form layers that dip at approximately 30°–40° degrees relative to the core axis, a lower angle than associated subvertical, coarse igneous patches that cut the core. Below this zone, the percentage of oxide minerals decreases again to 1% or less

Table 7. Primary modal mineralogies for Holes 894F and 894G, grouped according to lithology.

Core, section, interval (cm)	Piece	Rock type	Ol	Cpx	Opx	Plag
147-894						
G 4R-1, 113-120	16	Gabbronorite		30.0	15.0	55.0
G 4R-2, 67-71	10	Gabbronorite		30.5	7.2	59.7
G 5R-1, 28-30	5	Gabbronorite	0.4	36.9	6.5	55.6
G 6R-1, 26-28	4A	Gabbronorite		30.0	15.0	55.0
G 6R-1, 86-89	8A	Gabbronorite		30.0	20.0	50.0
G 6R-2, 82-85	6	Gabbronorite		35.0	20.0	45.0
G 7R-1, 75-77	13	Gabbronorite		20.0	15.0	65.0
G 7R-2, 35-38	4	Gabbronorite		32.1	16.5	50.5
G 8R-1, 39-42	5A	Gabbronorite		29.5	15.0	55.0
G 8R-1, 56-58	5A	Gabbronorite		25.0	20.0	55.0
G 8R-1, 126-130	10	Gabbronorite		34.0	10.0	55.0
G 9R-3, 71-77	5C	Gabbronorite		30.0	10.0	50.0
G 10R-1, 85-87	13A	Gabbronorite		39.0	5.0	55.0
G 11R-2, 42-44	5	Gabbronorite		40.0	10.0	50.0
G 11R-3, 12-14	2	Gabbronorite		30.0	20.0	47.5
G 12R-2, 42-44	4	Gabbronorite		17.0	17.0	62.5
G 12R-2, 56-58	4F	Gabbronorite		25.0	15.0	60.0
G 12R-2, 91-96	9A	Gabbronorite		20.0	20.0	52.5
G 12R-3, 142-148	8	Gabbronorite		44.0	5.0	50.0
G 12R-4, 122-126	13	Gabbronorite	2.0	40.0	7.5	50.0
G 12R-5, 84-88	9	Gabbronorite		27.0	15.0	45.0
G 13R-2, 10-13	2	Gabbronorite		14.4	18.6	61.8
G 13R-2, 88-90	8	Gabbronorite		29.2	21.0	49.4
G 13R-3, 13-15	1B	Gabbronorite		30.6	13.2	55.1
G 15R-1, 77-80	12	Gabbronorite		50.0	30.0	20.0
G 17R-1, 52-54	10A	Gabbronorite		50.0	5.0	45.0
G 18R-1, 65-70	10	Gabbronorite		25.0	15.0	60.0
G 20R-1, 19-22	4	Gabbronorite		37.4	7.6	55.0
G 20R-2, 14-16	2	Gabbronorite		33.3	9.8	53.7
G 20R-2, 56-59	10	Gabbronorite		25.0	10.0	45.0
G 20R-3, 59-62	9	Gabbronorite		32.8	12.1	51.3
G 7R-1, 62-68	11	Olivine gabbronorite	5.0	30.0	15.0	50.0
G 9R-3, 138-142	11	Olivine gabbronorite	5.0	30.0	15.0	50.0
G 9R-4, 133-135	11	Olivine gabbronorite	10.0	30.0	5.0	55.0
G 11R-3, 45-49	6A	Olivine gabbronorite	7.0	30.0	15.0	47.5
G 13R-1, 132-136	14	Oxide gabbronorite		30.0	12.0	50.0
G 19R-1, 92-95	13	Oxide gabbronorite		30.0	15.0	50.0
F 2R-1, 5-7	1	Gabbro		46.6		51.1
F 3R-1, 30-33	5	Gabbro		48.0		50.6
G 2R-3, 11-14	3	Gabbro	1.5	45.6		52.1
G 2R-3, 32-35	5	Gabbro	4.0	45.0		35.0
G 2R-3, 49-52	6	Gabbro		50.0		50.0
G 2R-3, 78-80	11	Gabbro		45.0		55.0
G 9R-3, 48-52	4	Gabbro		35.0		50.0
G 10R-1, 47-50	10	Gabbro	4.0	37.0	4.0	52.5
G 11R-2, 97-100	10	Gabbro		45.0		55.0
G 17R-1, 116-118	14	Gabbro		35.0	3.0	60.0
G 18R-2, 23-26	4A	Gabbro		42.0	3.0	55.0
G 18R-2, 97-99	14	Gabbro		42.5		57.0
G 20R-2, 16-19	2	Gabbro		23.4		75.7
F 3R-1, 103-105	17	Olivine gabbro	8.0	44.3	0.8	46.1
G 2R-1, 8-10	2	Olivine gabbro	7.4	36.2	2.2	53.5
G 2R-3, 118-120	14	Olivine gabbro	11.4	39.2	0.3	48.7

Notes: Ol = olivine; Cpx = clinopyroxene; Opx = orthopyroxene; Plag = plagioclase.

in foliated finer-grained gabbro. Coarser, more equigranular gabbros found in this lower part of the section may have up to 10% oxide minerals but only in very restricted areas.

The texture of the oxide minerals remains predominantly interstitial throughout, except in the less-deformed, coarser patches where they are equant or lath shaped. The interstitial minerals form locally thin cuspate-shaped grains between the silicates. They may also partially to totally enclose silicates (Fig. 9) or, where interstitial between plagioclase, make up subangular cross sections. Interstitial oxide minerals are disseminated throughout the core and are found in contact with all major igneous silicates. Although they show exsolution, their primary textures are well preserved; only rarely, in the most altered parts of the core, do the oxide phases appear to have been altered.

Sulfide Minerals

Although most of the sulfide minerals are secondary, primary sulfide minerals occur in contact with interstitial oxide minerals and rarely occur as inclusions in oxide minerals. In these cases the sulfide minerals are rounded and globular, which suggests that they may be related to the magmatic crystallization of the oxide minerals. A second primary association of oxide and sulfide minerals occurs where an ilmenite layer (Sample 147-894G-13R, 130–137 cm; at 103.4 mbsf) that is barren of sulfides has a concentration of sulfide minerals just above it. These sulfide minerals are now low-temperature forms, but may have crystallized in association with the ilmenite layer and subsequently may have been altered in situ.

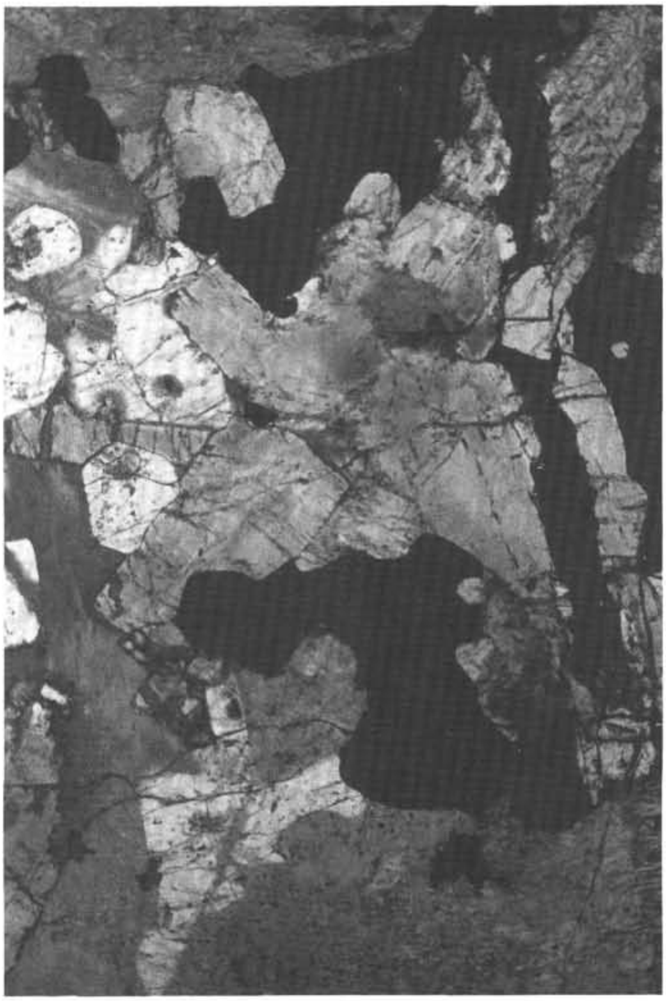

Figure 9. Photomicrograph of an oxide gabbronorite. Tabular plagioclase (gray) is intergrown with magnetite (black) (Sample 147-894G-13R-1, Piece 14, 132–136 cm; field of view is 5 mm).

Accessory Minerals

Zircon and apatite occur in several specimens, particularly in very coarse-grained gabbronorites. Both minerals are considered to be primary, late magmatic (deuteric) accessory minerals and are associated with primary oxide minerals and dark green amphibole (which may be deuteric?). In Section 147-894G-9R-3 (Pieces 4 and 5A), zircon forms euhedral prismatic crystals with habits ranging from rhombic to needle-shaped (Fig. 12). Clusters of these euhedral crystals, which range up to 0.8 mm maximum dimension, are found adjacent to oxide minerals with which they may be intergrown. Zircon is unusually abundant in these patches (although still less than 1% by volume) and thus confirms the evolved nature of the coarse-grained gabbronorite.

Apatite generally occurs as small, stubby crystals ranging up to 0.4 mm in maximum dimension, although in Section 147-894G-17R-1

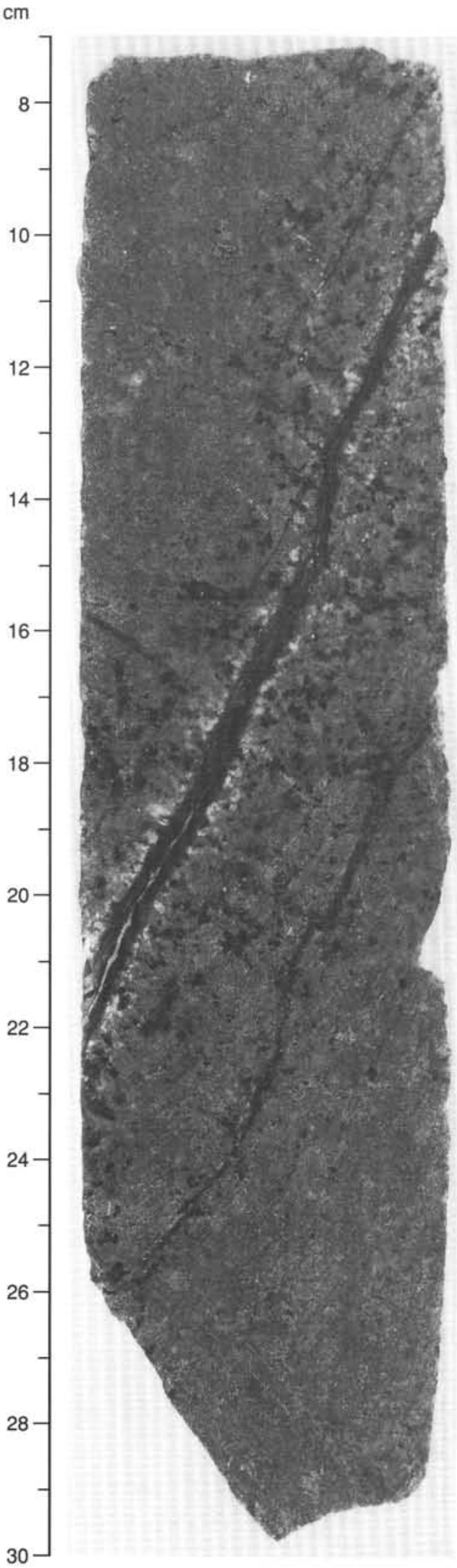

Figure 10. Photograph of an olivine gabbronorite (Sample 147-894G-9R-4, Piece 2, 7–30 cm). Alteration halo along vein highlights olivine crystals.

Figure 11. Photomicrograph of an olivine gabbro exhibiting a poikilitic texture with oikocrysts of clinopyroxene (Cpx) including plagioclase and olivine (Ol) chadacrysts (Sample 147-894F-3R-1, Piece 17, 103–105 cm; field of view is 5 mm).

(Piece 6) it occurs as acicular needles up to 1 cm long (and partly enclosed in amphibole?) (Fig. 13). Apatites are typically rich in primary and secondary fluid inclusions (see "Metamorphism" section, this chapter).

Relationships Among Different Lithologies

Textural Variations

The plutonic rocks display significant variations in texture. The most common textures are poikilitic and equigranular hypidiomorphic (Fig. 14A, -B). Poikilitic texture most frequently involves orthopyroxene oikocrysts, but poikilitic clinopyroxene is also common. Oikocrysts of orthopyroxene commonly surround resorbed olivine chadacrysts. In equigranular gabbronorite, olivine is absent. Varitextured rocks that exhibit changes in texture on the scale of a thin section are common. Patches of equigranular gabbronorite are found within poikilitic gabbronorite in several sections of core. Also common are scattered oikocrysts of orthopyroxene in an otherwise equigranular rock. The textural relationship between plagioclase and clinopyroxene may change over small distances from equigranular to poikilitic, or to domains where the two minerals are characterized by globular intergrowths. In a number of sections, large intervals of the core alternate between poikilitic and equigranular textures. This may be a layering phenomenon or may represent large patches of one textural type within

Figure 12. Reflected light photomicrograph of euhedral zircon (white) in coarse-grained gabbronorite (Sample 147-894G-9R-3, Piece 4, 48–50 cm; field of view is 1.5 mm).

the other. We note that equigranular gabbronorite increases in abundance and becomes coarser grained toward the lower half of the recovered core (Fig. 6).

Grain Size Variations

The average grain size of plagioclase in Hole 894G core varies from 1 to 8 mm, with an average of approximately 3 mm (Appendix A on CD-ROM; see Fig. 10 of "Explanatory Notes" chapter for example). The average grain size increases slightly with depth in Hole 894G, with more coarse-grained rocks found in Core 147-894G-12R and below (Fig. 6). A similar increase in grain size downhole is exhibited by the oxides. The maximum average grain size observed for the oxides in the upper part of Hole 894G is 1–2 mm, whereas the maximum average grain size close to the base of the hole is 5–6 mm (neglecting a single piece with an average grain size of nearly 10 mm). Rocks with relatively finer grain sizes, however, continue to be present throughout the core. Therefore, the observed increase in grain size downhole seems due to a more frequent appearance of medium- to coarse-grained and coarse-grained rocks. There is a wide range in grain size of both plagioclase and oxides on a small scale. Medium-grained rocks cut by veins or patches of coarser-grained rocks commonly occur. The largest grain sizes are found in the more equigranular rocks.

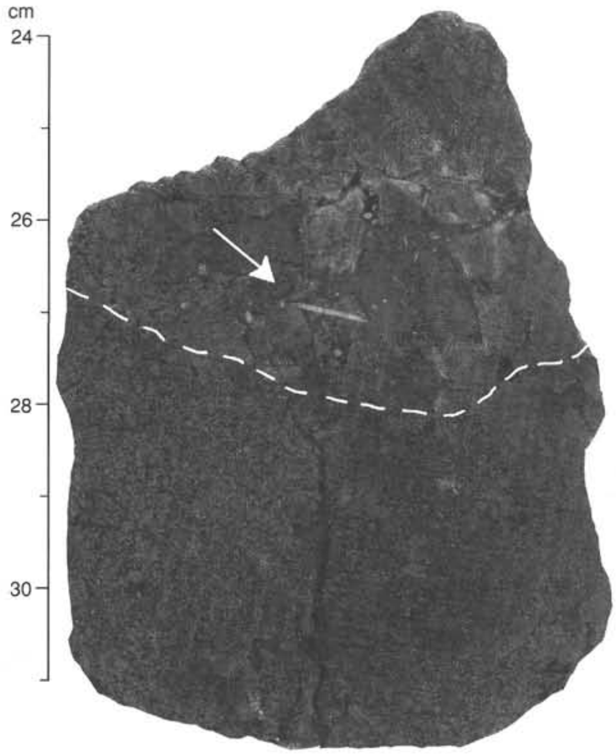

Figure 13. Photo of a coarse-grained patch of gabbronorite with centimeter-long needles of apatite (arrow) (Sample 147-894G-17R-1, Piece 6, 24–31 cm).

Relationship Between Magmatic Foliation and Lithology

Magmatic foliation, defined by the alignment of tabular plagioclase crystals, is locally developed in the middle and lower parts of Hole 894G. Foliation is particularly well developed in Cores 147-894G-8R, -10R, -12R, -13R, -19R, and -20R (i.e., from 70 to 150 mbsf); (see "Structure" section, this chapter). Within these cores the foliation is intermittent and grades from unfoliated poikilitic gabbronorite to foliated gabbro and gabbronorite, and can be distinguished on both macroscopic and microscopic scales. The magmatic foliation is most common in rocks of medium grain size. Where magmatic foliation is developed in medium-grained poikilitic gabbronorites, orthopyroxene is either drastically reduced in abundance or completely lacking in the rock.

Magmatic foliation is commonly found adjacent to coarse-grained gabbronorite. In the sample illustrated in Figure 15A, the foliation is developed along the margins of a 2- to 3-cm-thick tabular body of equigranular gabbronorite. A thin section taken across this tabular body demonstrates that the foliation is locally inclined to the contact, and that the medium- to coarse-grained gabbronorite is unfoliated (Fig. 15B), clearly indicating that the latter represent a vein. The coarse grain size and lack of chilling along the margins suggest that the foliation formed at a late magmatic stage.

Preliminary Interpretation and Comparison of the Plutonic Sequence

In Holes 894F and 894G, olivine gabbros, poikilitic gabbronorites and equigranular gabbronorites are interrelated in a complex fashion. We note that a possible fractionation sequence would be from olivine gabbro to poikilitic gabbronorite to equigranular gabbronorite. This sequence represents the crystallization order: (1) olivine-plagioclase-

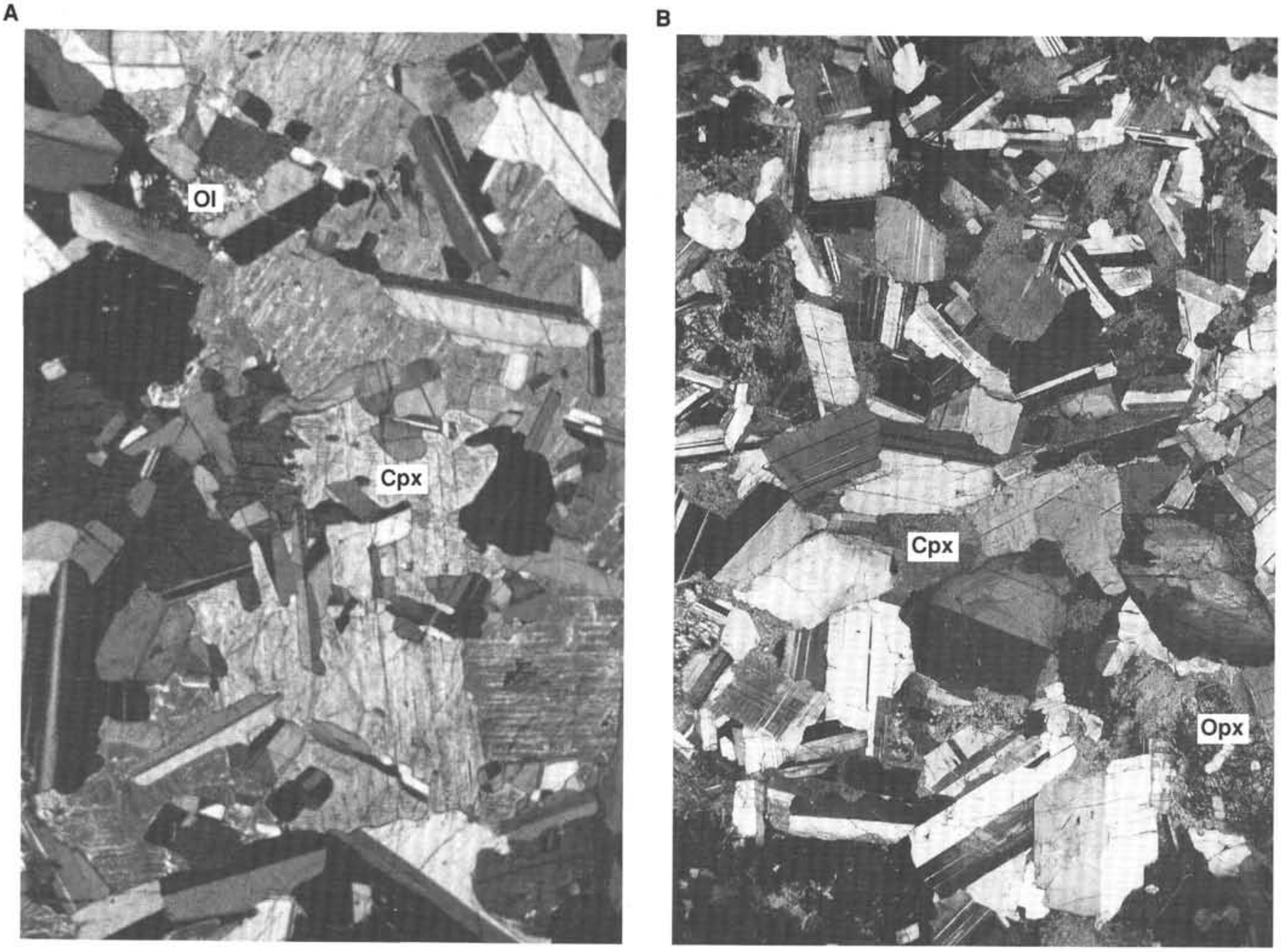

Figure 14. Photomicrographs showing the principal textural types seen in Holes 894F and 894G. **A.** Poikilitic texture in an olivine gabbro with chadacrysts of subhedral plagioclase laths and olivine (Ol) enclosed in a clinopyroxene (Cpx) oikocryst (Sample 147-894F-3R-1, Piece 17, 103–107 cm; field of view is 5 mm). **B.** Typical equigranular texture in gabbronorite (Sample 147-894G-4R-1, Piece 16, 113–120 cm; field of view is 5 mm); Cpx = clinopyroxene, Opx = orthopyroxene.

clinopyroxene, (2) orthopyroxene (olivine/melt reaction)-plagioclase-clinopyroxene, and (3) orthopyroxene-plagioclase-clinopyroxene co-crystallization.

The change from olivine gabbros in Hole 894F and in the upper parts of Hole 894G to gabbronorites, and the gradual appearance of more and more equigranular gabbronorites further down in the core (with a maximum between 100 and 120 mbsf) suggest that the rocks crystallized from progressively more evolved magma downhole. This is consistent with the general decrease in the Cr-content of the rocks from about 700 ppm at 17 mbsf in Hole 894F to less than 100 ppm at 105 mbsf in Hole 894G (see "Geochemistry" section, this chapter). The presence of several olivine gabbronorite units (i.e., Units 5, 7, and 10; Table 5) between these levels may reflect smaller-scale fluctuations in magma compositions, possibly related to episodic influx of magma.

The occurrence of numerous patches of coarse gabbronorite adjacent to magmatically foliated orthopyroxene-lacking gabbro suggests that filter-pressed segregations locally formed from a surrounding foliated host. This indicates that accumulation and flow of interstitial melts may have played an important role at this level in the crust.

With respect to the general stratigraphy of the Hess Deep intrarift Ridge (Francheteau et al., 1990; Hekinian et al., 1993), Site 894 is at the top of a long sequence of exposed plutonic rocks that trend downslope from gabbro to primitive olivine gabbro, troctolite, dunite, and tectonized serpentinite in the floor of Hess Deep. Gabbro from the North Slope was sampled in three *Alvin* dives just below the base of the sheeted dike sequence (J. Natland, unpubl. data). In a general descending stratigraphic order, they change from gabbro of basaltic composition to gabbro cumulates. The gabbro cumulates, which occur about 200 m below the base of the sheeted dike sequence, texturally and geochemically show significant effects of cumulus processes and consist primarily of gabbro, gabbronorite, and norite that lack olivine and contain low (<1%) percentages of primary interstitial oxides.

In a compositional and a quasi-stratigraphic sense, Site 894 appears to lie between the two extremes represented by the North Slope (olivine-absent) and the lower intrarift ridge at Hess Deep (olivine-bearing rocks). Olivine is present in many of the cored samples, but the preponderance of orthopyroxene- and oxide-bearing varieties suggests that the rocks are more evolved than most of those described by Hekinian et al. (1993).

The rocks of Site 894 match lithologies encompassed by olivine-poor gabbro, gabbronorite, and disseminated-oxide gabbro at Hole 735B. The fairly primitive troctolites and olivine gabbros cored at Hole 735B were not recovered from Hole 894G, and neither was trondhjemite or otherwise felsic dikelets found associated with Fe-Ti oxide gabbro at Hole 735B. The range of rocks in the 500-m hole at Hole 735B matches the range found in all localities within Hess Deep. Only

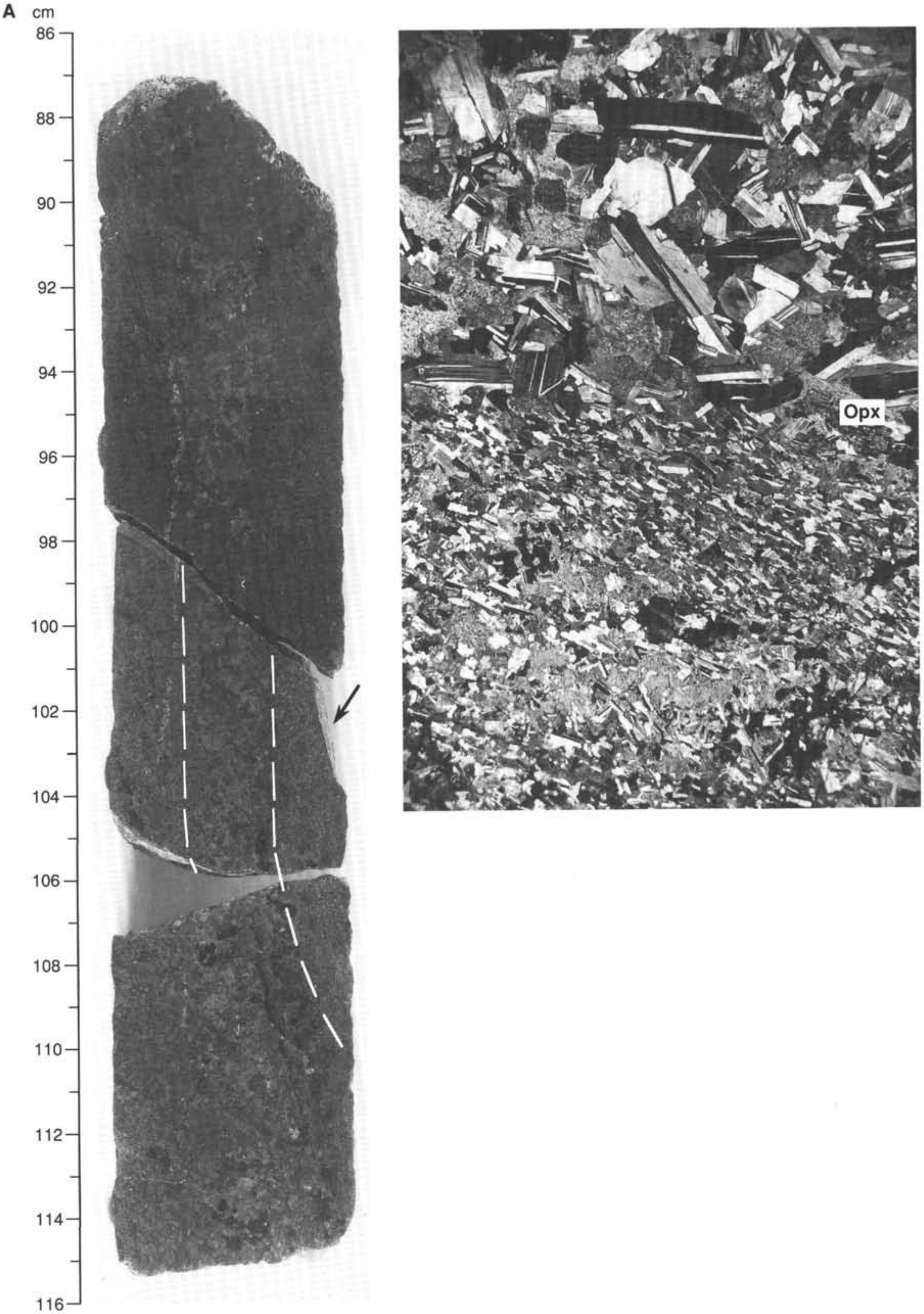

Figure 15. **A.** Photograph showing a 2- to 3-cm-thick vein of coarse-grained and equigranular gabbronorite in a medium-grained gabbro. Note that a pronounced magmatic foliation is at a low, oblique angle to the vein; arrow marks foliation direction; dashed lines show boundaries between gabbro and gabbronorite (Sample 147-894G-12R-2, Pieces 9A, 9B, and 10B, 86–116 cm). **B.** Photomicrograph of the vein shown in Figure 15A (field of view is 4 cm). Note how the magmatic foliation, defined by a parallel orientation of tabular plagioclase, is cut by the unfoliated, coarse-grained gabbronorite vein. Orthopyroxene (Opx) is not present in the strongly foliated rock, but occurs as oikocrysts in the unfoliated, coarse-grained gabbronorite (Sample 147-894G-12R-2, Piece 9A, 91–96 cm).

the primitive olivine gabbro and troctolite in Hess Deep sampled by *Nautile* (Hekinian et al., 1993) have no generic equivalents at Hole 735B.

The rocks recovered in Holes 894F and 894G also bear a marked resemblance to lithologies found in the upper plutonic sections of many ophiolites. This is particularly true of their lack of well-developed modal layering, their varitextured nature, and the presence of evolved rock types containing accessory minerals such as zircon and apatite.

Petrographic Description of Basaltic Dikes

Two pieces of aphyric basalt were recovered at Hole 894F. No phenocrysts are present, but a sutured igneous contact with olivine gabbro is seen in Section 147-894F-3R-1 (Piece 19). The basalt is microcrystalline and appears to have a chilled margin that is somewhat more altered than the rest of the rock.

Two basaltic dikes were sampled in Hole 894G (Section 147-894G-2R-1, 15 cm, to Section 147-894G-2R-2, 127 cm; Section 147-894G-19R-1, 49 to 139 cm). Both of these are porphyritic, with up to 15% phenocrysts of plagioclase, olivine, and Cr-spinel, in order of abundance. The upper dike is medium-grained with a subophitic texture, whereas the lower dike was quenched against cold country rock to glassy-spherulitic groundmass textures. The lower dike exhibits marked flow differentiation, with phenocrysts concentrated within 0.5 cm of the dike contact, and again at distances more than 1.3 cm from the contact (Fig. 16). In between, there are very few phenocrysts. Throughout, plagioclase microlites are strongly preferentially oriented parallel to the dike contact.

The olivine phenocrysts in both dikes are partly to completely altered to dull green clay minerals, but the groundmass is relatively unaltered, with fresh plagioclase and clinopyroxene. In the upper dike, skeletal titanium-rich magnetite is only slightly altered to titanium-rich maghemite along small fractures. In the spherulitic groundmass of the lower dike, only traces of tiny titanomagnetite crystals were observed between microlites of plagioclase.

The plagioclase phenocrysts in both dikes range from tabular or equant microphenocrysts to large subhedral megacrysts up to 1 cm in size, with numerous melt inclusions. Together, they comprise up to 10% of the rocks. Some megacrysts are intergrown with altered olivine. Olivine phenocrysts are euhedral to subhedral. The Cr-spinel phenocrysts are unevenly distributed in the upper dike, being numerous in two thin sections and rare in a third. They are numerous in the lower dike. In both dikes, the spinels are reddish amber to reddish brown. The larger spinels form imperfect euhedral crystals with equant shapes, often with skeletal overgrowths or resorption/reequilibration margins (Fig. 17). Such spongy margins are not present on spinel phenocrysts at the very fine-grained quench margin of the lower dike (in the outer 0.5-cm contact zone), but they are present and become wider with distance from the contact. Similar margins are wider still in the coarser-grained upper dike; some crystals are entirely skeletal. The larger spinels often contain silicate inclusions. Tiny perfect octahedra of Cr-spinel are also present in the groundmass of both dikes.

Sulfide minerals are rare and almost completely secondary, located in zones of alteration. Pyrrhotite and chalcopyrite form locally composite grains that may have a primary origin.

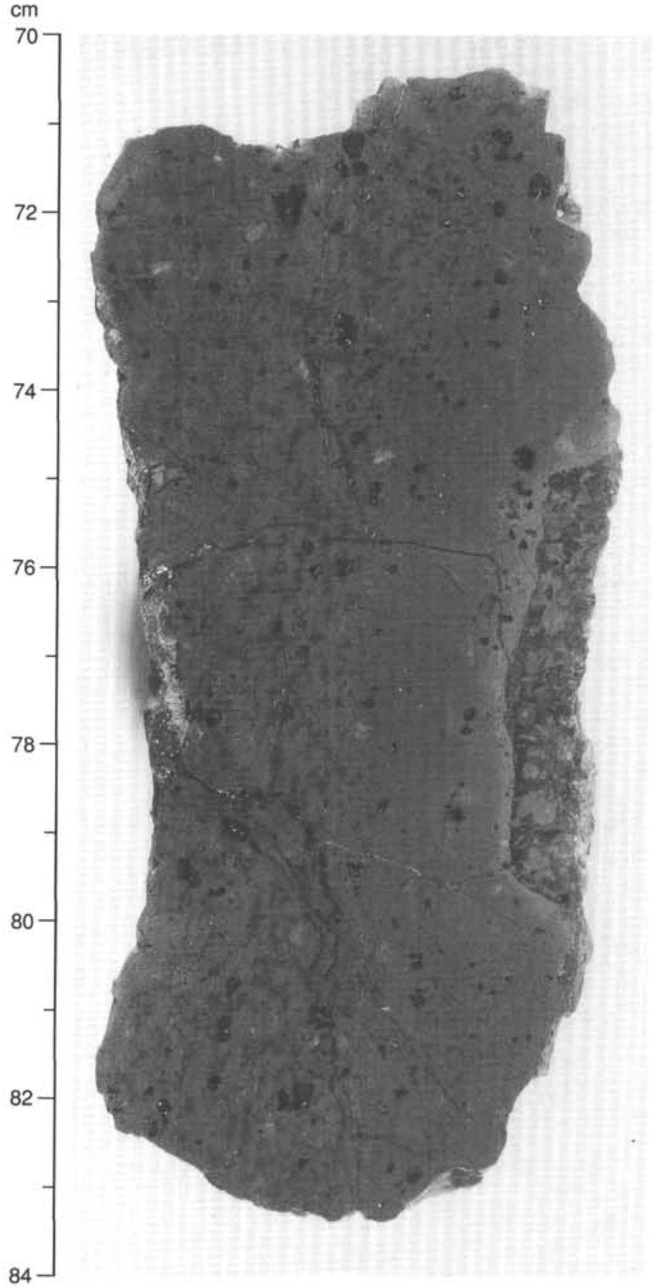

Figure 16. Photograph showing the primary igneous contact between gabbronorite and a plagioclase, olivine, spinel-phyric basalt. Note that the dike is chilled against the contact, and that phenocrysts (probably due to flow differentiation) are concentrated within 0.5 cm of the dike contact, and again at distances more than 1.3 cm from the contact (Sample 147-894G-19R-1, Piece 12, 70–84 cm).

Preliminary Interpretations and Comparisons of the Basaltic Dikes

The observations made on the porphyritic dikes recovered from Hole 894G point to the following general conclusions. First, based on phenocryst assemblages, the Hole 894G dikes seem to represent primitive magmas. Second, the lower dike was quenched against cold country rock. Third, the dikes did not experience the pervasive background alteration to lower amphibolite facies mineral assemblages experienced by the surrounding gabbros. There is evidence instead that pre-existing secondary sulfides in the gabbros were disturbed by injection of the dikes (marcasite was only found in gabbros near the dike; see "Metamorphism" section, this chapter). These conclusions indicate that the dikes may have been emplaced late in the history of rocks at Site 894, after the initial high-temperature hydrothermal alteration of the gabbros, and after they had cooled substantially. Therefore, it is questionable whether these rocks formed at the East Pacific Rise and whether they are related to the plutonic sequence. This doubt is substantiated by a complete absence of similar porphyritic rocks and the scarcity of primitive lavas in general, among axial extrusives of the East Pacific Rise both in this area (i.e., at both North Slope and South Slope *Alvin* dive and dredge localities in and near Hess Deep; J. Natland and K. Nilsson, unpubl. data) and regionally (Morel and Hekinian, 1980; Natland, 1980). Glassy pillow lavas with phenocryst assemblages similar to those seen in the dikes have been obtained in one dredge haul with serpentinized ultramafic rocks on the flank of the intrarift ridge about 2 km to the southeast of Site 894 (Dredge AII-125-4D; J. Natland and K. Nilsson, unpubl. data). These lavas clearly represent a very young extrusion on top of altered peridotite, and are probably basalts injected from the tip of the Cocos-Nazca spreading center, now propagating in a westerly direction. The dikes are also petrographically similar to porphyritic basalts found at Siqueiros Fracture Zone on the East Pacific Rise (Natland, 1980; 1989), at small, off-axis seamounts (e.g., Allan et al., 1989), and at eastern Pacific ridges spreading at intermediate rates (e.g., Hole 504B at the Costa Rica Rift; Natland et al., 1983).

METAMORPHISM

Introduction

Gabbros from Site 894 provide a unique opportunity to assess the nature of metamorphism and water-rock interaction in plutonic rocks formed at the fast-spreading East Pacific Rise (EPR). The 150-m penetration in Hole 894G represents the first core recovery of gabbros from this environment and allows comparison with the well-studied metamorphic and hydrothermal processes found at slow-spreading oceanic systems such as the Southwest Indian Ridge and Mid-Atlantic Ridge near the Kane Fracture Zone (MARK) (e.g., Mével and Cannat, 1991; Stakes et al., 1991; Gillis et al., in press; Kelley et al., in press).

Variably altered and deformed gabbroic and basaltic rocks recovered from Hole 894 record a complex history of interaction between magmatic, hydrothermal, and deformational processes. The rocks are characterized by a pervasive background static metamorphism at amphibolite down to zeolite facies, which is associated with brittle deformation in the form of anastomosing amphibole-filled microveinlets and millimeter-wide amphibole veins and vein networks (Table 8). Evidence from apatite-hosted primary fluid inclusions in coarse-grained pods of gabbronorite indicates that, locally, the earliest hydrothermal event involved magmatic fluids. This initial event may be expressed mineralogically by the local development of coarse-grained amphibole. The static metamorphism and associated vein formation requires the migration of seawater-derived fluids through the gabbros from >500°C to ambient temperatures, and is consistent with the generation of permeability primarily by thermal contraction of the cooling gabbros. With progressive cooling of the gabbroic rocks, circulation of fluids increased, leading to the development of actinolite, chlorite + prehnite and chlorite ± smectite ± zeolite veins and concomitant wall-rock alteration. In local cataclastic zones where deformation allowed enhanced penetration and circulation of evolved Ca-rich fluids, fluid-rock interaction was most intense, leading to pervasive recrystallization and alteration of the gabbroic host rock to greenschist facies mineral assemblages. The absence of a high-temperature, synkinematic metamorphic assemblage in gabbroic rocks from Hess Deep is in marked contrast to gabbroic samples recovered at Site 735B, in which ductile shearing and penetration by fluids at granulite facies conditions strongly influenced the magmatic and metamorphic evolution (Stakes et al., 1991; Dick et al., 1992).

Static Metamorphism

Alteration of Primary Minerals in Gabbroic Rocks

Variably altered and deformed gabbroic rocks recovered from Site 894 record static metamorphism under amphibolite to zeolite facies conditions. Mineral assemblages defining distinct metamorphic zones are absent, overprinting of higher temperature secondary minerals by lower temperature phases is common, and intensity of alteration downhole is heterogeneous (Fig. 18; Appendix B on CD-ROM; see Fig. 11 of "Explanatory Notes" chapter for example). In general, background alteration intensity is governed by replacement of pyroxene. The most intensely altered sections of the core are related to formation of cataclasites and to densely veined zones. At least 80% of the gabbros drilled at Site 894 are affected by 20%–50% background replacement of primary minerals, with more altered local intervals displaying 50%–100% replacement. Samples exhibiting less than 15% modal alteration are extremely rare (Table 8).

Olivine

Olivine alteration is highly variable, involving complex and heterogeneous coronitic replacement. Alteration is commonly pervasive; however, some samples contain up to 90% relict olivine. Irregular concentric zoning of olivine commonly involves cores that contain varying amounts of green to pale yellow mixed-layer chlorite-smectite, olive brown-yellow smectite, iddingsite, and more rarely talc and carbonate (Fig. 19A). Moving outward from the core, these minerals are rimmed by or intergrown with fibrous pale green to colorless amphibole (tremolite?) and fine-grained magnetite. Where olivines are in contact with plagioclase, pale green fibrous chlorite with anomalous blue birefringence commonly forms the outermost rim. Fine-grained magnetite is pervasive along crosscutting microfractures and as concentrated bands that mimic original grain boundaries. In samples where olivines are enclosed by orthopyroxene, fibrous amphibole (cummingtonite?) is commonly the dominant alteration phase, forming fine-grained intergrown mats enclosing olivine pseudomorphs. In any one sample, these mineral zonations are highly variable and one or more alteration phases may be absent. Olivines are rarely cut by liquid to vapor-rich anhedral fluid inclusion arrays. In hand sample, altered olivine is characterized by an iron red color,

Table 8. Summary of metamorphic characteristics at Site 894.

	Mineralogy			
Lithology	Primary	Secondary	Vein types	Metamorphic intensity
Gabbroic rocks	Olivine	Mixed-layer chlorite/smectite, smectite, tremolite, cummingtonite, iddingsite, talc, carbonate, magnetite, pyrite	(1) Amphibole (2) Chlorite ± prehnite ± actinolite ± epidote (3) Chlorite ± smectite ± zeolite ± calcite	Amphibolite to zeolite facies, 20% to 100% altered
	Clinopyroxene	Pale brown amphibole, green to yellow-green amphibole, secondary clinopyroxene, smectite, pyrite, magnetite		
	Orthopyroxene	Pale green amphibole (cummingtonite?), talc, serpentine, chlorite, smectite, magnetite		
	Plagioclase	Secondary plagioclase, smectite, zeolite, clay, actinolite, chlorite, epidote		
	Ilmenite	Titanite		
Basaltic dikes	Olivine	Smectite, chlorite, serpentine?, magnetite, pyrite, clay	(1) Chlorite + actinolite ± titanite, (2) Chlorite + clay (smectite)	Greenschist to zeolite facies, 10% to 85% altered
	Clinopyroxene	Actinolite, chlorite, magnetite		
	Plagioclase	Clay, secondary plagioclase, zeolite, chlorite, smectite		
	Groundmass	Fine-grained amphibole?, zeolite, smectite, clay		

Figure 17. Reflected light photomicrograph of euhedral spinel (Sp) with spongy margin and euhedral titanomagnetite (Mt) in a dike. Smaller laths of titanomagnetite are also present (Sample 147-894G-2R-1, Piece 9, 68–71 cm; field of view is 1.5 mm).

which is due to replacement by iddingsite, and coarse-grained pyrite is common (Appendix B).

Clinopyroxene

Clinopyroxene is the most visibly altered mineral in the gabbros at Site 894, where replacement varies from 10% to 100%. The earliest alteration of clinopyroxene is replacement by trace amounts of fine, anhedral, pale brown amphibole grains. With progressive alteration, clinopyroxenes become turbid, mottled, and brown in plane-polarized light due to pervasive crosscutting of microfractures containing abundant micron-sized (<1–5 μm) anhedral magnetite grains, intergrowths of fine- to medium-grained fibrous pale green to yellow amphibole, and poorly developed secondary hydrothermal clinopyroxene (Fig. 19B). Alteration intensity of such grains may have been overestimated in microscopic analyses due to the fine-grained nature of the alteration products. In some samples, clinopyroxene is green-black in color due to the pervasive abundance of these fine-grained minerals. Localized replacement and veining of smectite forms the latest alteration phase. In the least-altered samples, minor actinolite after clinopyroxene is common.

Secondary clinopyroxene after magmatic clinopyroxene is pervasive throughout the gabbroic section. Where secondary clinopyroxene development is poor, dusty, inclusion-filled patches are formed, pervasively replacing the original pyroxene (Fig. 19B). These inclusion-rich zones typically dominate alteration in the cores of clinopyroxene, and are rimmed by coarser grained secondary clinopyroxene. Coarse-grained secondary clinopyroxene occurs as anhedral, optically continuous translucent to pale green grains. In coarse-grained gabbronorite patches containing apatite and zircon, coarse-grained secondary clinopyroxene is pervasive, and may completely replace primary clinopyroxene. In these grains, primary vapor-dominated fluid inclusions are ubiquitous (see following "Fluid Inclusions" section). The secondary pyroxenes are petrographically similar to those in gabbros recovered from near the Kane Fracture Zone (Kelley and Delaney, 1987; Gillis et al., in press), the Skaergaard Intrusion (Manning and Bird, 1986), and Hole 735B (Stakes et al., 1991; Mével and Cannat, 1991), although secondary clinopyroxene in Hole 735B commonly occurs in veins.

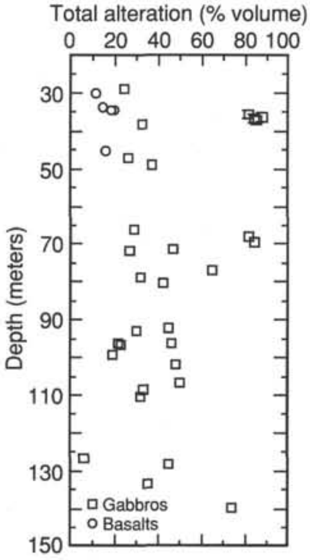

Figure 18. Depth below seafloor vs. total alteration (abundance of secondary minerals) in percent as estimated or point counted in thin sections.

Amphibole after clinopyroxene exhibits complicated and diverse optical zonation and crystal habits. It typically forms fine-grained, fibrous, pale green to colorless radiating actinolitic(?) mats, which rim or completely pseudomorph clinopyroxene and which compose up to 35 modal percent of the gabbros (Fig. 19B). Fine-grained, anhedral pyrite and magnetite are commonly associated with the fibrous actinolitic rims. Pale green chlorite with anomalous blue to low-first order birefringence after actinolite is rare in these zones and, where it is found, is commonly bounded by both clinopyroxene and plagioclase. Coarser grained aggregates of bladed amphibole after clinopyroxene may show well-developed cleavage and are commonly green-yellow, or dark green to blue-green in color. Such amphiboles are especially well developed in coarse-grained pods and patches, and more rarely in gabbros that have undergone minor shearing. Macroscopically, these amphibole-rich pods form up to 1 cm in diameter and give the gabbros a patchy appearance. Formation of coarse actinolitic patches is particularly well developed adjacent to macroscopic veins, presumably due to higher water to rock ratios in these more permeable zones.

Orthopyroxene

In general, alteration of orthopyroxene is similar to that of clinopyroxene, where alteration intensity varies from ≈15% to 100%. Alteration is commonly heterogeneous on a thin-section to hand-sam-

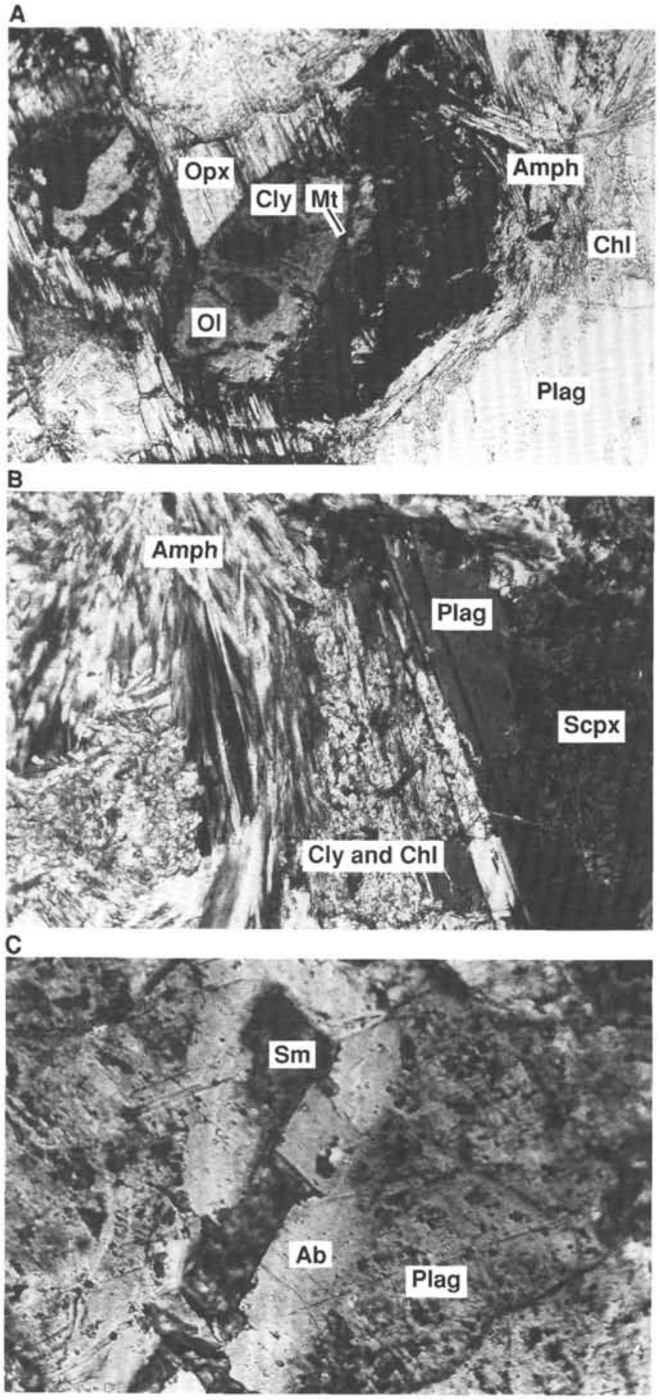

Figure 19. **A.** Poorly developed coronitic replacement of olivine (Ol) by green to yellow mixed-layer chlorite-smectite (Cly), fibrous pale green to colorless amphibole (Amph), chlorite (Chl), and fine-grained, predominantly fracture-bound magnetite (Mt). Olivine is partially enclosed by orthopyroxene (Opx). Olivine alteration is commonly highly variable and heterogeneous on a thin section scale (Sample 147-894G-2R-1, Piece 2, 8–10 cm; field of view is 5.6 mm; crossed polars). **B.** Well-developed amphibole and secondary clinopyroxene (Scpx) after clinopyroxene with pervasive replacement of plagioclase by intergrown chlorite and clay and minor amphibole along microfractures. **C.** Smectite-rich (Sm) pod, rimmed by albite (Ab) in core of plagioclase (Plag) grain (Sample 147-894G-8R-1, Piece 5A, 56–58 cm; field of view is 1.4 mm; plane light).

ple scale. Orthopyroxene is typically turbid, mottled, and brown in plane-polarized light due to pervasive crosscutting microfractures filled with abundant micron-sized anhedral magnetite grains, and intergrowths of very fine-grained, acicular, highly birefringent colorless to pale green amphibole that is probably cummingtonite, with rare talc and serpentine. Fibrous pale green radiating amphibole commonly rims grain boundaries. In zones where alteration minerals are better developed, pale green to pale yellow, coarse-grained bladed amphibole dominates orthopyroxene replacement. Replacement by chlorite is rare, generally comprising less than 1–2 modal percent, and is most common adjacent to throughgoing composite prehnite and chlorite veins. As with clinopyroxene, localized replacement and veining of smectite forms the latest alteration phase.

Plagioclase

Plagioclase alteration ranges from <10% to 100% and predominantly involves the formation of secondary albitic plagioclase, followed by smectite and zeolite replacement (Fig. 19C). Alteration is commonly patchy on a thin-section to hand-sample scale, and is most pervasive adjacent to anastomosing macroscopic vein networks and in cataclastic zones. In highly altered zones, plagioclase is typically turbid and dusty due to variably abundant fine-grained inclusions of clay and zeolite, which comprise up to 20 modal percent. Smectite-rich pods, which locally occur in plagioclase cores, are rimmed by secondary plagioclase (Fig. 19C). Secondary plagioclase commonly forms irregular microveinlets and bands that crosscut and rim primary plagioclase. Locally, in extensively altered patches, secondary plagioclase contains abundant anhedral liquid-dominated fluid inclusions (<5 to 40 µm in size). Very fine opaques, which occur as oriented rods and as rounded inclusions (<1 µm in size) are abundant in some samples. Fine-grained, fibrous sprays of actinolite, which radiate from adjacent altered pyroxene and olivine grains, commonly coalesce to form anastomosing veinlets cutting plagioclase, and actinolite rimming plagioclase grain boundaries is common. Trace epidote forms fine-grained granular grains and more rarely occurs as coarse pale green to yellow grains. Replacement by epidote is best developed in coarse-grained gabbro and gabbronorite patches. Chlorite is rare. Slightly altered plagioclase in hand sample is characterized as translucent and cream colored. In more pervasively altered patches, particularly those adjacent to vein networks, plagioclase is chalk white in color, and yellowish when altered to clay.

Secondary Oxides and Sulfides in the Gabbroic Rocks

Both oxide and sulfide minerals in the gabbroic rocks have been subject to alteration. The oxides have exsolved and altered mainly in their primary igneous crystallization positions. In contrast, the textures of sulfides are typically secondary, implying that if primary sulfides were present, they have been remobilized and concentrated in altered zones.

Oxides

The major oxides include ilmenite and magnetite, the characteristics of which are presented in Table 9. Although the oxides are mainly in their primary igneous crystallization positions, they show characteristics of alteration in the form of a number of stages of exsolution. The most abundant types are lattice and sandwich exsolution producing composite grains of ilmenite and magnetite (Fig. 20A). Lower temperature mottled types of exsolution are also common with a probable titanite, hematite, and pseudobrookite association. Titanite is especially common in zones of more intense alteration and where macroscopic veins cross oxide-rich areas. The dominant interstitial shape of the oxide mineral is commonly preserved, but extreme alteration tends to produce crystals with more blocky shapes that do not have such a distinct interstitial texture. Shearing produces rounded grains of mag-

Table 9. Typical characteristics of the main oxides and sulfides.

Mineral	Characteristics
Oxide minerals	
Magnetite and ilmenite	Magnetite is isotropic and typically has a pitted surface, whereas ilmenite is anisotropic and has a smooth surface. Commonly they occur together exhibiting lattice and sandwich exsolution. The oxide surfaces may be mottled, showing further alteration to rutile, hematite, sphene, and pseudobrookite?
Sphene	Colorless in plane polarized light, with high relief. Has low reflectance in reflected light, exhibits a good polish, and may be associated with ilmenite in veins or altered areas.
Iddingsite	Bright reddish-brown and occurs as replacement of olivine, forming amorphous or lamellar growths characterized by bright red internal reflections.
Sulfide minerals	
Pyrite	Creamy yellow, with fairly high relief and is isotropic except in shear zones, where it has wavy extinction. It may have a pitted surface, giving it a spongy appearance. Commonly forms semi-rounded grains, but may be irregular.
Chalcopyrite	Deep yellow with lower relief than pyrite and is anisotropic. Exhibits smooth surfaces and forms sub-angular laths. Rarely altered to hematite, which rims the chalcopyrite.
Sphalerite	Euhedral, hexagonal, zoned green, brown, honey yellow in plane light, or more commonly is opaque with red internal reflections. It is pale blue in reflected light and is anisotropic. Associated with pyrite and chalcopyrite. May have crystallized as wurtzite.
Pyrrhotite	Brown yellow, anisotropic and occurs as laths. Commonly associated with pyrite and chalcopyrite.
Pentlandite	Very pale yellow and anisotropic. Occurs as flames within pyrrhotite and as alteration product of olivine.
Marcasite	Common alteration product of pyrite, exhibiting semi-rounded grains with irregular edges. Typically contains relict cores of pyrite. It is anisotropic, with mottled extinction, has lower relief than pyrite, and is slightly darker yellow.

netite (Fig. 20B). Where alteration and shearing is intense, a network of ilmenite laths remains after magnetite has been etched or dissolved and redistributed within the shear zone (Fig. 20B). Magnetite occurs as an alteration product after olivine and pyroxene (Fig. 20A) where it commonly forms small laths enclosed within amphibole, and which may be aligned with former cleavage directions of replaced pyroxene. The magnetite is commonly arranged in sworls between needles of fibrous amphibole. The magnetite is mobile during alteration and forms concentrated bands along grain boundaries. In some samples secondary magnetite is associated with secondary pyrite.

Sulfide Minerals

Sulfide minerals are mainly secondary and are concentrated in altered patches, after olivine and pyroxene, and in veins, rarely, they are included in oxide minerals, indicating that they replace primary sulfides (Fig. 20C). The sulfide minerals rarely make up 2% of the rock and are commonly less than 0.5%. The maximum size is 2 mm, but they are almost always less than 1 mm in diameter. Sulfide assemblages consist of pyrite, chalcopyrite, sphalerite, marcasite, and pyrrhotite with rare pentlandite, which commonly occur either in clusters separated by silicate phases or as composite grains. Sulfide mineral characteristics are summarized in Table 9.

Pyrrhotite is rare, pyrite is ubiquitous, and marcasite occurs in more altered areas. Pyrrhotite is observed altering to pyrite, which in turn may be partially or wholly altered to marcasite (Fig. 20C).

In altered pyroxene, pyrite is present as elongate laths or irregular patches parallel to cleavage and may line the surface of the cleavage planes or form a net texture filling cleavage planes and fractures crosscutting the cleavage. Pyrite occurs both in pervasively altered zones and in veins. Marcasite is only present in the vicinity of the dikes, where the gabbroic rocks are more altered.

Chalcopyrite commonly forms inclusions in plagioclase or infills cracks across it. In highly altered areas, chalcopyrite is rimmed by hematite. Secondary pentlandite forms flames in pyrrhotite in olivine-rich samples, especially in and around partially altered olivine. Flames of chalcopyrite and pentlandite may occur together in the same pyrrhotite crystal.

Although sphalerite occurs in zones of pervasive alteration, it is most commonly associated with veins of prehnite, where it has a characteristic euhedral (Fig. 20D) hexagonal morphology, and in more altered zones near dikes. This may indicate that sphalerite forms a pseudomorph after wurtzite.

Alteration of Basaltic Rocks

The background alteration of basaltic material recovered from Site 894 is variable and heterogeneous, ranging from 10% to 85% replacement of primary minerals by secondary phases (Table 8). The most intense alteration is associated with chilled margins bounding gabbroic rocks and adjacent to vein networks. Plagioclase, both as phenocrysts and groundmass, is typically fresh or locally altered to clay along microfractures or in the vicinity of veins. Plagioclase glomerocrysts are variably altered on a thin-section scale, ranging from 5% to 90%, and are commonly replaced by patches and anastomosing microveinlets of secondary plagioclase, very fine-grained clay, and smectite. Discontinuous microveinlets of prehnite are rare, as are rounded pods (0.7 mm in diameter) of smectite. Rare liquid- to vapor-dominated fluid inclusions that may be primary are locally present in secondary plagioclase. Primary devitrified glass inclusions that mimic plagioclase grain boundaries commonly contain small vapor bubbles. Fine-grained aggregates of green-brown smectite, chlorite, mesh serpentine?, and fine-grained magnetite and trace pyrite variably replace or pseudomorph groundmass and olivine phenocrysts. Relict olivine is locally preserved. Clinopyroxene phenocrysts and groundmass phases are variably altered to pale green fibrous actinolite, trace chlorite, and fine-grained opaques. Alteration of groundmass minerals and mesostasis is heterogeneous, with common replacement by very fine-grained amphibole?, zeolite, and smectite.

The oxide minerals are only moderately altered, although many titanomagnetite crystals exhibit partial oxidative alteration to titanomaghemite along cracks. In contrast, the sulfide minerals are almost entirely altered. The most abundant sulfide in the basaltic rocks is pyrite, which is concentrated in altered zones. Minor chalcopyrite is also present. Sulfides, especially pyrite, are concentrated in altered phenocrysts where they form a net texture. In basaltic chilled margins, however, the phenocrysts are devoid of sulfides, indicating that the alteration associated with introduction of the sulfides did not affect these phases.

Veins and Associated Alteration

Macroscopic veins were observed during core description. Data on the location, mineralogy, and morphology of veins and associated wall-rock alteration were recorded in the vein spreadsheet (Appendix C on CD-ROM; see Fig. 12 of "Explanatory Notes" chapter for example). All measurements were made on the archive halves of the core

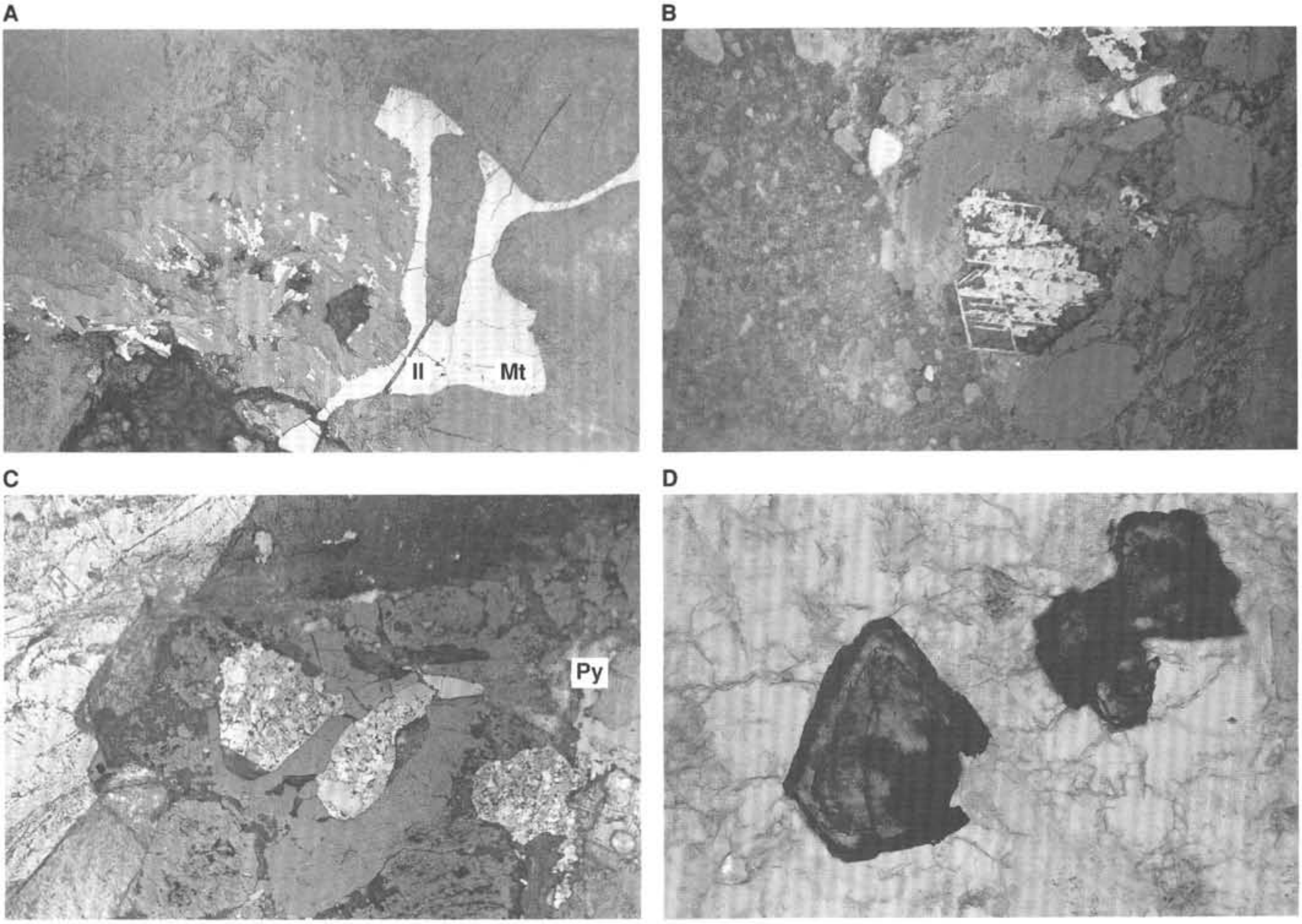

Figure 20. **A.** Interstitial oxide (pale gray) in silicate showing characteristic interstitial texture that completely surrounds silicate minerals. This oxide contains magnetite (Mt; pitted surface) and ilmenite (Il; thick "sandwich" lath surrounding the silicate). It is located adjacent to an alteration area (left) that hosts much finer grained secondary magnetite after pyroxene (Sample 147-894G-2R-3, 118–120 cm; field of view is 1.5 mm; reflected light). **B.** Lattice exsolution laths of ilmenite remaining as a box work texture after dissolution of magnetite in a shear zone in gabbro. Note the sub-rounded grain of magnetite in the shear zone (Sample 147-894F-2R-1, 54–56 cm; field of view is 0.8 mm; reflected light). **C.** Rounded patches of marcasite (mottled gray, center) almost completely surrounded by oxide (dark gray smooth), which in turn is surrounded by silicate (dark gray and pale gray right). Marcasite shows characteristic mottled extinction due to intergrowth of differently oriented laths that make up the grain. This contrasts with the even reflection from the nearby pyrite (Py, gray) (Sample 147-894F-2R-1, 32–35 cm; field of view is 1.5 mm; reflected partially crossed polarized light). **D.** Zoned euhedral sphalerite showing hexagonal form in secondary vein (Sample 147-894G-2R-3, 11–14 cm; field of view is 0.8 mm; plane polarized light).

and selected samples were taken from the working halves for shipboard petrography. Identification of fine-grained vein fillings at Site 894 was facilitated by shipboard X-ray diffraction studies on material scraped from representative veins. Smectite and mixed-layer clays were identified by comparing diffraction patterns of air-dried and ethylene glycol-solvated preparations. Below, we discuss veins in the gabbroic and basaltic lithologies of Site 894.

Veins in Gabbroic Rocks

Both macroscopic (≥0.01 mm wide) and microscopic veins occur in the gabbroic lithologies of Site 894. Petrographic study revealed that the earliest veins are related to the pervasive static metamorphism and are microscopic. All macroscopic veins crosscut and therefore postdate the microscopic veins.

Microscopic Veins

The early amphibolite facies mineral assemblages are not associated with macroscopic brittle or ductile deformation. However, optical microscopy reveals a dense network of irregular microscopic veins that includes micron-size amphibole grains along grain boundaries between relict igneous minerals, dense arrays of fluid inclusions along healed microfractures, and microveins that are tens of microns wide and that cut igneous minerals. These veins are ubiquitous throughout the gabbroic lithologies at Site 894 and appear to represent the conduits that allowed influx of aqueous solutions and resultant hydration of the primary minerals to the static amphibolite facies mineral assemblages.

Macroscopic Veins

Macroscopic veins postdate the early alteration and associated microveins. The macroscopic veins can be divided into three types based on vein-filling mineral assemblages (Table 10). The earliest veins are filled primarily by green amphibole, with rare pale brown amphibole, chlorite, and titanite. In some samples of this vein type, the vein-filling minerals change as a function of the magmatic mineral being cut. These veins are green and are typically difficult to distin-

Table 10. Summary of vein types in gabbroic rocks from Site 894.

Type	Major minerals	Width	Comments
Dark green	Amphibole	1 micron to tens of microns	Microscopic. Associated with static amphibolite facies mineral assemblages. Not related to macroscopic deformation features.
Dark to medium green	Green amphibole ± brown amphibole ± chlorite ± sphene	<0.01 mm to several mm	Macroscopic. Fracture-filling. Varying mineralogies and widths along veins.
Various shades of green	Chlorite ± prehnite ± green amphibole ± epidote ± smectite	0.1 mm to several mm	Macroscopic. Commonly form composite veins. Associated with strong wall-rock alteration, local brecciation and cataclasis.
Light green to yellow-brown to white	Chlorite + smectite ± mixed-layer clays ± zeolites ± calcite	0.1 mm to several mm	Macroscopic. Variable wall-rock alteration.

guish from the background alteration. Their morphologies range from distinct, sharp-sided features with centimeters of continuity to irregular wispy discontinuous structures. Macroscopic widths are variable, ranging from <0.01 mm to several millimeters. In thin section, widths can be seen to vary along the vein as a function of the mineral being cut. For example, Figure 21A shows an example of two crosscutting green amphibole veins: where the veins cut plagioclase grains, they are narrower than where the host mineral is clinopyroxene. Similar observations have been made for the earliest veins in gabbroic rocks in the Skaergaard Intrusion (Bird et al., 1986, 1988; Manning and Bird, 1986).

Fractures filled by chlorite ± smectite ± prehnite ± actinolite ± epidote postdate the amphibole veins. These later veins exhibit a wide range in mineral fill, but invariably contain green to dark green chlorite. Most examples are zoned such that chlorite ± actinolite line vein margins, and discontinuous elliptical patches of prehnite ± smectite ± epidote fill vein centers. These veins are typically associated with strong wall-rock alteration to secondary plagioclase, actinolite, chlorite, sphene, and local epidote and prehnite (Fig. 22). In several samples, wall-rock alteration extends for >10 cm at high angles from the vein orientation in diffuse anastomosing zones dominated by prehnite and albite alteration of magmatic plagioclase (Fig. 23). The veins are 0.1 to several mm wide and typically have true dips of 40°–60°. Figure 21B is a dark green chlorite + prehnite vein in Sample 147-894G-12R-2 (Piece 4F), which shows that widths of these veins are independent of host rock mineralogy and crosscut the early alteration. Abundant microveins of prehnite and/or chlorite are common in the wall rock near the principal vein. The characteristic alteration of primary plagioclase to a more sodic secondary plagioclase is illustrated in Figure 21C. These veins and associated wall-rock alteration also occur near rare zones of cataclastic deformation where they may be vuggy (Fig. 24).

The youngest veins are filled by combinations of chlorite, smectite, mixed-layer clays, calcite, and minor zeolite. They range in color from light green to brown, brownish yellow, and grayish white. X-ray diffraction analyses suggest that a spectrum of layered silicates ranging from chlorite to smectite is found in these veins. Veins of this type exhibit a range of dips, with many subvertical examples. Minerals of this vein type are commonly observed as coatings on core pieces, suggesting that the pieces broke along these veins during drilling and entrainment in the core barrel. The mineral assemblage associated with this vein type also occurs as late residual pore filling in earlier vein types. These latest veins have a range in width that is similar to that of the other vein types. The veins are associated with variable wall-rock alteration of relict igneous minerals and earlier metamorphic minerals to the same minerals as those in the veins.

X-ray diffraction studies were performed on the chlorite-bearing veins to better characterize the mineralogy of the fine-grained phyllosilicates. Results indicate that the early dark green chlorite veins and the later chlorite + clay veins are filled by phyllosilicates with contrasting mineralogy and structure. Chlorite from the intermediate vein type described above has well-defined basal reflections (e.g., Fig. 25A, -B), with d-spacings of (002) reflections typically between 7.09 and 7.23 Å and (003) reflections at 4.75 Å. The relatively wide peaks suggest that the chlorite is poorly crystallized. Ethylene glycol solvation produced significant changes in the diffraction patterns. Smectite was detected after glycolation by the appearance of the (001) reflection at 17 Å (e.g., Fig. 25B, -C, -D). The presence of Ca-smectite is indicated by the broad peak distribution between 27° and 30° 2θ, corresponding to the (005) reflection. Reflections also were observed for prehnite, amphibole, calcite, and minor mixed-layer smectite/illite, as well as plagioclase, which may represent wall-rock clasts in the veins. Tremolitic compositions of the amphibole are indicated by peaks with d-spacings at 8.38, 3.12, and 2.71 Å in Sample 147-894G-12R-5 (Piece 7C, 56–57 cm) (Fig. 25B).

Smectite and/or mixed-layer clays are the dominant minerals in the late veins (e.g., Fig. 25D and Fig. 26). Mixed-layer smectite/illite (denoted as M–L in Fig. 26) was identified by the appearance of reflections at approximately 17.2 Å, 8.5 Å, and 5.6 Å after glycolation. Corrensite, which is a smectite-chlorite in regularly mixed layers (R1), showed reflections at about 30 Å, 14.8 Å, 7.3 Å, 4.8 Å, and 3.5 Å (Fig. 26). After glycolation, the first and third reflections shift to 32 Å and 7.8 Å, respectively. The latter reflection corresponds to the superstructure 004*, which appears after glycolation at about 11.3° 2θ, and is characteristic for corrensite (e.g., Moore and Reynolds, 1989). Additional peaks for plagioclase, calcite, and locally, chlorite were observed in the late veins.

Veins in Basaltic Rocks

Two generations of veins are present in the basaltic rocks. The first generation is represented by veins of chlorite + actinolite that have widths ranging from 1 to 3 mm. Where they cut plagioclase, these veins contain up to 30% titanite. They commonly constitute anastomosing networks responsible for local, strong alteration of the wall rock. Thinner veins with widths ranging from 0.3 to 0.5 mm are also present, but contain only chlorite.

The later veins are always very thin (0.01–0.05 mm) to thin (0.1–0.5 mm), and most of them are filled with the association chlorite + clays (dominantly smectites). A few of the late veins contain minor iron-oxides, rare chlorite, and zeolites.

Vein Density

Vein density, or the number of veins per unit length, allows characterization of fracture-related fluid flow and associated wall-rock alteration. During core description and vein identification, individual piece lengths were measured and summed for Hole 894G at Site 894 as described in the "Igneous-metamorphic Core Description" section of the "Explanatory Notes" chapter. Vein densities were then calculated by dividing the number of veins by the cumulative piece length. A total of 770 veins were observed in Hole 894G (35.5 m of cumulative piece length; Appendix C), yielding a vein density of 0.21 cm^{-1}. The calculated densities are a minimum as fine-scale veins may be underrepresented during core description. Figure 27A shows vein densities for each curated section of the core. Observed values range widely, from 0 to 0.44 veins cm^{-1}. The vein density observed in Hole 894G is dramatically higher than the values of 0.01 and 0.06 cm^{-1} for

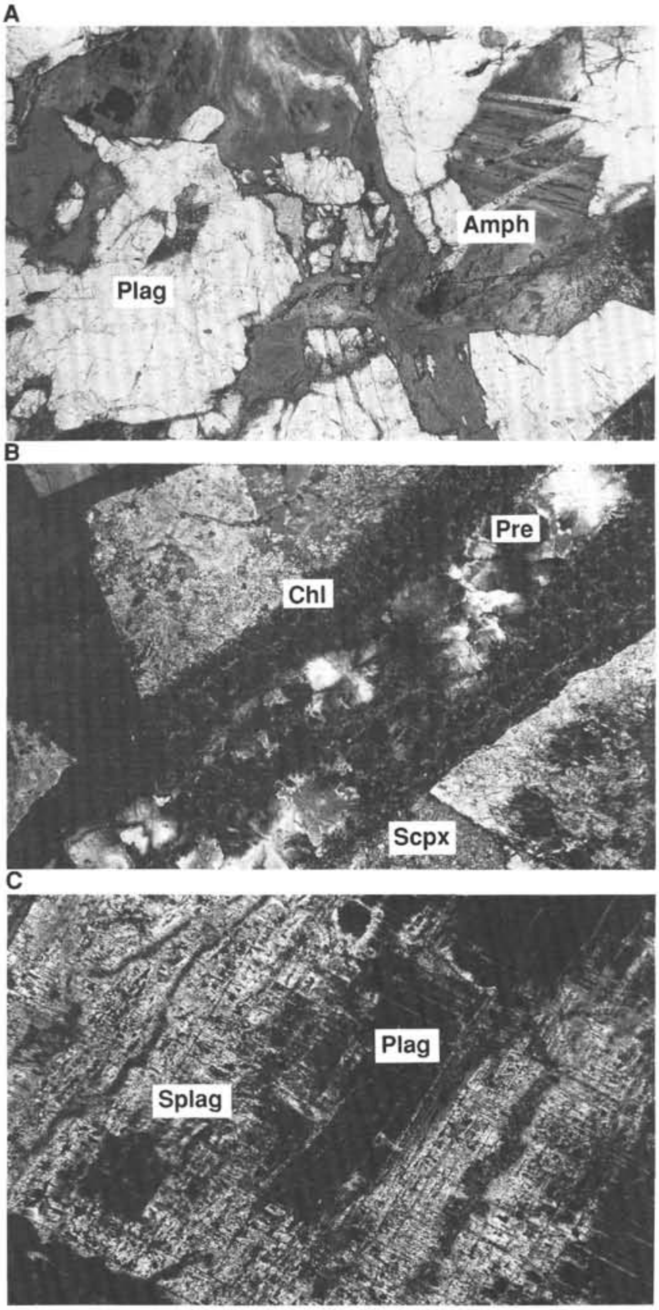

Figure 21. Photomicrographs of vein textures and relations. **A.** Crosscutting green amphibole (Amph) veins that are nearly orthogonal. The veins are thinnest where they cut primary plagioclase grains (Plag). Where the veins cut primary clinopyroxene, amphibole crystals extend into the wall rock. Note the presence of fine-grained secondary clinopyroxene (Scpx) adjacent to the relict igneous clinopyroxene (Sample 147-894F-2R-1, Piece 1, 5–7 cm; field of view is 1.5 mm; plane polarized light). **B.** Chlorite (Chl) + prehnite (Pre) vein cutting early alteration of clinopyroxene to secondary clinopyroxene and green amphibole. The formation of secondary plagioclase from primary plagioclase is localized at the vein margin. Prehnite characteristically forms in elliptical patches in the centers of veins of this type (Sample 147-894G-12R-2, Piece 4F, 56–58 cm; field of view is 1.5 mm; crossed polars). **C.** Pseudomorphic replacement of igneous plagioclase (Plag) by secondary plagioclase (Splag) in the wall rock near the chlorite + prehnite vein shown in (B). Relict plagioclase is preserved only in the core of the original grain (field of view is 1.5 mm; crossed polars).

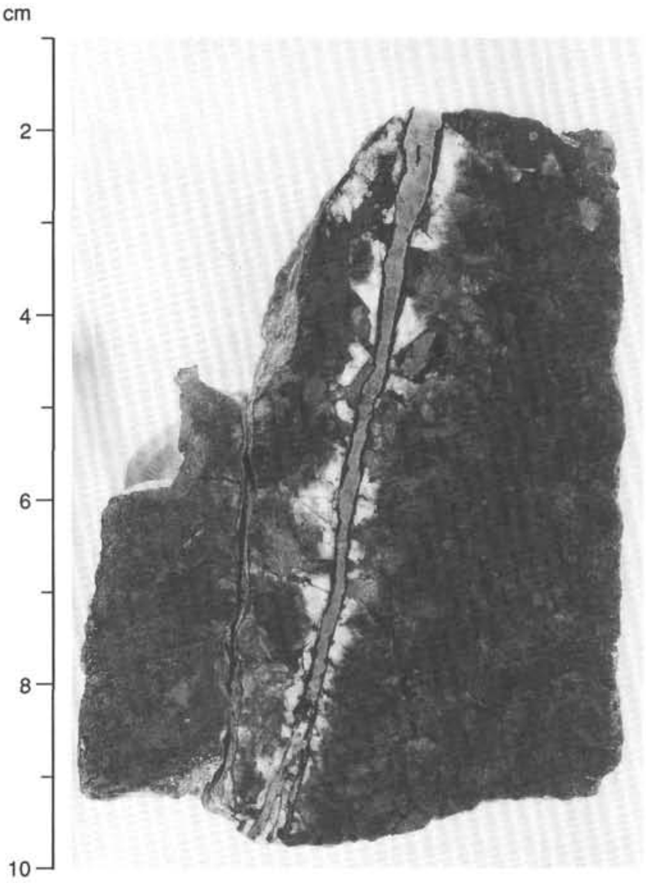

Figure 22. Photograph of alteration of plagioclase in wall rock adjacent to a chlorite + prehnite vein (Sample 147-894G-21W-1, Piece 1, 1–9 cm).

the Skaergaard and Oman gabbros, respectively (Bird et al., 1986; Nehlig and Juteau, 1988). Vein densities of the fine- and medium-grained diabases in the lower portion of Hole 504B are ~0.1 cm^{-1} (Dick, Erzinger, Stokking, et al., 1992), lower by a factor of two than those observed in the gabbroic rocks of Hole 894G.

The variation in vein abundance with depth in Hole 894G can be evaluated by calculating vein densities over large-length scales. Figure 27B shows such a calculation using 5-m intervals of cumulative piece length. Vein densities are highest in the upper 10 m, which correspond to Cores 1–8 (~0.29 cm^{-1}). Vein density decreases sharply to 0.18 cm^{-1} in the next 5 m of cumulative piece length and is ≤0.22 cm^{-1} for the rest of the gabbros.

Metamorphism Associated with Cataclastic Deformation

Highly altered intervals in the gabbroic rocks recovered at Site 894 are associated with local brittle deformation and shearing under greenschist to zeolite facies conditions and are generally distinguished from the more pervasive higher temperature static metamorphism by a higher degree of plagioclase alteration. As described in the "Structure" section, this chapter, cataclastic deformation as the result of faulting ranges from protocataclasis through cataclasis to ultracataclasis in thin shear zones. Although veining and microfracturing is by far the most dominant brittle deformation feature at this site, distinct zones of cataclastic deformation and shearing occur in the shallow Holes 894C, 894E, and 894F, and locally at similar shallow levels (above approximately 38 mbsf) in Core 2R of Hole 894G. At greater depths in Hole 894G, brecciation and cataclastic deformation is rare and tends to be restricted to intervals of dense

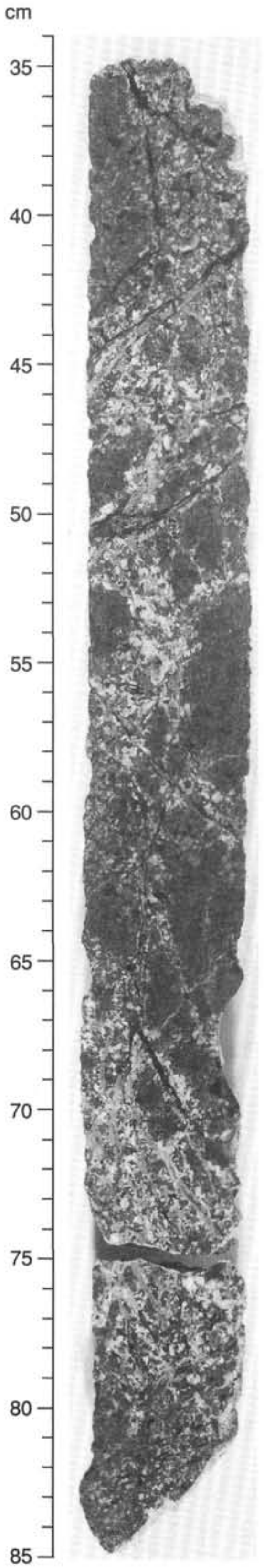

Figure 23. Complex wall rock alteration near chlorite + prehnite veins (Sample 147-894G-8R1-1, 34–85 cm).

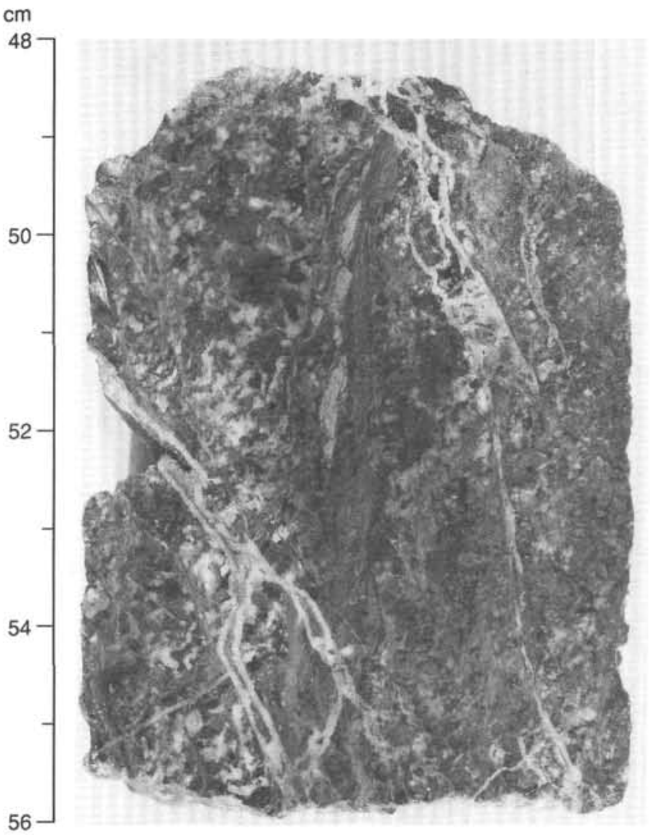

Figure 24. Vuggy anastomosing chlorite + prehnite veins crosscutting a cataclastic shear zone (Sample 147-894G-2R-3, 48–56 cm).

prehnite-veining with pervasive alteration of plagioclase (e.g., Sections 147-894G-8R-1, 147-894G-11R-1 through -21R-6, and Fig. 28).

Varying degrees and scales of cataclastic deformation and extent of alteration are characteristic of the upper 30–40 m of gabbroic section at Site 894. Examples of cataclastic fabrics are shown in Figures 24, 28, and 29 (see also "Structure" section, this chapter). In Hole 894F, highly to very highly altered (75%–95%) cataclastic intervals vary in thickness from approximately 2 mm to 5 cm and are locally cut by a series of 1- to 2-cm-wide ultracataclastic shear zones (see Figs. 30 and 31). The cataclastic zones are characterized by grain-size reduction of the primary igneous phases, typically resulting in subrounded to angular porphyroclasts of altered plagioclase, pyroxene, amphibole, and/or compound gabbroic clasts in a fine-grained, clay-rich matrix (see Fig. 32). The sheared intervals are cut by 0.5- to 5-mm-wide veins, typically filled by prehnite + chlorite ± actinolitic amphibole, with younger generations filled by zeolites ± mixed-layer clays (see also "Structure" section, this chapter).

X-ray diffraction determinations were carried out on the characteristic deformation zones in Hole 894F, as optical mineral identification in the cataclastic matrix and the ultraclastic shear zones is commonly difficult because of the very fine grain size and high degree of alteration. The results of the XRD analyses show that the cataclastically deformed intervals consist of chlorite, tremolitic amphibole, sodic plagioclase, and diopsidic clinopyroxene, with varying occurrences of prehnite and mixed-layer chlorite/smectite. The chlorite is poorly crystallized, as indicated by relatively wide peaks at 14.2 Å, 7.1 Å, and 4.75 Å, and commonly shows expansion of the (001) reflection with ethylene glycol treatment. Mixed-layer chlorite/smectite, predominantly corrensite, was identified by first, second, and fourth order reflections at about 29 Å, 14.5 Å, and 7.2 Å. After glycolation these

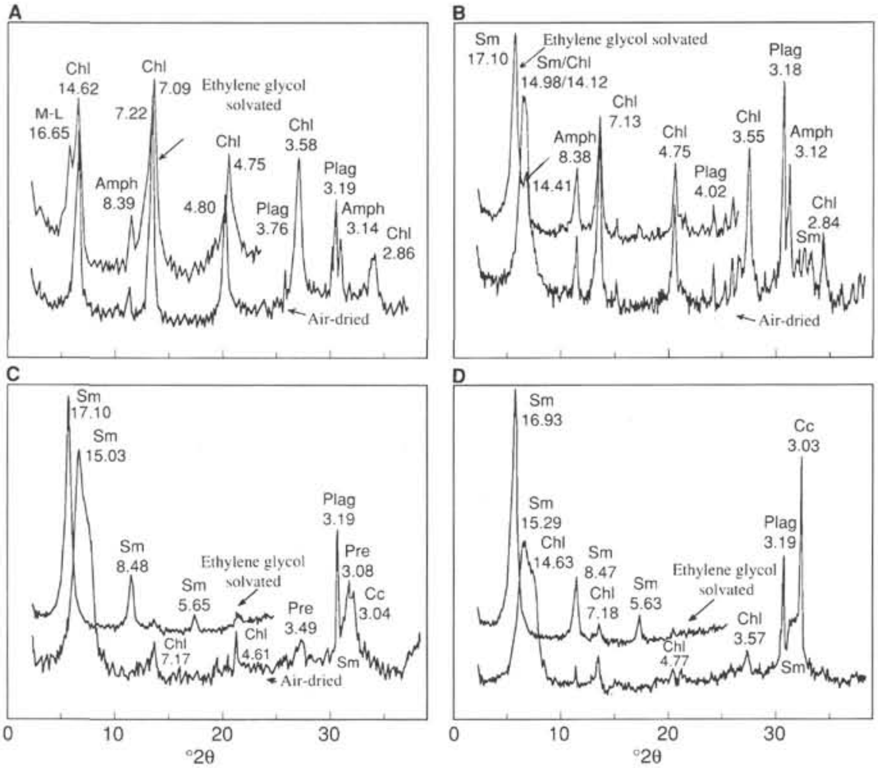

Figure 25. X-ray diffractograms showing peak positions and d-spacing (Å) for air-dried and ethylene glycol-solvated vein material from composite chlorite ± amphibole ± prehnite ± smectite veins (A, B, and C) and from late smectite and chlorite veins (D). Chl = chlorite; Amph = amphibole; Sm = smectite; Plag = plagioclase; M-L = mixed layers; Pre = prehnite; Cc = smectite/illite. **A.** Sample 147-894G-13R-3 (Piece 5V2, 60–61 cm). **B.** Sample 147-894G-12R-5 (Piece 7C, 56–57 cm). **C.** Sample 147-894G-12R-3 (Piece 1F2, 24–26 cm). **D.** Sample 147-894G-4R-2 (Piece 8, 44–47 cm).

peaks shifted to about 32 Å, 15.8 Å, and 7.8 Å (Fig. 33A). The very fine ultracataclasite intervals are predominantly made up of chlorite, corrensite, and sodic plagioclase (Fig. 33B). X-ray diffraction determination of the youngest veins in this section indicates that the zeolites are predominantly analcime and wairakite.

Cataclastic deformation, veining, and extensive alteration are particularly well developed in the olivine gabbros located below a basaltic unit in Section 147-894G-2R-1. Section 147-894G-2R-3 is characterized by a transition from locally fractured or brecciated to more pervasive cataclastic deformation with complex multiple generations of veins. Section 147-894G-2R-3 (Pieces 1 through 3) is approximately 70%–75% altered and makes up a sulfide-rich interval, defined by interdispersed secondary pyrite, sphalerite, and minor chalcopyrite, with strong fracturing and brecciation associated with prehnite vein formation (Fig. 29). A narrow, nearly vertical cataclastic shear zone with a thin (5- to 10-mm-wide) light green ultracataclasite band can be traced from 20 to 100 cm in the very highly altered (to 90% total alteration) olivine gabbros in Section 147-894G-2R-3 (Pieces 5 through 12). Cataclastic deformation has locally produced boudinaged, faulted, and completely altered porphyroclasts of plagioclase. The cataclastic shear zone and ultracataclasite band are cut by subparallel, vuggy prehnite veins, which in turn are cut by zeolite ± clay veins (e.g., Fig. 24). Secondary sulfides include pyrite in the shear zones and minor sphalerite in prehnite veins. Below 100 cm of Section 147-894G-2R-3, the olivine gabbros are relatively undeformed and only moderately altered (approximately 35% total alteration).

Microscopically, the cataclastic deformation zones at Site 894 are characterized by very heterogeneous grain sizes, degree of clinopyroxene replacement, and extent of cataclasis (see Figs. 32 and 34). Igneous plagioclase is highly to completely altered to secondary plagioclase and clay, giving a characteristic dusty appearance. At contacts to altered clinopyroxene grains, they are overgrown with needles of green amphibole. Fractured, bent, and faulted grains are common, with extensive subgrain development, depending on degree of deformation. Fractures in plagioclase are filled with clear secondary plagioclase, or less commonly with chlorite or clay. Extinction is generally undulating or blocky. Primary clinopyroxene is generally 75%–85% altered to green-blue to green amphibole, locally associated with Fe-oxides of variable, but commonly submicron grain-size, and secondary clinopyroxene. In less sheared areas, amphibole replacement of clinopyroxene is clearly static and commonly forms clusters of radiating fibrous grains. Rare clasts of prehnite are also present in matrix-dominated zones. Towards the shear zones, clay content increases, and altered plagioclase and clinopyroxene increasingly form blocky fine- to very fine-grained clasts in the cataclasite matrix. Foliation in these rocks is defined by the alignment of clasts and alternating cataclasite and ultracataclasite layers.

Fluid Inclusions

Multiple populations of fluid inclusions in the variably altered and deformed gabbroic and basalt samples indicate that fluid circulation at Site 894 involved fluids of widely varying composition and temperature, starting at late magmatic conditions. Inclusions are most abundant in gabbroic and basaltic matrix minerals, where they occur along anastomosing arrays of healed microfractures, and are less common as primary inclusions trapped during growth of primary and secondary minerals. In vein minerals, primary and secondary inclusions are rare, probably reflecting the inherent difficulty of the vein minerals such as actinolite, chlorite, and prehnite to trap inclusions.

Table 11. Fluid inclusion types in gabbroic and basaltic rocks from Site 894.

Inclusion type	Mineral host		Origin		Comments
Type 1: Liquid-dominated, daughter mineral absent	1a	Plagioclase		Secondary	
	1b	Plagioclase	Primary		
	1c	Plagioclase	Primary	Secondary	$+CO_2$?
	1a	Apatite	Primary	Secondary	$+CO_2$?
	1c	Apatite	Primary	Secondary	$+CO_2$?
	1a	Zircon		Secondary	
	1a	Epidote	Primary	Secondary	
	1a	Amphibole	Primary		
	1a	Secondary Clinopyroxene	Primary		
Type 2: Vapor-dominated daughter mineral absent	2	Plagioclase[a]	Primary		$\pm CO_2$?
	2	Apatite[a]	Primary	Secondary	$\pm CO_2$?
	2	Secondary Clinopyroxene	Primary		
Type 3: Daughter mineral-bearing inclusions	3a	Plagioclase		Secondary	3-4 daughter, CH_4?
	3b	Plagioclase[a]	Primary	Secondary	Halite daughters
	3a	Apatite[a]	Primary	Secondary	Halite daughters

[a] Vapor-dominated and halite-bearing fluid inclusions are cogenetic.

Based on petrographic analyses at room temperature, the inclusions were classified into three main types (Table 11).

Type 1: Liquid-dominated, Daughter Mineral-absent Inclusions

Type 1 inclusions are liquid-dominated inclusions, which are pervasive in primary and secondary plagioclase and less common in apatite, zircon, epidote, and secondary amphibole and clinopyroxene. Inclusion sizes are widely variable, ranging from <1 µm to 35 µm. The liquid-dominated inclusions occur as three subtypes (Table 11). Type 1a inclusions (Fig. 35A) are hosted in plagioclase, amphibole, secondary clinopyroxene, apatite, and zircon; exhibit negative to subhedral crystal habits; contain a small aqueous liquid-rimmed vapor bubble (<50 vol%); and commonly form anastomosing cross-cutting arrays along healed microfractures. These inclusions are secondary in origin. Type 1b inclusions form concentrated zones of irregularly shaped, ragged inclusions and occur in highly altered patches of plagioclase. These inclusions may be primary in origin, although textural evidence for primary origin is not conclusive. Type 1c inclusions, which are plagioclase and apatite-hosted, occur parallel to crystal faces and were trapped during mineral growth, or less commonly occur as anastomosing arrays along healed microfractures. These inclusions contain a vapor bubble making up less than ≈10%–15% volume of the inclusions; such inclusion bubbles commonly exhibit "brownian motion." These inclusions may be CO_2-dominated.

Type 2: Vapor-dominated, Daughter Mineral-absent Inclusions

Vapor-dominated inclusions only occur in gabbro samples, where they are rare to moderately abundant as primary and secondary inclusions in apatite, and as primary inclusions in secondary plagioclase and clinopyroxene. In apatite and secondary plagioclase, vapor-dominated inclusions are spatially associated with halite-bearing inclusions. In apatite, individual inclusion arrays may contain solely vapor-dominated inclusions; however, some arrays contain both vapor-dominated and liquid-dominated, halite-bearing inclusions. In secondary clinopyroxene, subhedral vapor-dominated inclusions are extremely abundant and commonly exhibit variable vapor to liquid ratios.

Type 3: Daughter Mineral-bearing Inclusions

Daughter mineral-bearing inclusions occur as two types in the gabbro samples. Type 3a inclusions are only hosted in plagioclase, where they are secondary in origin and are liquid-dominated to vapor-rich. Daughter mineral phases are extremely abundant and include fibrous and elongate highly birefringent crystals (amphibole?), cubic birefringent daughter minerals, and rare opaques. Type 3b inclusions are primary and secondary halite-bearing inclusions hosted in apatite and plagioclase (Fig. 35B). Fine-grained opaques are commonly included in the halite.

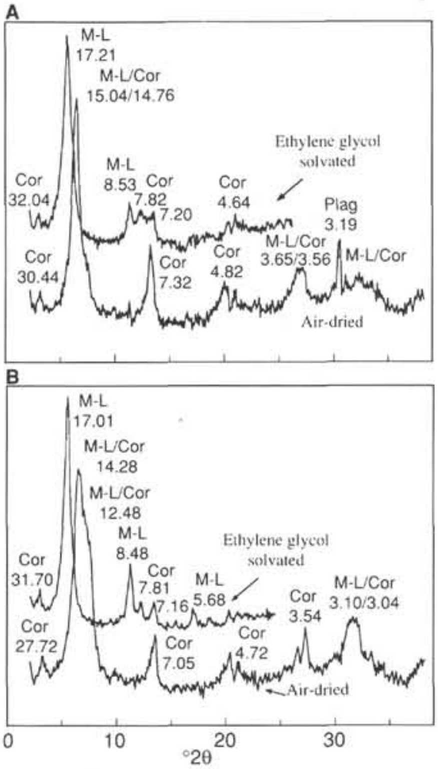

Figure 26. X-ray diffractograms showing peak positions and d-spacing (Å) for air-dried and ethylene glycol-solvated vein material from late mixed-layer clay veins. Abbreviations are the same as used in Figure 25; Cor = corrensite (a mixed-layer chlorite/smectite). **A.** Sample 147-894G-7R-2 (Piece 4, 37–39 cm). **B.** Sample 147-894G-12R-3 (Piece 1F, 24–26).

Discussion

The plutonic and shallow crustal suite of rocks recovered from Site 894 is the product of a complex history involving the integrated effects of magmatic, tectonic, and hydrothermal processes acting in a fast-spreading environment. The earliest hydrothermal event recorded in the plutonic suite involved exsolution of magmatic volatiles rich in CO_2(?) and $H_2O + NaCl \pm CO_2$ from residual evolved pockets

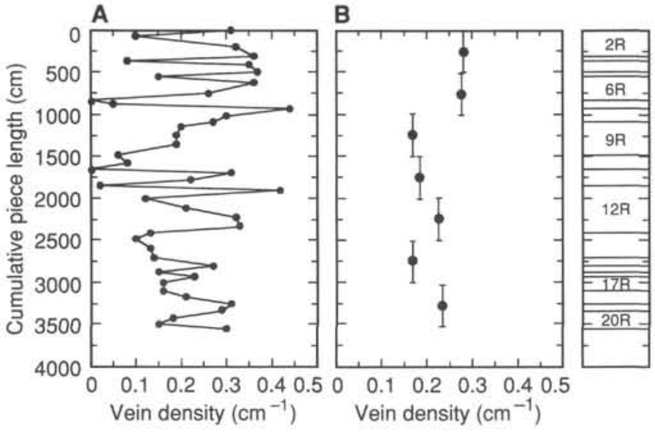

Figure 27. Variation in vein densities with the cumulative piece length. **A.** Vein density in each curated section of core recovered from Hole 894G. **B.** Vein densities calculated over 5-m intervals downhole. The filled circles are plotted at the midpoints of the interval, and the bars denote the depth range over which each vein density applies.

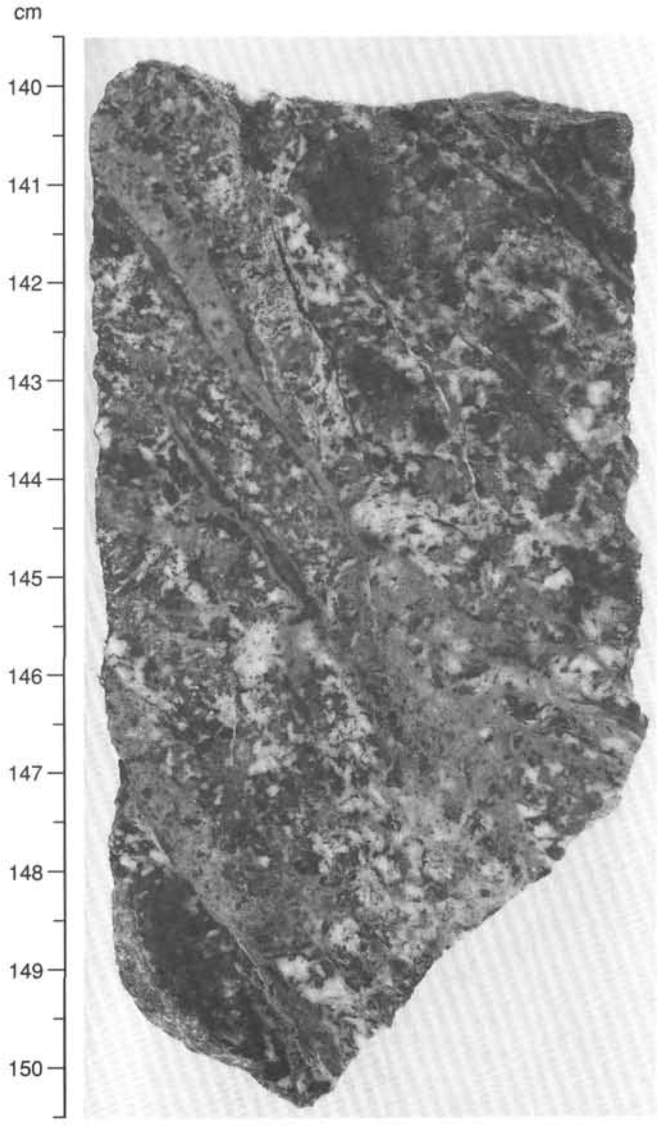

Figure 28. Formation of subparallel cataclastic zones and extensive wall-rock alteration to secondary plagioclase, actinolite, mixed-layer clays ± chlorite associated with dense network of prehnite veins (Sample 147-894G-8R-1, Piece 11, 140–150 cm).

of melt, as evidenced by primary apatite-hosted fluid inclusions in coarse-grained patches and oxide-rich zones. Such inclusions are not unique to the EPR, as similar apatite-hosted inclusions have been observed in gabbros from the Kane Fracture Zone (MARK) and Hole 735B on the Southwest Indian Ridge (Kelley, unpubl. data). Homogenization behavior of the MARK inclusions indicates that the magmatically derived fluids were entrapped at temperatures in excess of 700°C (Kelley et al., in press; Kelley and Delaney, 1987). In gabbroic rocks from Hess Deep, well-developed, coarse-grained amphibole within the coarse-grained patches may reflect deuteric alteration by these early fluids; however, their origin is not yet well constrained.

The onset of pervasive fluid penetration into the gabbros is marked by the occurrence of early amphibolite facies mineral assemblages replacing the primary igneous minerals. Flow of fluids into the plutonic suite was facilitated initially by microscopic isolated to anastomosing fractures and flow along grain boundaries. These fossilized flow channels are recorded by very fine veinlets of amphibole, and amphibole rimming grain boundaries of some minerals. Vein density, and static background alteration associated with these fine-scale brittle fracturing events is heterogeneous, and may be correlated to grain size of the host rock (e.g., finer grained samples are less densely veined and are, therefore, less altered than coarser grained samples). Alteration associated with this background static metamorphism is heterogeneous and commonly reflects rock-dominated conditions. The variable and diverse nature of the mineralogical zonations replacing olivines probably reflects incomplete alteration under such conditions, where secondary mineral formation was governed by local variations in water to rock ratios, temperature, and kinetic effects. Similarly, vein-filling mineralogy along these microfractures is commonly governed by the magmatic mineral being cut. The presence of amphibole filling these crack networks, and associated metamorphism of the host rock, suggest migration of seawater through the gabbros at temperatures in excess of 500°C. The temperatures recorded by the early mineral assemblages are sufficiently high that they are probably related to the cooling and contraction of the gabbros as they moved off the EPR axis.

Pervasive development of macroscopic fractures at lower temperatures enhanced fluid circulation in the gabbros, and led to the development of actinolite, chlorite + prehnite, and chlorite/smectite ± zeolite veins, which postdate the early amphibolite facies mineral assemblages. The mineralogy of these later veins is less dependent on the host rock mineralogy, and alteration haloes are more common, suggesting larger deviations from chemical equilibrium during this stage of alteration. Liquid to vapor ratios of secondary, liquid-dominated inclusions in plagioclase, apatite, and epidote associated with this later stage of alteration suggest homogenization temperatures of 200°–400°C.

Fluid rock interaction was most intense in local cataclastic zones, where deformation associated with shearing enhanced penetration of evolved Ca-rich fluids and gabbroic host rocks were pervasively recrystallized at greenschist to zeolite facies. Undeformed prehnite veins that crosscut some cataclastic zones indicate that, locally, the migration of Ca-rich fluids postdated deformation. Formation of the cataclasites to ultracataclasites may reflect deformation and attendant uplift of the gabbroic crustal rocks in response to development of the Cocos-Nazca propagating rift. The extremely high densities of the late chlorite ± prehnite and chlorite/smectite ± zeolite veins found in gabbros at Hole 894G, which are about two times greater than those observed in the lower sheeted dikes from Hole 504B, may reflect the unique and complicated tectonic history associated with the intersection of the Cocos-Nazca propagating rift and subsequent uplift and exposure of the gabbros.

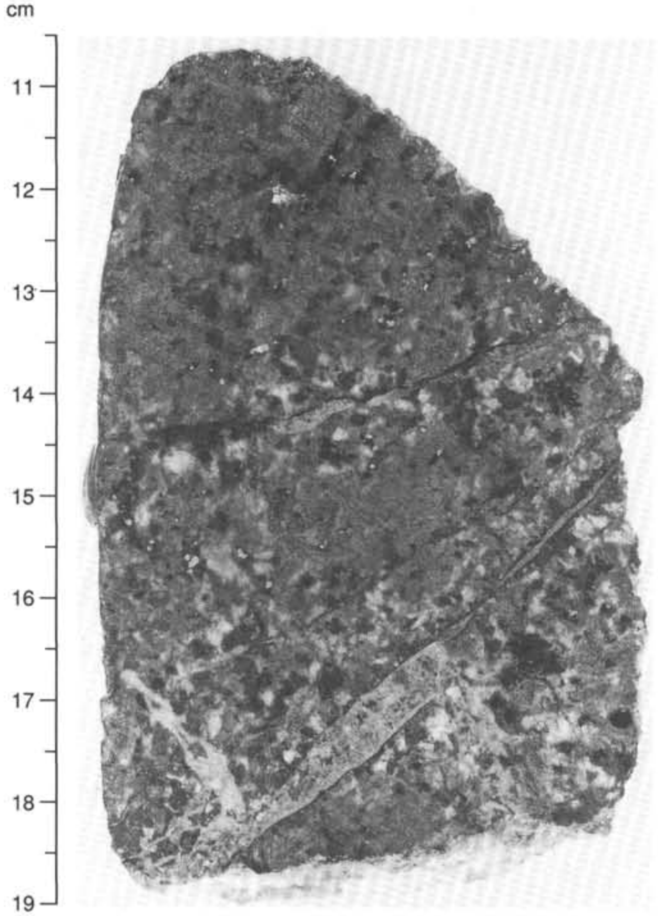

Figure 29. Incipient cataclasis and local brecciation associated with prehnite vein formation (Sample 147-894G-2R-3, Piece 3, 10–19 cm).

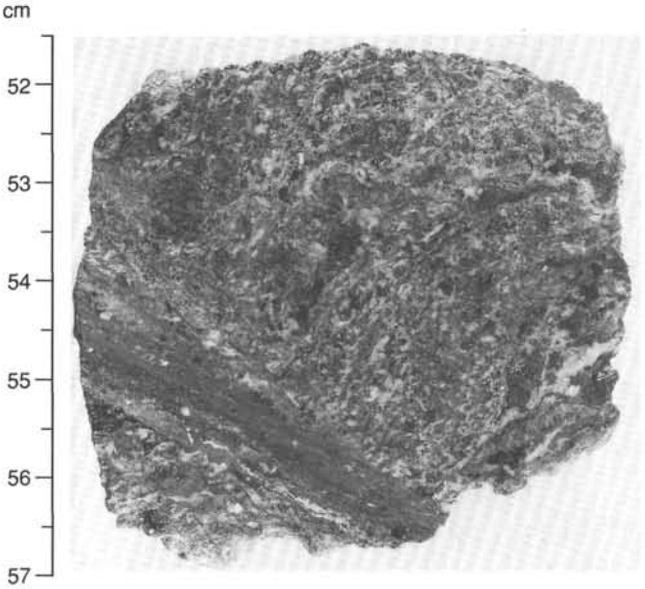

Figure 30. Ultracataclastic shear zone. Note rotation of the foliation into shear zone. Shear sense: top down (Sample 147-894F-2R-1, Piece 7, 51–57 cm).

STRUCTURE

Introduction

The gabbroic rocks collected from Site 894 are either isotropic or foliated, but are devoid of igneous layering. The foliated gabbros have a penetrative fabric defined by the shape-preferred orientation of crystals which, we will argue, is related to magmatic flow. The rocks show little evidence for solid-state penetrative deformation, in marked contrast to gabbros from Hole 735B (Leg 118), the only other ODP or DSDP hole to date that drilled a substantial section of oceanic Layer 3.

Displacive structures at Site 894 are found in the form of a few cataclastic and ultracataclastic shear bands located at shallow levels (0.05–22.54 mbsf) in Holes 894C, 894F, and 894G. Breccia networks are restricted to several horizons (Section 147-894G-11R-1, 84 mbsf; Section 147-894G-12R-1, 94 mbsf; Section 147-894G-20R-3, 147 mbsf). No mylonitic shear zones were recognized.

Site 894 is instead dominated by abundant veining throughout the entire section. Some 448 veins were measured from the 47.58 m of core recovered from Holes 894F and 894G. Secondary minerals fill tensile fractures and in rare instances accommodate minor displacement; few open fractures were recognized (27 identified). The veining is distributed throughout the section, as discussed in the "Metamorphism" section, this chapter.

Penetrative Fabrics

The fabric in the gabbros is marked only by the preferred shape orientation of euhedral, 1–3 mm plagioclase crystals (Fig. 36), and is often not easily recognizable in hand specimen. Foliations were observed in 49 core pieces from Hole 894G, marked by their apparent dip on the half-cut surface. Complete orientations of these foliations relative to the axis of the borehole were obtained in 30 pieces by measurement of their apparent dips on half surfaces together with strikes on surfaces cut perpendicular to the axis of the core (Table 12). Recognition of a fabric tends to be dependent upon its orientation relative to the cut surface of the core: it is not obvious on non-cut surfaces or if its strike is near parallel to the "East–West" cut surface. For these reasons we regard our observation of the frequency of occurrence of the fabric to be an underestimate.

Magmatic foliations were observed only in core from Hole 894G and are patchily distributed. Foliation was first observed in Core 147-894G-4R (50 mbsf), but most observations and measurements refer to Cores 147-894G-12R to -13R (100 to 120 mbsf). The magmatic foliation is steeply dipping, between 50° and 90°, with a mean of 75° (Fig. 37) and standard deviation of 13°. Lineations were rarely measurable directly because it was not possible to cut the core in the appropriate plane; however, the significantly better quality of the foliation traces on vertical surfaces relative to horizontal surfaces suggests a steep trend for the mineral lineation relative to the axis of the core in all cases. This is confirmed by direct observation in three oriented thin sections.

The magmatic foliation is generally more well developed in the fine-grained gabbros, but a weak to moderate fabric also has been observed in some of the coarser grained gabbronorites. When an igneous contact between the finer grained gabbros and coarser gabbronorites is preserved, the magmatic foliation in the former is slightly oblique to, and cut by, the igneous contact, which normally has a steeper trend (Fig. 38; and see below). The coarser gabbronorite is usually poikilitic, with orthopyroxene oikocrysts giving rise to an isotropic texture; when foliated, the fabric may become moderately well developed and parallels the contact. These observations suggest that coarse-grained gabbronorite occurs as dikelets or veinlike patches that slightly postdate the main foliated fine-grained gabbro (see "Igneous Petrography of Holes 894F and 894G" section, this chapter).

The common characteristic of igneous structures observed in the gabbros of Hole 894G is their steeply dipping geometry. Whether this geometry is primary or related to later tilting is a first-order question. Some constraint is provided by the tentative restoration of core folia-

Table 12. Magmatic foliation data: strikes and dips and depths.

Core, section, piece	Feature locn (cm)	Depth (mbsf)	Core coordinates				Geog coord	
			Combined		Paleomag		Restored	
			strike	dip	dec	inc	strike	dip
147-894G-								
4R-2, 10	73	47.07	270	55	120.1	67.8	150	55
7R-2, 1	8	66.30	195	56	059.9	32.2	135	56
8R-2, 4	33	70.34	240	80	016.2	33.9	224	80
9R-4, 6	81	79.22	180	70	–026.4	60.3	206	70
9R-4, 11	128	79.69	120	90				
10R-1, 11	85	79.95	240	74	016.8	35.8	223	74
10R-1, 13	92	80.02	115	67				
10R-2, 2	12	80.60	249	52				
11R-2, 5	35	85.92	320	70	–102.2	35.0	062	70
12R-2, 4	42	95.74	045	90				
12R-2, 9	109	96.41	165	61				
12R-2, 10	136	96.68	180	50				
12R-2, 11	140	96.72	030	56				
12R-3, 8	147	98.23	050	70	–151.2	36.2	201	70
12R-4, 4	50	98.76	315	68	137.3	38.1	178	68
12R-5, 7	55	100.32	020	81	058.0	41.0	322	81
12R-5, 9	88	100.65	140	90				
12R-5, 11	110	100.87	230	73				
13R-1, 9	64	104.04	350	80				
13R-1, 11	92	104.32	175	90				
13R-2, 7	57	105.35	065	90				
13R-2, 8	92	105.70	020	76				
13R-2, 9	109	105.87	115	90				
13R-3, 1	12	106.37	100	90	142.4	43.6	318	90
13R-3, 8	85	107.10	170	65				
13R-3, 13	127	107.52	020	90				
17R-1, 10	65	126.45	260	84				
17R-1, 14	125	127.05	345	85	–035.4	49.9	020	85
18R-1, 10	80	131.70	000	85	093.8	48.9	266	85
18R-2, 4	23	132.56	045	72				

Notes: Feature locn (cm) = location of feature in centimeters from top of the section; dec = declination; inc = inclination; Geog coord = geographical coordinates.

tion measurements relative to the stable remanent magnetization directions of gabbro samples, which is discussed at the end of this chapter.

Microscopic Characteristics

All thin sections examined on board exhibit euhedral tabular plagioclase crystals (1 to 3 mm in length in gabbro; 2 to 4 mm in length in gabbronorite), flattened parallel to the (010) albite twinning plane, that are embayed by anhedral isometric clinopyroxene grains. In gabbronorite, large (5-mm-size) orthopyroxene oikocrysts include smaller (0.5 mm) euhedral plagioclase crystals. Some crystals of plagioclase are zoned, mainly in the gabbronorites (see "Igneous Petrography of Holes 894F and 894G" section, this chapter). All plagioclase crystals exhibit albite and sometimes pericline twinning, both of which are growth twins; no mechanical twinning or dynamic recrystallization, both of which are diagnostic of solid-state deformation, have been observed. The occurrence of undulose extinction in samples from the shallower portions of Holes 894F and 894G is thought to be related to later lower-temperature cataclasis (see below).

The gabbroic rocks from Site 894 do not therefore appear to have been subjected to high-temperature plastic deformation. We instead interpret their fabric to result only from the orientation of plagioclase crystals by or in a flowing magma. This is in profound contrast to gabbros from Hole 735B (Leg 118: Robinson, Von Herzen, et al., 1989; Cannat, 1991), but in accord with observations from some ophiolite complexes (e.g., Oman: Nicolas et al., 1988). The percentage of plagioclase crystals (50% on average) implies that they are often isolated from each other, and did not exhibit the tiling effect often observed in magmatic flow textures. The anhedral or poikilitic texture of both clinopyroxene and orthopyroxene indicates that these minerals crystallized late, and provides some constraint on the percentage of liquid present during magmatic flow. We infer, from the absence of intracrystalline deformation, that magmatic flow must have occurred in a crystal mush that contained a large amount (of the order of 40% to 50%) of interstitial liquid (Usselman and Hodge, 1978).

We were able to cut only a limited number of thin sections oriented properly (i.e., perpendicular to the foliation plane and approximately parallel to the lineation; other sections would in fact have been approximately parallel to the lineation). Only in the correctly cut thin sections was it possible to evaluate the quality of the fabric. We found that the fabric is controlled by two parameters: (1) the shape anisotropy of plagioclase crystals, and (2) their preferred orientation. Viewed in thin section, the shape anisotropy was relatively uniform, varying from 1:2 to 1:3. It was strongest in the fine-grained gabbros. A qualitative evaluation of the intensity of the fabric was classified (as per "Explanatory Notes" chapter, this volume) as 1, 2, or 3, based on preferred orientation of euhedral plagioclase crystals (illustrated in Figs. 39, 40, and 41, respectively). Quantification of preferred orientation intensity requires image analysis or U-stage measurements, which could not be performed on board.

Brittle Deformation

With the exception of undulose extinction of plagioclase and pyroxene in shear zones and possible rare subgrain development of plagioclase, deformation of Site 894 gabbros was accommodated entirely by brittle processes. Veins are numerous and occur throughout the section; nonmineralized fractures are rare in the recovered cores. Cataclastic shear zones are restricted to the upper portions of Holes 894C, 894F, and 894G, whereas minor distributed cataclasis (i.e., fault brecciation) is found locally throughout Hole 894G. Below is a summary of the microstructures and textures associated with cataclastic deformation and vein formation. Detailed structural descriptions of both the core and selected thin sections are found in Appendix D on the accompanying CD-ROM (see Fig. 15 of "Explanatory Notes" chapter for example).

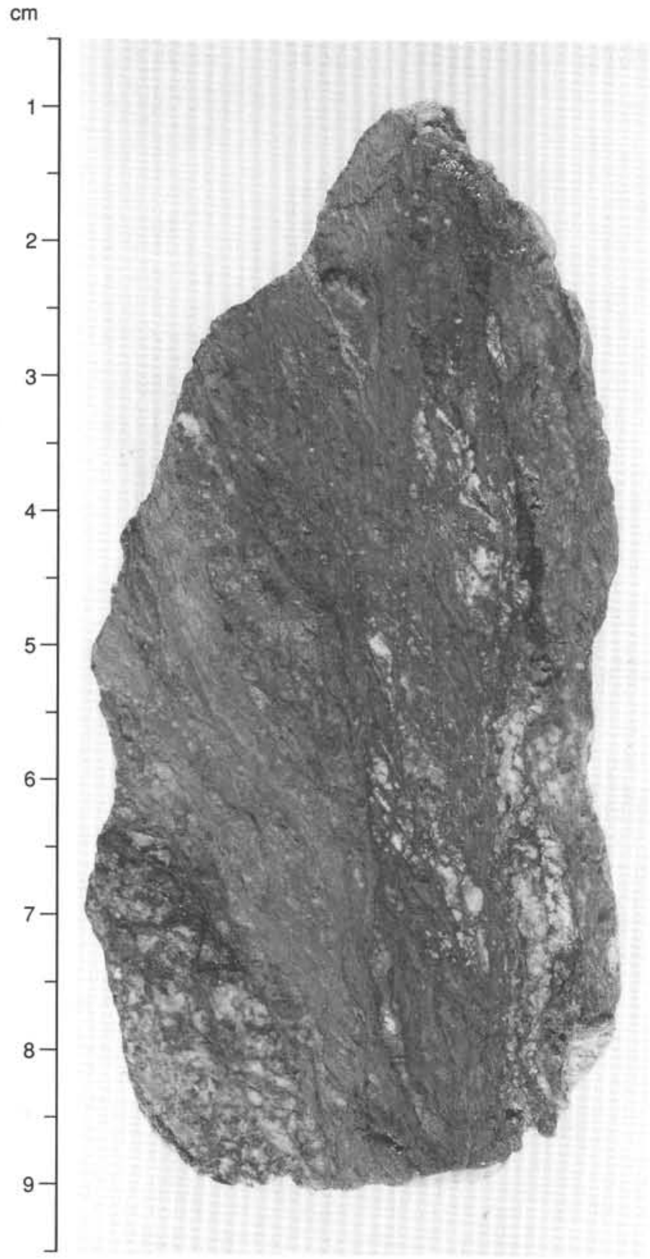

Figure 31. Foliated cataclasite in gabbro. Foliation rotates into shear surface. Shear sense, right side down (i.e., sub-vertical, normal shear zone) (Sample 147-894F-1R-1, Piece 1, 0–10 cm).

Cataclastic Deformation

Cataclastic deformation is a macroscopically ductile process if the deformation is localized into high-strain shear zones and cataclastic flow occurs. Several shear zones from Site 894 core were identified as cataclastic in origin following examination of thin sections, although it was difficult to distinguish them from mylonites in hand specimen.

The occurrence of localized shear zones with well-developed fault-rock fabrics is limited to Holes 894C and 894F and the upper portion of Hole 894G; these zones represent less than 1% of the cored interval. The locations of cataclastic shear zones from Site 894 core are listed in Table 13.

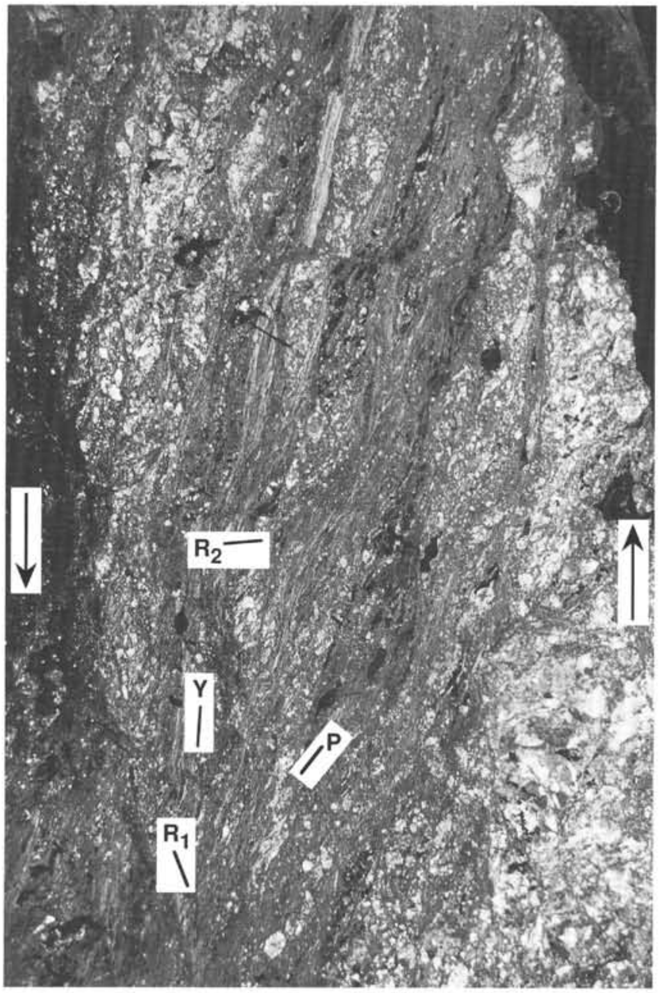

Figure 32. Photomicrograph of a portion of an oversized thin section of a foliated cataclasite. The ultrafine shear zones are clay-rich. Opaque minerals are sheared in the foliation and appear crenulated as a consequence of slip along R_1 shears. The cataclasite shows a well-developed Riedel shear array, including R_1, R_2, Y, and P shears (see "Structure" section, this chapter). Arrows indicate shear sense (Sample 147-894F-1R-1, Piece 1, 2–9 cm; field of view is 3.75 mm).

Macroscopic Observations

Cataclastic shear zones vary in their texture, ranging from homogeneously distributed zones of cataclasis, through development of protocataclasite to cataclasites and ultracataclasites, with increasing strain. Cataclastic shear is best developed in Hole 894G, Section 147-894G-2R-3, which contains a continuous subvertical shear zone that can be traced from 21.99–22.54 mbsf (from Pieces 5 to 12). This zone is characterized by a well-defined, narrow (5–10 mm) ultracataclasite band, with extensive associated alteration and later veining.

The ultracataclasites are extremely fine-grained, commonly contain angular to subrounded fragments, and are typically very thin. They range from 2–5 mm in width and form distinct zones of shear. The surrounding wall rock is commonly porphyroclastic and foliated, with the foliation being bent into the shear zone (e.g., Sample 147-894F-2R-1, Piece 7, 54–57 cm; Fig. 30). The more anastomosing, diffuse shear zones resemble mylonite zones: they are ductile in appearance, may be foliated and porphyroclastic, and less commonly possess "S-C" fabrics (Berthé et al., 1979; e.g., Sample 147-894F-1R, Piece 1, 0–10 cm; Fig. 31). Sense of shear indicators—rotation of foliation towards the shear zone, asymmetry of clasts, and "S-C" fabrics—indicate a normal sense of shear in all cases. Dips of the shear

Table 13. Cataclastic shear zone data: thickness, strikes and dips, and depths.

Sample	Feature		Thickness (cm)	True dip[a] (°)	Depth[b] (mbsf)
147-894B-					
1R-1, 0–8 cm	Cataclasis		8	Not oriented	
147-894F-					
1R-1, 0–10 cm	Ultracataclasite		10	70	0.05
2R-1, 26–42 cm	Protocataclasite		17	40	
2R-1, 46–52 cm	Protocataclasite		6		9.63
2R-1, 52–58 cm	Ultracataclasite		6	31	9.86
		Total	29		
3R-1, 14–21 cm	Ultracataclasite		7	42	19.09
3R-1, 34–39 cm	Ultracataclasite		5	Not oriented	
3R-1, 14–21 cm	Ultracataclasite		1	Not oriented	
3R-1, 68–84 cm	Hydrothermal breccia		14	Not oriented	
		Total	27		
147-894G-					
2R-3, 11–100 cm	Ultracataclasite		89	85	21.99
				90	22.13
				90	22.42
				90	22.42
				90	22.54
		Total	89		
		Total sheared core:	145		

[a] Relative to core.

[b] Curated depths.

zones vary (see Table 13). Veining and pervasive alteration is typically associated with cataclastic shear zones (see "Metamorphism" section, this chapter).

Microstructural Observations

In thin section most shear zones are demonstrably cataclastic in texture. They consist of an ultrafine-grained, dark to light brown matrix, probably clayey, within which are contained angular to rounded clasts of plagioclase, secondary amphibole, clinopyroxene, and opaques (Fig. 34). The clasts commonly display undulose extinction, particularly plagioclase, and are variably altered (up to 90%). A few cataclasites display moderately developed Riedel shear geometries, possessing R_1, R_2, Y, and rarely, a poorly developed P or callipygous shape fabric, defined by alignment of clasts and aggregates of clasts at an acute angle to the direction of shear (e.g., Fig. 32). Irregular and discontinuous veinlets predominantly of clay and zeolites crosscut the shear zones at a high angle to the shear zone boundary. In two samples, cataclasites are crosscut by large, blocky-textured prehnite veins (see "Metamorphism" section, this chapter). Veinlets of clay and zeolites also occur oriented at acute angles to the shear zone boundary, predominantly in an overprinting (crosscutting) geometry. Less commonly, however, the veinlets are sheared into the foliation, indicating syn-kinematic vein formation. The wall-rock texture adjacent to localized shear zones is that of a random-fabric cataclasite, with angular to rounded clasts of variable size in a clayey matrix. Grain size increases with distance from the ultracataclasite. In these areas grains are typically highly fractured and altered, commonly with fractures sealed by vein material.

The majority of the shear zones appear to have formed exclusively by cataclasis; however, one zone, Section 147-894F-1R-1 (Piece 1, 0–10 cm) (Fig. 31), appears to have formed predominantly by brittle mechanisms, accompanied by possible minor plastic deformation. In this sample, the local development of subgrains in plagioclase is common, although this may be due to intense microcracking (e.g. Tullis and Yund, 1987). The shear zone and foliation is defined by anastomosing ultrafine-grained layers, separated by lenses of protoclastic material. Opaque minerals and amphibole are commonly sheared and crenulated (Fig. 32). Plagioclase occurs as porphyroclasts that have undergone extreme grain-size reduction. Because of this rock's foliated appearance, we call it a "foliated cataclasite," following the terminology of Chester et al. (1985). Kinematic indicators identified include the rotation of foliations into the shear zone, synthetic microfaulting, asymmetric pods, and Riedel shear geometries; all indicate a normal sense of displacement.

Other areas of cataclasis are found in Sections 147-894G-12R-1, -16R-1, and -18R-2. No discrete slip surfaces were identified in either macroscopic or microscopic observations; rather, cataclastic material occurs in discontinuous, nonplanar pods and patches separated by highly altered and fractured minerals. Fractures in minerals, especially plagioclase, are commonly infilled with vein material (see "Metamorphism" section, this chapter). Brecciated vein material (commonly prehnite-chlorite) with incorporated wall-rock fragments was also observed.

Possible zones of intense alteration, veining, and fracturing are recognized by the retrieval of angular rubble, resembling fault breccia, that ranges in size from powder to 4–5 cm. Rubble was recovered in Sections 147-894G-11R-1 and 147-894G-12R-1. Although the actual brecciation of the core may be drilling-induced, it is possible that the core was initially heavily veined and fractured, as most pieces of the rubble have a green coating. X-ray diffraction determinations (see "Metamorphism" section, this chapter) show that this coating is predominantly chlorite and amphibole, with lesser amounts of diopside, plagioclase, and mixed-layer clays. This corresponds to the composition of the host rock veins, which are predominantly chlorite and amphibole. The diopside, clay, and plagioclase may have been incorporated into the surfaces by the drilling process.

Discussion of Cataclasites

The development of cataclasites rather than mylonites within shear zones indicates that the temperatures prevalent during shearing were too low to allow dynamic recrystallization of plagioclase. However, both plagioclase and pyroxene display undulose extinction, and less commonly plagioclase is locally subgrained, suggesting that a minimal amount of strain may have been accommodated by solid-state mechanisms during shear. The grain size of deformed plagioclase is commonly below the resolution of the optical microscope; thus by microscopic examination alone we cannot determine unequivocally whether plagioclase has undergone local dynamic recrystallization or severe comminution. However, taking into consideration the alteration mineralogy of the shear zones (see "Metamor-

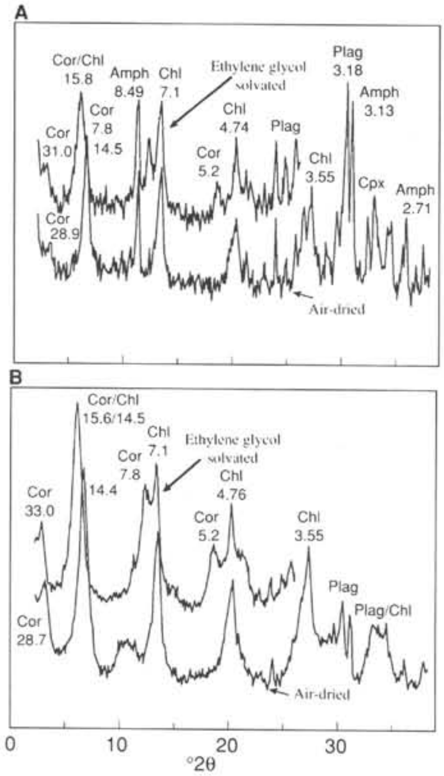

Figure 33. X-ray diffractograms showing peak positions and d-spacings (Å) for air-dried and ethylene glycol-solvated material from matrix material in cataclastic (A) and ultracataclastic (B) shear zones. Abbreviations are the same as used in Figure 25; Cor = corrensite. **A.** Sample 147-894F-2R-1, 27–36 cm. **B.** Sample 147-894F-3R-1, 52–58 cm.

phism" section, this chapter) it is unlikely that temperatures were higher than 400°C, which thus excludes the possibility of dynamic recrystallization. We conclude that the shear zones were formed by deformation processes that were almost exclusively brittle.

Igneous Contacts

Igneous contacts were measured at four locations in Hole 894G (Table 5). One contact is a coarse-grained gabbronorite in intrusive contact with a fine-grained gabbro; two contacts are a medium-grained gabbronorite in intrusive contact with a coarse-grained gabbronorite. The contact style varies from sharp and subplanar to irregular with associated minor fracturing. True dips of these contacts are 34° (Section 147-894G-18R-2, 25 cm; 132.6 mbsf), 47° (Section 147-894G-15R-1, 71 cm; 119.5 mbsf), and 85° (Section 147-894G-12R-2, 109 cm; 96.4 mbsf). The fourth contact (Section 147-894G-6R-2, 40 cm; 56.6 mbsf) is sheared, with a narrow, gently dipping, cataclastic zone (7° true dip) containing epidote fragments, that separates coarse-grained (above) from fine-grained poikilitic gabbronorite (below).

A porphyritic basalt dike intrudes gabbronorite in Section 894G-19R-1, 61–112 cm. The dike is vertical with a sharp but irregular chilled margin and associated brecciation and veining. In thin section the chilled margin is glassy and, for up to 7 mm away from the contact, there is a well developed preferred orientation of plagioclase laths. Numerous veinlets within the chilled margin either (1) terminate at the contact; (2) parallel the contact; or (3) crosscut the contact. The chilled margin is separated from the host rock by a zone of brecciation, containing highly fractured clasts of plagioclase and pyroxene in a fine-grained clay-plagioclase matrix. The fractured clasts are typically sealed with vein material. One smectite/chlorite vein has a fibrous morphology. The fibers are consistently sheared outside the brecciated zone, but become more irregularly sheared within the brecciated zone, possibly due to a change in vein orientation within the brecciated zone. Brecciation is probably due both to the pressure associated with dike intrusion and minor shearing.

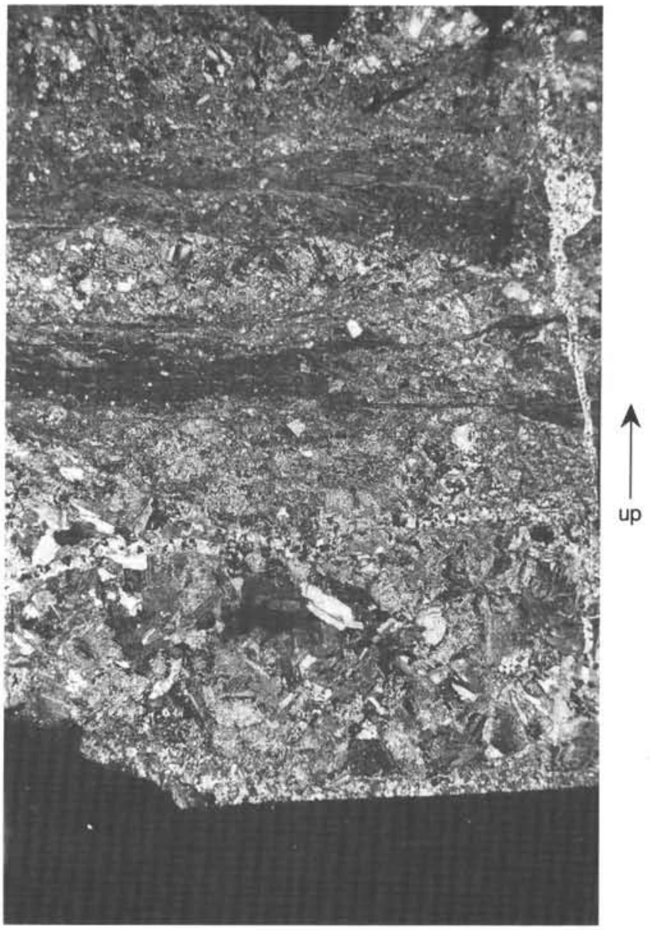

Figure 34. Full thin-section micrograph of ultracataclasite layers in a cataclastic gabbro. Shear zones contain sub-rounded to angular clasts of amphibole, pyroxene, plagioclase, and opaque minerals. Prehnite vein post dates shearing. Shear sense: top to left (i.e., normal) (Sample 147-894G-2R-3, Piece 11, 78–80 cm; field of view is 4 cm).

Veins and Fractures

Veins are the most ubiquitous and abundant structural feature identified in the Site 894 gabbroic rocks; they occur throughout the cored interval. Fractures without secondary mineral infilling were insignificant. Structural measurements were made on all veins that were approximately planar and sufficiently continuous to measure from each core piece that was reliably oriented relative to the axis of the borehole (448 veins). Of these data, all of which were initially measured relative to the core-liner coordinates, 86 were restored to geographical (i.e., magnetic) coordinates using shipboard paleomagnetic measurements. Their orientations are discussed at the end of this section.

Three generations of veins were identified based on the vein-filling mineralogy and crosscutting relationships (see "Metamorphism" section, this chapter). These are (from earliest to latest) (1) amphibole; (2) chlorite ± prehnite ± actinolite ± epidote; and (3) chlorite ± smectite ± zeolite ± calcite.

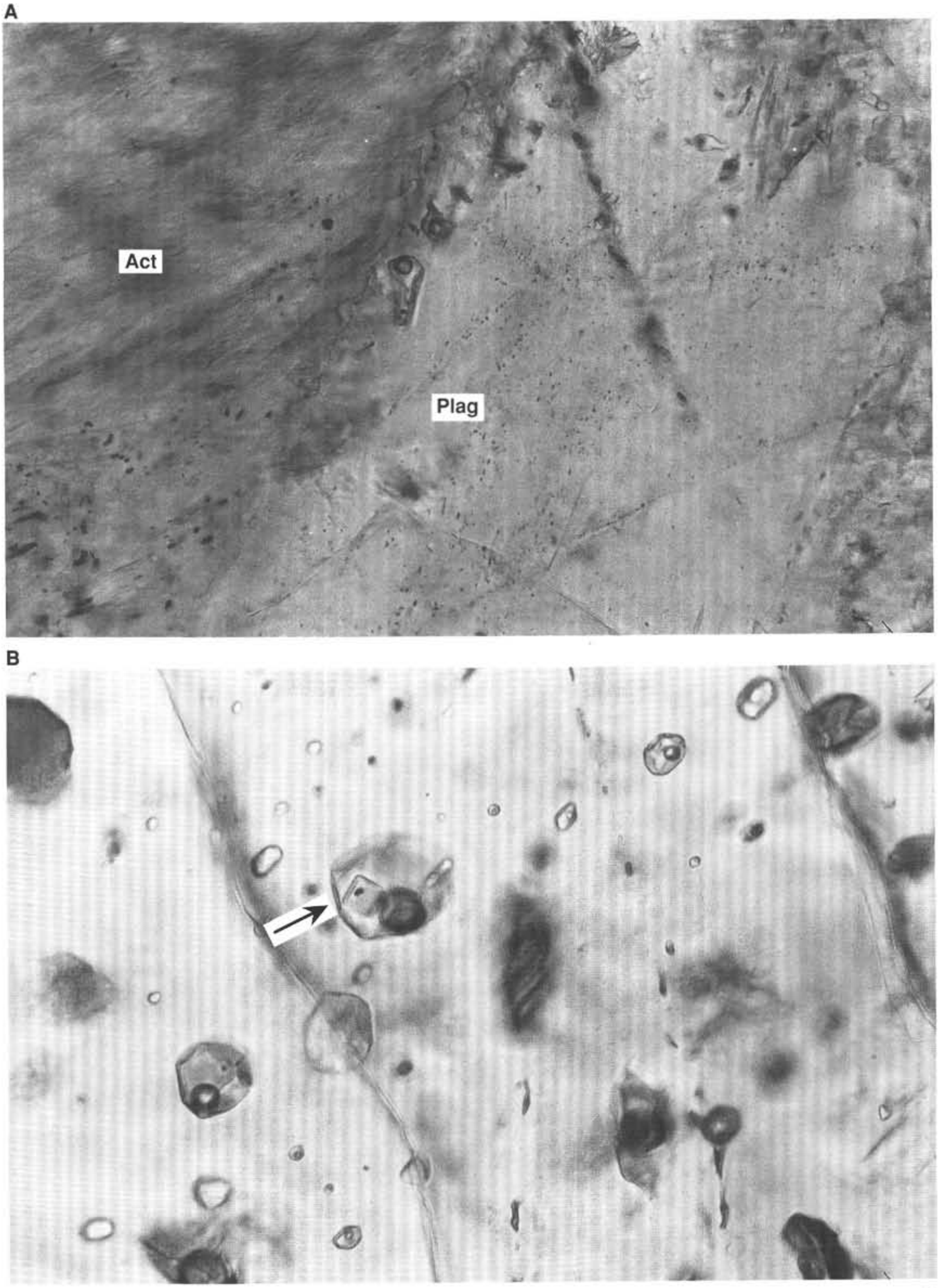

Figure 35. **A.** Type 1a fluid inclusion. Plagioclase-hosted (Plag), liquid-dominated secondary inclusion adjacent to actinolite (Act) after clinopyroxene. Largest inclusion is 12 µm in length. (Sample 147-894G-9R-4, Piece 11, 133–135 cm; field of view is 0.28 mm; plane light). **B.** Type 3b inclusions. Plagioclase-hosted, halite-bearing secondary inclusions. Halite daughter minerals commonly contain a fine-grained opaque mineral. These inclusions are commonly associated with vapor-dominated inclusions and likely formed by supercritical phase separation of a low-salinity fluid in the two-phase field. Large halite-bearing inclusion (arrow) is 22 µm in size (Sample 147-894G-9R-3, Piece 4, 48–50 cm; 0.14 mm across; plane light).

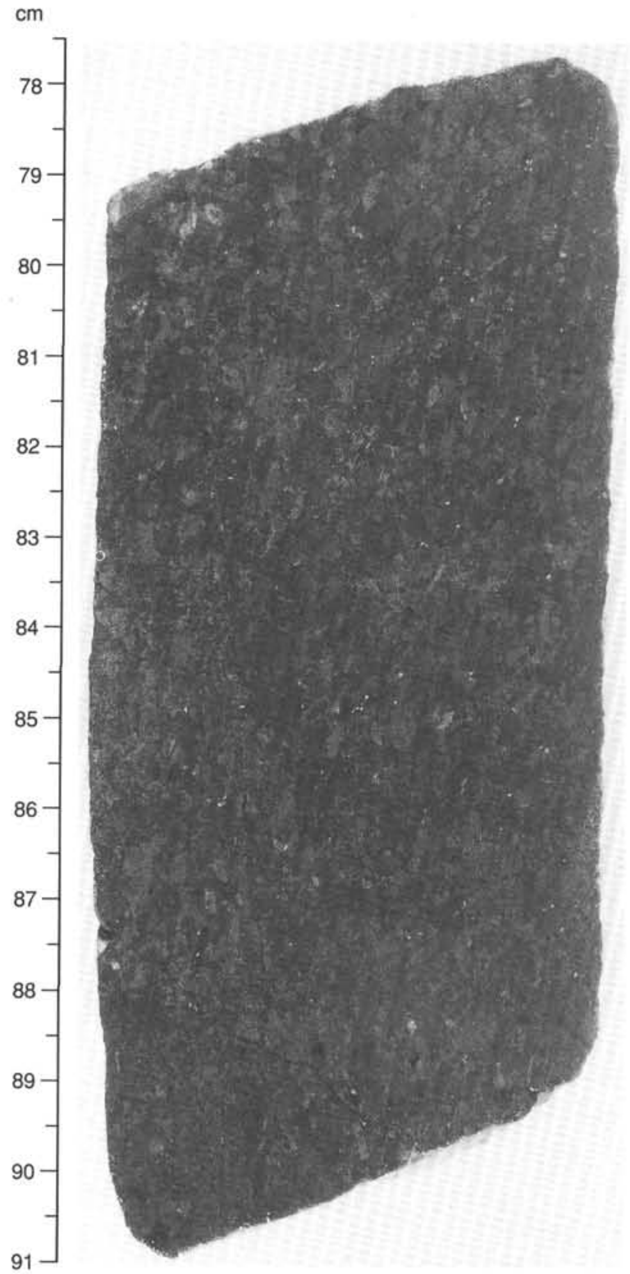

Figure 36. Photograph of a foliated gabbro. The magmatic foliation is marked by preferred orientation of euhedral plagioclase (vertical on the photograph) (Sample 147-894G-12R-5, Piece 9, 77–91 cm).

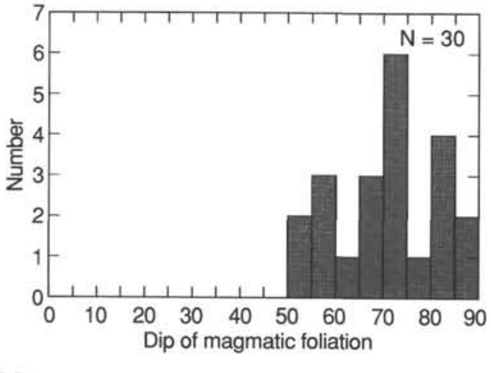

Figure 37. Histogram of dip of magmatic foliation, measured on 30 pieces.

Figure 38. Photomicrograph of an igneous contact between foliated fine-grained gabbro and coarse-grained gabbronorite. The foliation, well marked in the fine-grained gabbro, is oblique and crosscut by the igneous contact. Note the disymmetry of contacts, sharp at the bottom of the photograph, irregular to the top of the photograph. In coarse-grained gabbronorite, euhedral plagioclase crystals show a general tendency to orientate parallel to the igneous contact. Up in the core is to the left (Sample 147-894G-12R-2, Piece 9, 87–107 cm).

Macroscopic Observations

Veins in the Site 894 core are variable in morphology, ranging from either planar and continuous to irregular and discontinuous. Their average true dip is 55.8° (with standard deviation of 19.2°), this figure being influenced primarily by the regularly oriented, generally planar prehnite/chlorite veins (Fig. 42). The earlier amphibole-bearing veins tend to be more irregular in strike and are often shallowly dipping; later smectite/zeolite veins tend to have steeper dips. Shearing was noted on a few veins as demonstrated by the formation of mineral-filled pull-apart structures; these indicate normal displacement on a millimeter to submillimeter scale.

Microscopic Observations

In thin section, veins display a wide range of morphologies, ranging from relatively planar, continuous structures to curvilinear, discontinuous features with irregular and diffuse vein-wall-rock boundaries.

Amphibole Veins

These veins exhibit highly irregular wall-rock boundaries and have considerable variation in thickness due to the extensive alteration of

Figure 39. Photomicrograph of magmatic textural type 1 in fine-grained gabbronorite (thin section perpendicular to the foliation). Euhedral plagioclase crystals, representing 50% in volume, have variable grain size (3 × 1 mm to 2 × 0.5 mm); they are flattened on (010) plane and are more irregularly oriented, with an average trending (E–W on the photograph); they exhibit the same albite-carlsbad-pericline growth twin association. Anhedral crystals of clinopyroxene (1 to 2 mm) embaying plagioclase are devoid of shape fabric. Orthopyroxene oikocrysts (4 mm) include small euhedral plagioclase crystals (0.5 mm) not oriented. No trace of plastic deformation (Sample 147-894G-4R-1, Piece 16, 113–120 cm).

Figure 40. Photomicrograph of magmatic textural intensity 2 in fine-grained gabbro (thin section perpendicular to the foliation). Euhedral plagioclase crystals (2 × 0.5 to 1 mm), represent 60% in volume; they are flattened on (010) plane and mark a moderate preferred orientation with a bimodal tendency. Albite and carlsbad growth twins are associated with pericline twins in cross-hatched pattern. Anhedral crystals of clinopyroxene (2 mm) embaying plagioclase are devoid of shape fabric; no trace of plastic deformation (Sample 147-894G-10R-1, Piece 13, 85–87 cm).

wall-rock clinopyroxenes. They typically, although not always, have a minor component of shear indicated by kinked amphibole and elongated plagioclase. Shearing is typically restricted to the vein fill material itself.

Chlorite-Prehnite Veins

These veins tend to be associated with highly altered, fractured gabbros and with the cataclasites. They are typically zoned and rarely sheared, although, as with the amphibole veins, shearing is restricted to the vein fill itself. Chlorite fibers define a sharp contact with the vein walls; adjacent to this, a thin zone of fine-grained mixed-layer clays may occur, with the vein core filled with blocky prehnite. Prehnite typically occurs as lenticular pods separated by a complex network of clay veinlets and mesh textured chlorite.

Chlorite-prehnite veins also occur with a highly brecciated internal morphology (see "Metamorphism" section, this chapter). Mineral zoning within the vein is similar to that noted above, with the addition of a thin, well-defined layer of blocky prehnite adjacent to the clay layer. The cores of the veins consist of prehnite, commonly with fragments of angular plagioclase, altered clinopyroxene, and opaques. Both clinopyroxene and plagioclase display undulose extinction. Within the prehnite core, there are typically numerous discrete surfaces, subparallel to vein boundaries, which are either filled with chlorite or comminuted material and indicate that localized slip has occurred within the vein.

Chlorite/Smectite-Zeolite Veins

The latest veins are typically thin, sinuous, anastomosing, and discontinuous. They contain combinations of the minerals chlorite, smectite, zeolite, and calcite, usually as irregular coatings on fractures. They are frequently observed on the broken ends of core pieces. Zeolites usually have a radial morphology, although fibrous varieties do occur, and smectite is massive.

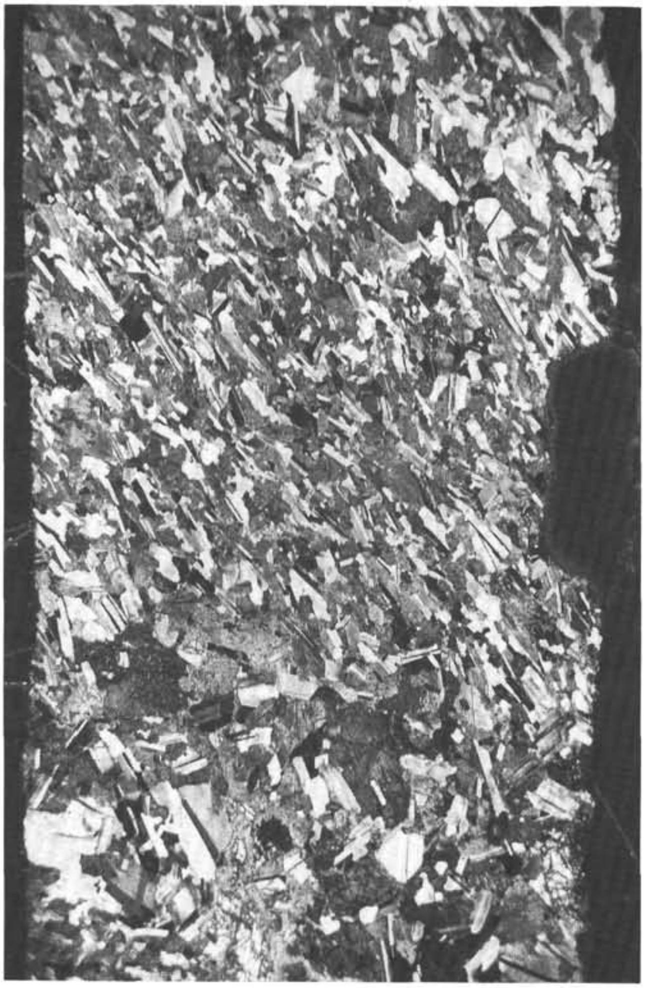

Figure 41. Photomicrograph of magmatic textural intensity 3 (i.e., strongly developed: see "Explanatory Notes" chapter, this volume) in fine-grained gabbronorite (thin section perpendicular to the foliation). Euhedral plagioclase crystals (2 × 0.5 mm), representing 50% in volume, are flattened on (010) plane, and exhibit a strong preferred orientation. Albite and carlsbad twins combined with rare pericline twins are growth twins, with no pinching of the twin lamellae. The largest plagioclase grains show corrosion boundaries with clinopyroxene. Anhedral crystals of clinopyroxene (1 to 2 mm) are embaying plagioclase. Poikilitic oikocrysts of orthopyroxene contain small (0.5 mm), nonoriented plagioclase crystals. None of the minerals exhibit any trace of plastic deformation (Sample 147-894G-12R-3, Piece 8, 72–95 cm).

Discussion of Veins

Most veins postdate the development of cataclastic shear zones (see "Metamorphism" section, this chapter); however, the smectite-zeolite-chlorite veins are syn- to post-shearing because they occur either crosscutting shear zones or, less commonly, are sheared themselves. Prehnite veins typically postdate the development of the cataclasite shear zones and are only rarely sheared. The mineralogically zoned nature of numerous veins suggests that they reflect multiple generations of fracture opening; that is, a fracture opens and is sealed with a certain mineralogy, it reopens and is then resealed. Because brecciated prehnite cores are lined with undeformed chlorite veins, the wall-rock clasts that are found within the prehnite cores must have been incorporated by fluid from elsewhere, transported along the fracture, and then deposited.

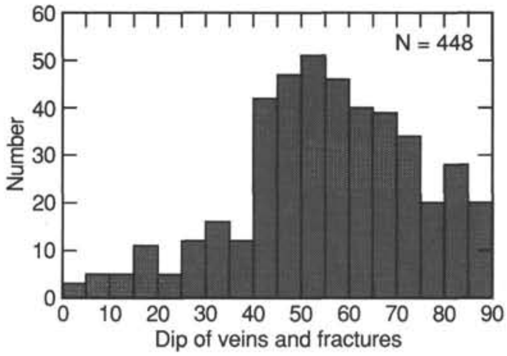

Figure 42. Histogram of vein dips. The average vein dip is 55.8°.

Reorientation of Structural Features

The only possible method of reorienting the Site 894 core structural measurements to geographical coordinates on board ship was with reference to paleomagnetic data. As discussed in the "Explanatory Notes" chapter, reorienting core in this way makes a number of assumptions. Foremost among these is that the stable magnetization vector for each sample, as isolated by alternating field or thermal demagnetization, reflects the primary magnetization acquired by the sample upon cooling, and originally pointed towards magnetic north, or south if of reversed polarity. If the 1 Ma estimate for the age of the rocks drilled at Site 894 is correct (see "Introduction and Principal Results" chapter, this volume), they should have formed during the Matuyama reversed polarity interval. In this case the magnetic declinations should be restored to south rather than (as here) north; however, because we have no direct constraint either on the age of these rocks or for their polarity (see "Paleomagnetism" section, this chapter), we have in all cases continued to plot the magnetic direction as if it were north.

One sample from Hole 894F and 21 samples from Hole 894G with stable magnetization vectors contained structural features that had been measured from the same contiguous core piece. From these data we were able to reorient 12 magmatic foliations, one cataclastic shear zone, and 86 veins and fractures, following the methodology described in the "Explanatory Notes" chapter. The magmatic foliations are few in number and show a spread of restored strike orientations (Fig. 43) that suggests a weak north–northeast maximum. The reoriented veins and fractures also display a variety of orientations relative to the stable magnetization direction, but with a well-defined preferred trend with west–northwest strike and steep south–southwest dip (Fig. 44). Much of this regularity appears to be due to the predominant second-generation greenschist facies chlorite-prehnite vein set described above and in the "Metamorphism" section (this chapter); otherwise, we have not been able to recognize any systematic relationship between orientation and either relative chronology or vein assemblage. The cataclastic shear zone (from Hole 894G, Section 147-894G-2R-3) also yields a westerly reoriented trend, with normal displacement down in the direction of magnetic inclination (i.e., north if of normal polarity, south if reversed).

When considering the significance of the restored magmatic foliations, veins, and fractures, it is pertinent to note the inclination of the stable magnetization direction of samples from Hole 894G. The structures presented in Figures 43 and 44 are reoriented with respect to azimuth only, yet the average magnetic inclination of the core is approximately 40° downwards (see "Paleomagnetism" section, this chapter). This is significantly different from the near-zero inclination expected for these latitudes, and strongly suggests that the section has been tilted to some degree, probably by tectonic means. Correction for this tilting can be made by restoring the magnetic inclinations to

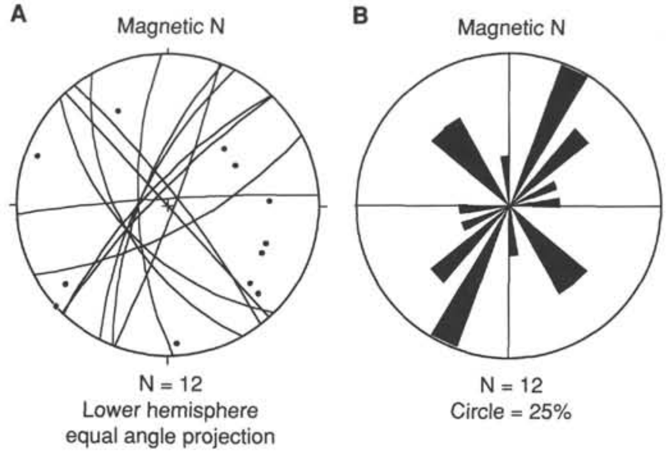

Figure 43. Magmatic foliations in gabbroic rocks from Hole 894G restored assuming that core paleomagnetic declinations point north. No inclination correction has been applied. **A.** Foliation planes and poles to planes (lower hemisphere equal angle projection). **B.** Rose diagram of foliation strikes.

zero (the supposed original inclination), and rotating all foliation and vein data by the same amount. This changes the mean strike of the magmatic foliation to one slightly nearer to north (Fig. 45), and brings the southerly dip of the predominant west–northwest vein set to vertical and its mean trend slightly closer to west (Fig. 46).

Discussion: Implications of Structural Data from Site 894

Magmatic Foliations

The magmatic foliation observed in Hole 894G gabbroic rocks is generally near-vertical and with a steeply plunging lineation, whether or not the effects of tilting are taken into account. The average trend of the foliation, restored with reference to core paleomagnetic data, is close to north, that is, near parallel to the strike of the East Pacific Rise (EPR) spreading axis (at which the gabbroic rocks of Site 894 are thought to have been created; see "Introduction and Principal Results" chapter, this volume).

The contrast between the structure of the gabbroic rocks we have recognized in Hole 894G and those of Hole 735B from Leg 118 is marked: the Hole 735B plutonic rocks have been affected by significant solid-state deformation, thought to be the result of amagmatic stretching of the crust under ductile deformation conditions (Robinson, Von Herzen et al., 1989; Cannat et al., 1991).

The geometry of magmatic flow at Site 894, on the other hand, is strikingly reminiscent of that reported from the upper part of the plutonic section of the Oman ophiolite, where detailed studies of the high-level gabbros have revealed the presence of steeply dipping magmatic foliations with steep lineations parallel to the strike of the overlying sheeted dike complex (Nicolas et al., 1988; MacLeod and Rothery, 1992). These authors have interpreted such fabrics as a record of the upward flow of melt at the top of the axial magma chamber into the base of the sheeted dike complex. We tentatively suggest that the magmatic fabrics of the Site 894 gabbros may be related to a similar process beneath the EPR axis.

Brittle Deformation

The only evidence for displacive deformation at Site 894 is in the cataclastic shear zones observed at shallow depths in Holes 894C, 894F, and 894G. Their brittle deformation style and associated metamorphic assemblage suggests that deformation occurred at temperatures of less than 400°C. They all indicate normal displacement and, with the westerly restored orientation of the vertical cataclasite zone in Section 147-894G-2R-3, are most probably related to rifting processes associated with uplift of the intrarift ridge within Hess Deep.

The magnetic data have allowed us to reorient a large number of the hydrothermal veins that traverse the core. These veins, which are dominated by chlorite-prehnite greenschist facies assemblages, represent the filling of tensile fractures. Restoration of these veins shows them to have a preferred west–northwest strike and steep or vertical dip. This orientation strongly suggests that they are related to the rifting of the Cocos and Nazca plates that led to formation of the Hess Deep rather than to extension at the EPR. This in turn suggests that the EPR crust and its associated hydrothermal alteration system were influenced by Cocos-Nazca-related rifting very soon after its formation.

GEOCHEMISTRY

Introduction

In all, 25 whole-rock samples from Site 894 were analyzed using X-ray fluorescence (XRF) for major oxide compositions and abundances of the trace elements Nb, Zr, Y, Sr, Rb, Zn, Cu, Ni, Cr, V, Ce,

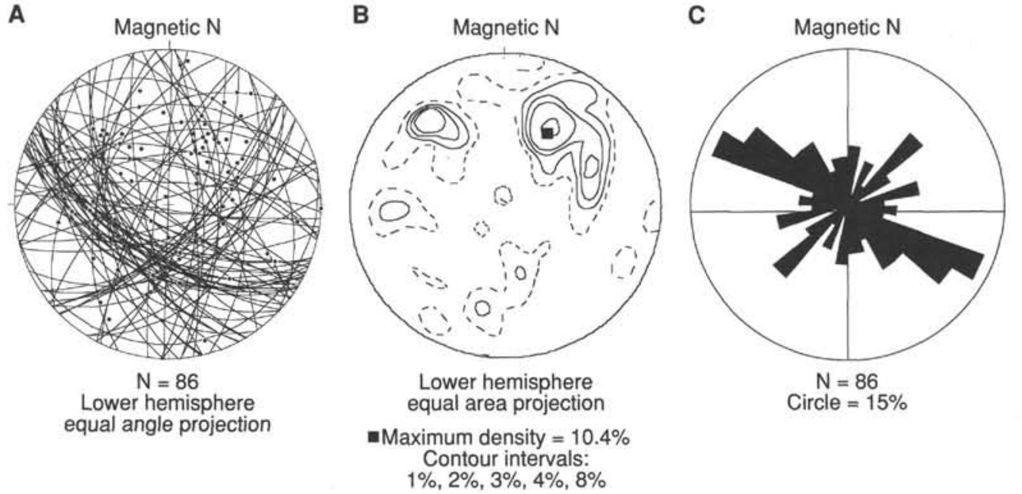

Figure 44. Veins and fractures in gabbroic rocks restored assuming that core paleomagnetic declinations point north. No inclination correction has been applied. **A.** Foliation planes and poles to planes (lower hemisphere equal angle projection). **B.** Contoured equal angle plot of poles to foliation planes (lower hemisphere equal area projection). **C.** Rose diagram of foliation strikes.

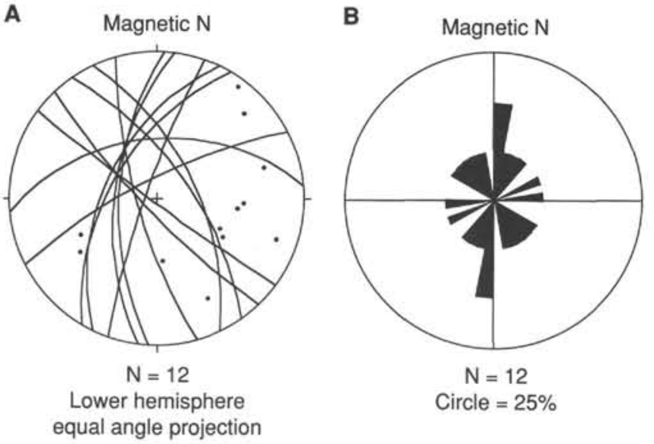

Figure 45. Magmatic foliations in gabbroic rocks from Hole 894G restored assuming that core paleomagnetic declinations point north, and assuming the mean inclination to be zero. **A.** Foliation planes and poles to planes (lower hemisphere equal angle projection). **B.** Rose diagram of foliation strikes.

and Ba. The samples were also analyzed using gas chromatography for H, C, and S contents. Sample preparation techniques and analytical procedures are outlined in the "Geochemistry" section of the "Explanatory Notes" chapter, this volume. The chosen rock samples represent 10 out of the 13 lithostratigraphic units from Hole 894G.

The results are presented in Table 14. Nb and Rb abundances were below detection limits (<1–2 ppm) for all samples analyzed. Ba and Ce are also not reported, due to large analytical errors. The loss-on-ignition (LOI) values provide only limited information on the amount of bound water and other volatiles in the rocks, because the loss of weight from removing volatiles is counterbalanced by oxidation of the ferrous iron. Thus, a comparison of H_2O contents as determined by gas chromatography and LOI in Table 14 shows that in most cases the LOI is less than the amount of H_2O.

Alteration Effects

The rocks have all undergone some degree of alteration (see "Metamorphism" section, this chapter). In choosing samples for geochemical analysis, an attempt was made to select the least altered material based on hand-specimen observations. A representative thin section was made for each rock sample chosen for analysis. In most cases, the thin section was taken from within the interval of the rock sample; if not, it was made from a rock sample immediately adjacent to the chosen geochemical rock sample. Petrographic observation of the rock samples chosen for geochemistry reveals that the amount of modal alteration varies from 6 to 85 modal percent (see Table 14). The amount of H_2O determined in the rocks ranges from 0.46 to 4.4 wt%. To evaluate the effects of alteration on the geochemistry of the rock samples, major and trace element abundances were plotted against H_2O and modal percent alteration. Because no significant correlations were found, we infer that the geochemistry of the gabbro samples has not been seriously affected by alteration. This conclusion is preliminary, as we have not yet fully sampled altered rock samples from Site 894. The same preliminary conclusion cannot be applied to the basaltic dikes in Hole 894G due to the limited amount of data on their compositions that were obtained at Site 894.

Hole 894E, 894F, and 894G Gabbros

Of the 25 samples chosen for geochemistry, 22 are gabbros and gabbronorites. In general, olivine-bearing samples have higher Ni, but otherwise there is no apparent difference in chemistry among the analyzed gabbroic and gabbronoritic rock types. The samples are broadly similar to primitive, highly incompatible element depleted N-MORB, with very low TiO_2 (typically well below 1%), K_2O (typically below 0.1%), Sr (<110 ppm), and Zr (typically <50 ppm).

Hole 894G Basaltic Dikes

Major and trace element geochemistry confirms the petrographic observations based on phenocryst assemblages (see "Igneous Petrography of Holes 894F and 894G" section, this chapter) that these basaltic dikes represent relatively primitive magma types when compared with the more evolved basaltic glass compositions sampled along the East Pacific Rise (EPR) (Allan et al., 1989) and exposed in the north and south walls of Hess Deep (J. Natland, unpubl. data). The primitive nature of the basaltic dikes is reflected in their high Mg# (67–69) values, Ni (254 ± 70 ppm) and Cr (462 ± 222 ppm) and low Zr (46 ± 1.5 ppm) and Y (20 ± 1.5) abundances.

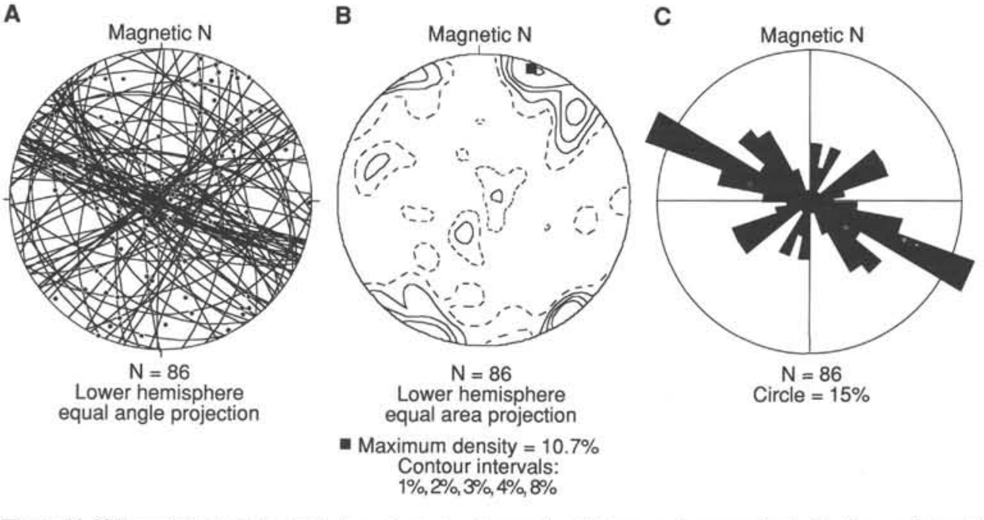

Figure 46. Veins and fractures in gabbroic rocks restored assuming that core paleomagnetic declinations point north, and assuming the mean inclination to be zero. **A.** Foliation planes and poles to planes (lower hemisphere equal angle projection). **B.** Contoured equal angle plot of poles to foliation planes (lower hemisphere equal area projection). **C.** Rose diagram of foliation strikes.

Table 14. Chemical composition of rock samples from Holes 894E, 894F, and 894G.

Hole:	894E	894F	894G	894G	894G	894G	894G	894G	894G	894G	894G	894G
Core-section:	3R-1	3R-1	2R-1	2R-2	2R-3	4R-1	5R-1	6R-2	7R-1	7R-1	9R-3	9R-4
Interval (cm):	62-70	98-103	60-65	95-100	20-26	113-119	30-34	79-87	56-66	76-84	133-139	100-144
Piece:	10	17	9	15	4	16	9	6	11	13	11	8,9,10,11
Depth (mbsf):	19.5	17.8	29.2	31.1	31.8	47.3	50.3	57	65.4	65.6	78.2	79.3
Igneous unit:	4	1	2	2	3	4	6	6	6	6	7	7
Lithologic type:	G	OG	B	B	OG	GN	GN	GN	GN	GN	OGN	OGN
SiO_2	52.69	50.13	48.72	48.29	52.48	51.81	51.31	51.93	49.46	51.95	49.67	49.13
TiO_2	0.78	0.56	0.96	0.91	0.46	0.89	0.76	0.81	0.43	0.65	0.61	0.42
Al_2O_3	15.32	16.87	17.86	18.69	13.32	14.87	15.20	13.95	15.11	16.36	17.19	17.40
FeO	7.70	7.07	8.13	7.71	8.95	7.67	6.96	7.71	8.99	7.07	8.56	8.15
MnO	0.18	0.13	0.15	0.14	0.18	0.16	0.15	0.16	0.16	0.15	0.15	0.13
MgO	8.30	9.15	9.67	9.37	11.48	8.28	8.34	9.69	11.34	8.36	9.85	10.05
CaO	10.61	12.95	12.04	12.17	7.56	14.38	14.09	13.37	12.24	12.31	11.89	12.20
Na_2O	3.57	2.13	2.13	2.03	4.14	2.24	2.26	2.23	1.82	2.55	2.22	2.08
K_2O	0.08	0.05	0.05	0.05	0.29	0.05	0.05	0.06	0.08	0.05	0.12	0.07
P_2O_5	0.05	0.04	0.07	0.06	0.03	0.06	0.06	0.08	0.03	0.05	0.04	0.03
Total	99.28	99.08	99.77	99.44	98.89	100.42	99.19	99.99	99.65	99.50	100.29	99.65
LOI	1.48	0.97	1.80	2.06	3.46	0.40	0.55	0.52	0.70	0.43	0.72	0.70
H_2O	2.28	1.49	2.21	2.48	1.50	0.87	0.80	1.13	1.23	0.80	1.47	1.19
CO_2	0.04	0.00	0.00	0.04	0.33	0.10	0.00	0.00	0.00	0.00	0.00	0.00
S	0.29	0.29	0.30	0.32	0.97	0.12	0.05	0.05	0.08	0.02	0.08	0.06
Sr	114	98	88	88	65	92	92	83	89	100	99	105
Zr	37	23	48	45	18	43	39	34	18	30	21	15
Y	21	12	21	20	11	23	19	17	10	15	10	9
V	236	187	156	153	162	279	271	243	161	205	163	139
Cr	142	668	381	291	507	404	357	331	540	221	309	310
Ni	84	110	224	205	190	101	97	101	193	62	137	149
Cu	41	54	81	76	190	81	58	91	82	40	84	84
Zn	49	34	43	41	470	36	28	38	52	35	49	47
Mg/(Mg+Fe)	65.7	76.5	67.9	68.4	60.1	65.8	68.1	69.1	69.2	67.8	67.2	68.7
Ca/(Ca+Na)	62.2	77.1	75.8	76.8	50.2	78.0	77.5	76.8	78.8	72.7	74.7	76.4
MgO/Al_2O_3	54.2	54.3	54.1	50.2	86.2	55.7	54.9	69.4	75.0	51.1	57.3	57.8
Modal % alteration	74.3	16.3	11.7	20.0	84.8	26.0	52.0	22.0	22.5	31.0	42.0	33.0

Notes: G = gabbro; Og = olivine gabbro; Gn = gabbronorite; Ogn = olivine gabbronorite; B = basalt. All iron is reported as FeO. All ratios multiplied by 100.

Chemical Stratigraphy of Hole 894G

The chemical stratigraphy of Hole 894G can be summarized by examining the variation in the compatible element Cr and the incompatible element Zr with depth, as presented in Figures 47A and 47B. An important and significant observation is that the overall decrease in Cr abundances with depth (Fig. 47A) demonstrates that the gabbroic rocks become more evolved downhole in Hole 894G, which is consistent with the petrographic observations. In contrast, Zr shows no consistent variation downhole.

PALEOMAGNETISM

Introduction

Paleomagnetic measurements were made on 35 minicores cut from core recovered from Holes 894F and 894G. The results of these measurements are displayed in Tables 15 and 16. The general goal of these measurements was to characterize the magnetic properties of lower crustal rocks formed at a fast-spreading center and to describe their variation as a function of lithology, alteration, and depth within the crustal section.

In addition to measurements made on minicore samples, magnetic susceptibility was measured on whole core using the multisensor track (MST); remanent magnetization of the archive half of the split core was measured using the cryogenic magnetometer. However, because of the measuring radius of the sensors on these two instruments, data collected from small pieces (<15 cm for susceptibility and <20 cm for remanence) had high errors and were not included in our database. A full description of measurement techniques is included in the "Paleomagnetism" section of the "Explanatory Notes" chapter, this volume.

Intensity of Natural Remanent Magnetization

Values of the intensity of natural remanent magnetization (J_0) for minicore samples are displayed in Table 15 and plotted vs. depth in Figure 48. Although J_0 was not measured for three samples, we used the magnetization values measured after an alternating field demagnetization (AFD) step of 1 mT as the J_0 value for these samples. This estimate of J_0 probably has an error of less than 10%, because these samples were very stable against AFD. For an additional 6 minicore samples, remanent magnetization was measured incorrectly up to the AFD step of 6 mT because of an error in the gain setting of one axis of the cryogenic magnetometer. Thus, J_0 values were determined for 29 of the 35 minicore samples. The J_0 values range from 0.03 to 7.2 A/m with an arithmetic mean of 2.0 A/m (Figs. 48 and 49).

Measurements of natural remanent magnetization (NRM) made on the half cores (110 total) resulted in a mean J_0 value of 1.5 A/m, which is similar to the value determined from minicore measurements. However, the half-core range of 0.14 to 3.8 A/m was somewhat smaller than that observed for the minicore measurements (Figs. 48 and 49). The smaller range in values probably occurs because the half-core measurements average a larger volume of rock than do the minicore samples. Therefore, the half-core measurements probably provide a better estimate of the average magnetization of the drilled section than do the minicores, but a poorer estimate of the extremes in magnetization values. The larger number of half-core measurements (110 compared to 29 minicore measurements) provides a more continuous record of the variability in remanent magnetization downhole (Fig. 48).

The observed variation in J_0 values of Hole 894G samples is similar to that reported for gabbros dredged from the Mid-Atlantic Ridge by Kent et al. (1978) (0.01–31.4 A/m) but much narrower than that reported for gabbros from the Southwest Indian Ridge (Kikawa and

Table 14 (continued).

Hole:	894G	894G	894G	894G	894G	894G	894G	894G	894G	894G	894G
Core-section:	11R-2	11R-3	11R-3	12R-2	13R-2	13R-2	13R-3	17R-1	19R-1	19R-1	20R-1
Interval (cm):	100-107	17-28	31-38	37-45	6-13	90-98	17-24	50-58	49-55	84-96	19-26
Piece:	10D	3A	4	4E	1B	8	1B	10A	9	13	4
Depth (mbsf):	86.6	87.2	87.3	95.6	105	106	106	126	141	141	146
Igneous unit:	9	9	9	11	11	11	11	11	12	12	13
Lithologic type:	GN	GN	GN	GN	GN	GN	GN	GN	B	GN	GN
SiO_2	51.43	52.13	51.51	52.11	53.14	52.14	51.86	51.55	47.44	52.71	51.67
TiO_2	0.47	1.10	0.49	0.46	0.61	0.50	0.85	0.54	0.94	0.74	0.43
Al_2O_3	15.77	12.39	15.14	17.92	17.26	15.89	14.57	14.98	19.68	16.22	16.71
FeO	7.92	10.20	7.23	6.99	6.57	7.21	9.03	6.62	7.78	7.67	7.23
MnO	0.16	0.20	0.16	0.14	0.12	0.15	0.17	0.15	0.13	0.15	0.15
MgO	9.47	9.62	9.00	7.70	7.32	8.96	9.25	8.92	9.86	7.97	9.16
CaO	12.88	11.71	13.84	11.23	11.39	13.10	11.25	14.53	10.84	11.16	12.39
Na_2O	2.16	2.15	2.11	2.97	3.11	2.21	2.47	2.16	2.36	3.08	2.27
K_2O	0.06	0.06	0.05	0.08	0.06	0.04	0.06	0.04	0.10	0.12	0.07
P_2O_5	0.02	0.07	0.02	0.03	0.05	0.02	0.04	0.02	0.06	0.07	0.02
Total	100.35	99.62	99.56	99.62	99.63	100.21	99.55	99.51	99.19	99.89	100.10
LOI	0.49	0.39	0.57	0.96	0.65	0.41	0.43	0.54	2.92	0.40	0.59
H_2O	0.91	0.97	0.46	1.37	1.06	0.96	0.99	0.65	4.40	1.20	1.65
CO_2	0.00	0.00	0.00	0.00	0.00	0.07	0.00	0.00	0.00	0.00	0.00
S	0.06	0.08	0.05	0.07	0.00	0.70	0.03	0.05	0.17	0.00	0.11
Sr	92	79	90	111	111	93	88	85	91	106	84
Zr	13	91	13	20	45	12	35	14	46	47	12
Y	10	32	11	13	17	12	19	14	18	21	10
V	206	317	211	160	172	210	278	226	189	251	182
Cr	392	156	415	145	67	304	133	478	714	80	225
Ni	113	78	101	58	52	83	76	94	334	58	120
Cu	80	61	82	45	12	73	48	82	78	19	82
Zn	44	68	36	37	19	38	48	28	48	29	40
Mg/(Mg+Fe)	68.1	62.7	68.9	66.3	66.5	68.9	64.6	70.6	69.3	64.9	69.3
Ca/(Ca+Na)	76.7	75.1	78.4	67.6	66.9	76.6	71.6	78.8	71.7	66.7	75.1
MgO/Al_2O_3	60.0	77.7	59.4	42.9	42.4	56.4	63.5	59.5	50.1	49.1	54.8
Modal % alteration	15.0	45.0	30.0	21.5	30.0	33.4	32.1	6.0	80.0	56.0	17.0

Pariso, 1991; 0.0026–130 A/m). Although the range of values observed from Hole 894G samples is smaller, the mean J_0 value for Hole 894G samples is similar to that of Leg 118 gabbros (1–2 A/m; Kikawa and Ozawa, 1992; Pariso and Johnson, in press). The mean J_0 value for Hole 894G is also similar to that of DSDP/ODP oceanic basalts older than 2 Ma (3.5 A/m; Harrison, 1987; Johnson and Pariso, 1993).

Magnetic Susceptibility

Values of magnetic susceptibility (k) for minicore samples and whole cores from Hole 894G are plotted vs. depth in Figure 50. The susceptibility values for minicores vary over two orders of magnitude, from 0.0006 to 0.06, and have an arithmetic mean of 0.016. However, most of the values lie in the range between 0.005 and 0.05, which is consistent with previous studies of oceanic gabbros (Fox and Opdyke, 1973; Kent et al., 1978; Dunlop and Prevot, 1982; Kikawa and Pariso, 1991). The whole-core susceptibilities have a range similar to the minicore measurements and an identical mean value (Figs. 50 and 51).

Like NRM intensities, the high sample density of the half-core susceptibility measurements allowed continuous observation of downhole variations in magnetic susceptibility (Fig. 50). Comparison of Figures 48 and 50 indicates that the variation in susceptibility with depth correlates with NRM intensities, suggesting that NRM intensities are largely dependent upon the concentration of magnetic minerals.

Koenigsberger Ratio

The Koenigsberger ratio (Q) compares the relative importance of the remanent magnetization with the magnetization induced in the formation by the Earth's magnetic field. Koenigsberger ratios were calculated using the equation $Q = J_0\mu_0/kH$, where μ_0 is the permeability of free space and H is the value of the ambient geomagnetic field at Site 894 (33×10^{-6} T; Merrill and McElhinny, 1983). Figure 52 shows that Q values for Hole 894G samples lie between 1 and 10, comparable to those of other oceanic gabbros (Fox and Opdyke, 1973; Kikawa and Pariso, 1991), indicating that the in-situ magnetization of these rocks is dominated by a remanent magnetization rather than an instantaneous magnetization induced by the Earth's magnetic field.

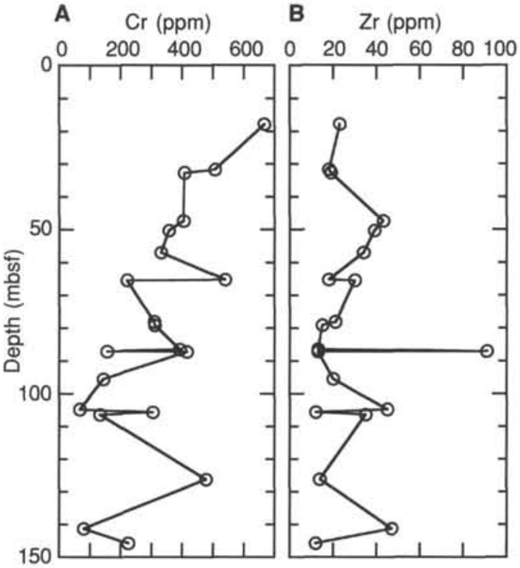

Figure 47. Variation in Cr (**A**), and the variation in Zr abundances (**B**) with depth for gabbroic rocks in Hole 894G.

Demagnetization Characteristics of NRM

Minicore samples from Holes 894F and 894G were demagnetized using both thermal and alternating field (AF) demagnetization techniques (Figs. 53 and 54, respectively). AF demagnetization was used

Table 15. Magnetic property values for minicores sampled from cores recovered from Holes 894F and 894G.

Core, section, interval (cm)	Piece number	Depth (mbsf)	NRM (A/m)	Susceptibility (SI units)	Koenigsberger ratio	MDF (mT)	Stable declination	Stable inclination	Rock type
147-894F-									
2R-1, 5–7	5	9.35	1.51	1.63E-02	4	0.8	94	54	Gabbro
3R-1, 26–28	3	17.06	0.79	3.24E-03	9	6	87	–30	Olivine gabbro
147-894G-									
2R-1, 68–70	9	29.28	0.66	7.95E-03	3	23	75	27	Phyric basalt
2R-2, 110–112	15	31.20	0.88	9.46E-03	4	19	–160	18	Phyric basalt
2R-3, 32–34	5	31.87	0.07	2.39E-03	1	36	–133	3	Olivine gabbro
2R-3, 118–120	14	32.73	1.21	3.48E-02	1	6	ND	ND	Olivine gabbro
4R-2, 76–78	10	47.10	0.25	8.52E-04	11	17	120	68	Gabbronorite
6R-1, 26–28	4a	55.06	0.95	6.39E-03	6	41	–147	39	Gabbronorite
6R-1, 89–91	8a	55.69	0.76	1.13E-02	3	17	53	66	Gabbronorite
6R-2, 78–80	6	57.01	1.76	1.67E-02	4	13	–28	30	Gabbronorite
7R-2, 6–8	1	66.26	1.72	1.05E-02	6	20	60	32	Gabbronorite
8R-1, 54–56	5a	69.04	0.69	1.20E-02	2	13	–104	26	Gabbronorite
8R-2, 31–33	4	70.31	2.14	1.01E-02	8	34	16	34	Gabbronorite
9R-2, 86–88	5a	76.51	1.67	1.47E-02	4	44	ND	ND	Gabbronorite
9R-3, 69–71	5c	77.60	1.34	3.56E-02	1	4	72	12	Gabbronorite
9R-4, 74–76	6	79.07	1.30	1.18E-02	4	ND	–26	60	Olivine gabbronorite
9R-4, 130–132	11	79.63	1.31	1.59E-02	3	9	ND	ND	Olivine gabbronorite
10R-1, 81–83	13a	79.91	2.19	1.38E-02	6	63	17	36	Gabbro
11R-2, 45–47	5	86.01	1.14	6.87E-03	6	71	–102	35	Gabbronorite
12R-2, 50–52	4e	95.76	4.71	2.73E-02	7	73	83	44	Gabbronorite
12R-3, 147–149	8b	98.20	ND	1.30E-02	ND	ND	–151	36	Gabbronorite
12R-4, 49–51	4c	98.74	ND	1.73E-02	ND	ND	137	38	Gabbronorite
12R-5, 64–66	7d	100.37	4.39	4.55E-02	4	ND	58	41	Gabbronorite
12R-5, 79–81	9	100.52	5.96	5.55E-02	4	7	–12	47	Gabbronorite
13R-3, 5–7	1a	106.28	7.20	4.02E-02	7	20	142	44	Gabbronorite
14R-1, 70–72	11	113.80	ND	1.19E-02	ND	ND	–157	69	Gabbronorite
16W-1, 43–45	7	123.23	ND	1.74E-02	ND	ND	117	2	Gabbronorite
15R-1, 73–75	12	119.53	3.82	1.79E-02	8	ND	–132	45	Gabbronorite
17R-1, 123–125	14	127.03	3.50	1.15E-02	12	38	–35	50	Gabbronorite
17R-2, 7–9	1a	127.31	2.67	1.32E-02	8	38	127	51	Gabbronorite
18R-1, 69–71	10a	131.59	2.39	5.03E-03	18	42	94	49	Gabbronorite
18R-2, 94–96	14	133.26	0.27	6.80E-03	2	22	34	65	Gabbronorite
19R-1, 72–74	12	141.22	0.03	5.52E-04	2	17	ND	ND	Phyric basalt
20R-1, 60–62	10	146.20	ND	1.23E-02	ND	ND	–49	44	Gabbronorite
20R-3, 56–58	9	147.98	ND	2.15E-02	ND	ND	ND	ND	Gabbronorite

Notes: ND refers to values that were not determined. MDF = median destructive field.

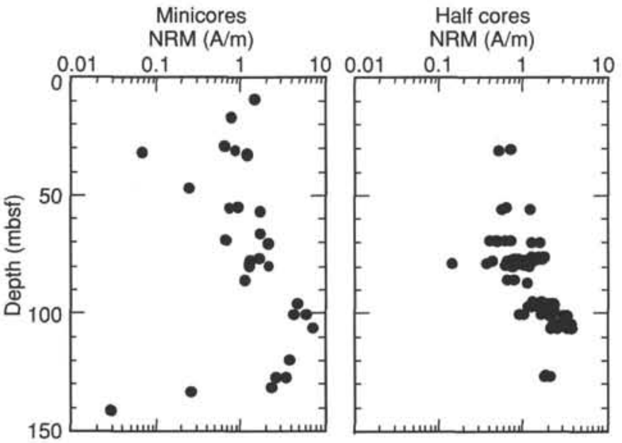

Figure 48. Plots of the intensity of NRM vs. depth in Hole 894G for minicores and half core samples.

for most samples because it is a nondestructive process that leaves the samples suitable for other types of studies. Thermal demagnetization was performed on three samples to help constrain the blocking temperature of the NRM, a parameter that is dependent both on the composition and grain size of magnetic minerals. To identify the blocking temperature spectra of the hardest portion of remanent magnetization, three samples were subjected to thermal demagnetization after stepwise AF demagnetization up to 100 mT.

The NRM of minicore samples from Hole 894G was generally resistant to thermal demagnetization. The sharp decrease in the magnetization evident around 550°C in the thermal demagnetization curves (Fig. 53) suggests that the NRM is carried by a single magnetic phase. This phase is most likely relatively pure magnetite, which has a Curie temperature between 550° and 580°C. This is consistent with the observation that secondary magnetite (which is generally titanium-poor) was commonly observed within olivine and pyroxene grains (see "Metamorphism" section, this chapter). The demagnetization behavior of the samples at steps below 200°C was complicated because these samples had been heated to 110°C in the physical properties laboratory. Therefore, we have only displayed demagnetization data for temperatures of 200° and greater in Figure 53. The low-field magnetic susceptibility, which was monitored after each thermal demagnetization step, remained relatively unchanged throughout thermal demagnetization, indicating that the magnetic mineralogy of the samples did not change significantly during heating. Samples that had their NRM demagnetized only by thermal methods (solid symbols in Fig. 53) had a distribution of unblocking temperatures between room temperature and 600°C with approximately half of the magnetization unblocked above 550°C. Nearly 25% of the magnetization was unblocked above 575°C, which again suggests an extremely pure magnetite (<5% substitution for Fe cations; Nagata, 1967) as the magnetic carrier. Data for samples that were first subjected to AF demagnetization are plotted as open symbols in Figure 53. These samples had >20% of their original NRM remaining after AF demagnetization; the remaining remanence was then thermally demagnetized. The remanence of these samples had a discrete unblocking temperature range between 525° and 600°C. Such a narrow unblocking temperature distribution suggests that the portion of the remanence resistant to AF demagnetization must be carried

Table 16. Anisotropy of magnetic susceptibility values for the normalized principal susceptibility values and directions.

Core, section, piece	k (10^{-6})	k_{max}	Dec	Inc	k_{int}	Dec	Inc	k_{min}	Dec	Inc	Error	P
147-894F-												
2R-1, 5	16314	1.0730	128	52	1.0327	328	37	0.8943	234	5	±0.0034	1.20
3R-1, 26	3236	1.0224	360	13	0.9990	94	17	0.9786	234	69	±0.0005	1.04
147-894G-												
2R-1, 68	7951	1.0052	357	6	1.0009	111	76	0.9939	266	13	±0.0001	1.01
2R-2, 110	9464	1.0036	269	26	1.0006	27	40	0.9958	155	36	±0.0001	1.01
2R-3, 32	2385	1.0153	105	41	0.9966	351	24	0.9881	240	39	±0.0003	1.03
2R-3, 118	34816	1.0264	18	43	1.0013	174	44	0.9723	276	12	±0.0004	1.06
4R-2, 76	3150	1.0345	96	88	0.9919	253	2	0.9736	343	1	±0.0006	1.06
6R-1, 26	6391	1.0442	75	51	0.9875	280	36	0.9683	181	13	±0.0006	1.08
6R-1, 89	11293	1.0945	249	18	0.9694	347	23	0.9361	125	60	±0.0039	1.17
6R-2, 78	16709	1.0689	228	31	0.9952	36	58	0.9359	135	5	±0.0007	1.14
7R-2, 6	10548	1.0981	269	71	1.0022	94	18	0.8997	4	1	±0.0033	1.22
8R-1, 54	11973	1.0324	186	10	0.9974	73	66	0.9702	280	22	±0.0004	1.06
8R-2, 31	10140	1.0496	325	61	1.0215	97	21	0.9289	195	20	±0.0005	1.13
9R-2, 86	14713	1.0503	116	1	1.0225	206	8	0.9272	16	82	±0.0026	1.13
9R-3, 69	35578	1.0956	112	57	0.9898	208	4	0.9146	301	32	±0.0010	1.20
9R-4, 74	11752	1.0475	182	42	0.9816	68	24	0.9709	317	39	±0.0006	1.08
9R-4, 130	15869	1.0383	149	35	1.0011	242	4	0.9606	338	54	±0.0005	1.08
10R-1, 81	13795	1.0249	230	65	0.9974	325	2	0.9777	56	25	±0.0009	1.05
11R-2, 45	6866	1.0949	129	56	1.0048	283	31	0.9002	20	12	±0.0006	1.22
12R-2, 50	27395	1.1140	164	14	1.0796	297	70	0.8063	70	14	±0.0014	1.38
12R-3, 147	13030	1.0921	137	68	1.0150	24	9	0.8929	290	20	±0.0008	1.22
12R-4, 51	17239	1.0770	360	56	0.9689	242	18	0.9541	142	28	±0.0016	1.13
12R-5, 64	45466	1.0954	210	73	1.0037	34	17	0.9009	304	1	±0.0010	1.22
12R-5, 79	55452	1.1147	101	52	0.9961	328	28	0.8892	225	24	±0.0015	1.25
13R-3, 5	40133	1.1132	288	41	0.9927	136	45	0.8941	31	14	±0.0010	1.25
14R-1, 70	11927	1.0492	268	49	1.0170	160	15	0.9337	58	37	±0.0007	1.12
15R-1, 73	17941	1.0247	61	15	1.0199	302	61	0.9554	158	24	±0.0004	1.07
16W-1, 43	16805	1.1303	339	19	0.9699	239	26	0.8998	102	57	±0.0008	1.26
17R-1, 123	11099	1.0288	174	35	1.0026	269	7	0.9685	10	54	±0.0004	1.06
17R-2, 7	12789	1.0489	239	49	0.9954	125	20	0.9557	21	35	±0.0004	1.10
18R-1, 69	4875	1.0730	212	69	1.0212	349	16	0.9059	83	14	±0.0014	1.18
18R-2, 94	6586	1.0375	195	15	0.9840	348	74	0.9785	104	7	±0.0002	1.06
19R-1, 72	535	1.0102	2	5	1.0069	110	74	0.9829	270	15	±0.0013	1.03
20R-1, 69	12340	1.0421	181	19	0.9911	52	62	0.9668	278	20	±0.0002	1.08
20R-3, 56	21504	1.0329	170	10	1.0015	261	5	0.9656	16	79	±0.0005	1.07

Notes: P is the degree of magnetic anisotropy ($P = k_{max}/k_{min}$). k_{max}, k_{int}, k_{min} normalized to k.

nearly exclusively by single domain (SD) magnetite grains. For equant magnetite grains, this corresponds to a grain size less than 0.05 µm (Day et al., 1977), again consistent with small secondary magnetite grains.

The NRMs were also resistant to AF demagnetization (Fig. 54). For approximately one-third of the samples, more than 20% of the remanent magnetization remained after applying a 100-mT AF field, the maximum field possible with the shipboard demagnetizers. The exceptions to this generalization were a small number of highly altered samples that were magnetically soft (e.g., Sample 147-894G-9R-3, 69–71 cm; Fig. 54). Many of the samples had both soft and hard components (e.g., Samples 147-894G-9R-2, 86–88 cm, and 147-894G-9R-4, 130–132 cm; Fig. 54), suggesting a bimodal distribution in the grain size of magnetite.

A simplified way to estimate the ease of AF demagnetization is to calculate the median destructive field (MDF), which is the AF field required to demagnetize half of the NRM. A histogram of MDF values is plotted in Figure 55. The arithmetic mean of the MDF is 28.6 mT, which is similar to values observed in gabbros from slow-spreading mid-ocean ridges (Kent et al., 1978; Dunlop and Prevot, 1982; Kikawa and Pariso, 1991). The high resistance of the NRM to AF demagnetization requires that most of the remanence be carried by grains that have an effective magnetic grain size less than 10 µm, and a significant portion of the NRM must be carried by SD magnetite (<0.05 µm).

Alternating field demagnetization, to 15 mT, was also performed on the archive half of the whole core. The half cores were also relatively resistant to AF demagnetization; often, more than 50% of the magnetization remained after the 15-mT step. The AF fields were not high enough to isolate the stable magnetization of the half cores.

Direction of Remanent Magnetization

Subsequent to demagnetization, individual components of magnetization were identified for each minicore using a least-squares fitting routine applied to each component of magnetization identified on an orthogonal (Zijderveld) vector diagram (Fig. 56; Zijderveld, 1967). More than half of the samples (17) have two components of magnetization, and four samples have three components of magnetization. A substantial range exists in the direction of the secondary components of magnetization, but the majority have stable inclinations (I_{stable}) that are steep and positive (Fig. 57). This figure also shows that secondary components of magnetization are more common from samples from the upper part of Hole 894G.

Stable magnetic directions were determined for all but four of the samples and are displayed in Table 15. In most cases, the stable component of magnetization was observed to decay to the origin of the Zijderveld diagram. However, for a small number of samples, the stable component of magnetization did not decay to the origin. Stable inclination values for Hole 894G are plotted vs. depth in Figure 58, which shows a general steepening, from 30° to 50°, with depth. The mean I_{stable} value is 40° and is significantly steeper than expected for Site 894. Assuming the remanent magnetization was acquired in a geocentric axial dipole field, the predicted magnetic inclination for crust formed at this latitude (~2°N) should be very close to 0°. Up to 13° of angular dispersion can be expected in inclination values during the past 5 Ma for this latitude due to secular variation (i.e., normal variations in the Earth's magnetic field) (McFadden and Merrill, 1975). Measurements of the tilt of the borehole show that at a depth of 70 mbsf, Hole 894G is inclined only 4°–6° from vertical (see "Operations" section, this chapter). Therefore, it is unlikely that either

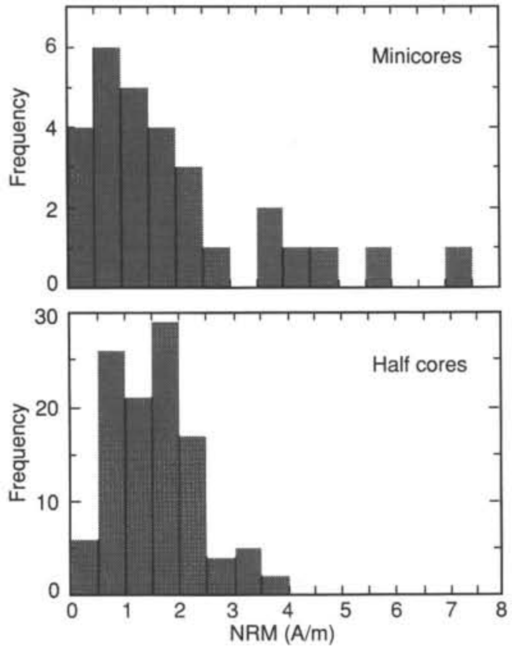

Figure 49. Histograms of the intensity of NRM.

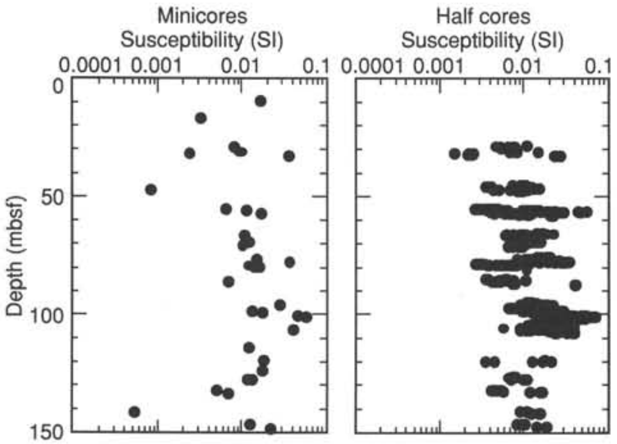

Figure 50. Plots of magnetic susceptibility vs. depth in Hole 894G minicores and half core samples.

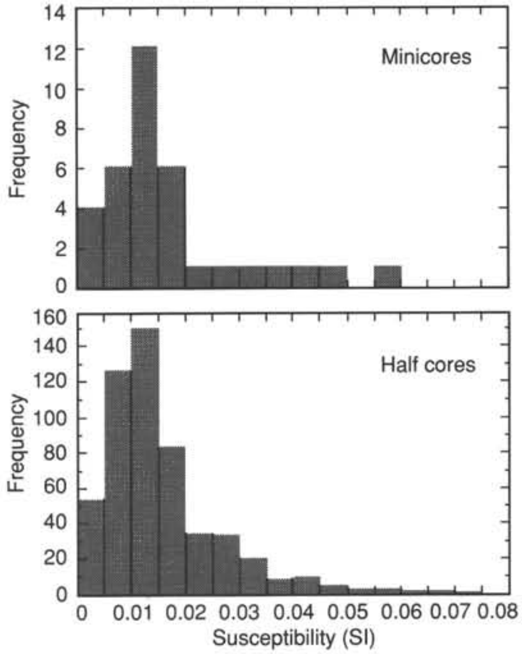

Figure 51. Histograms of magnetic susceptibility.

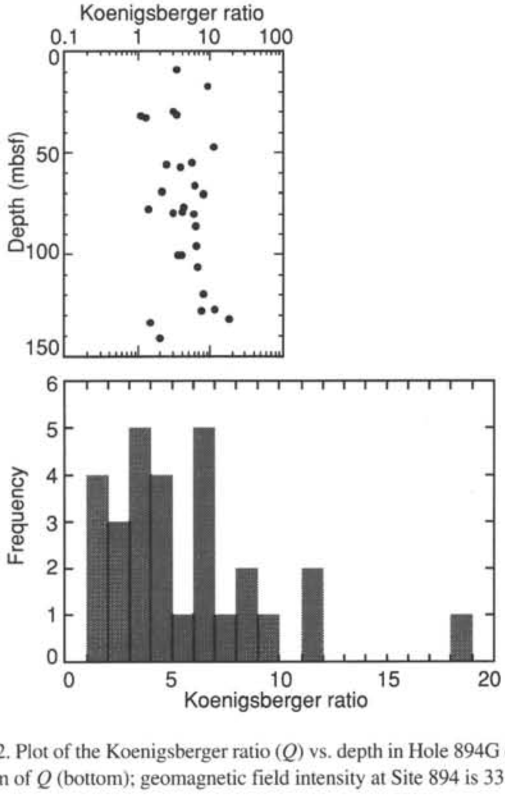

Figure 52. Plot of the Koenigsberger ratio (Q) vs. depth in Hole 894G (top) and histogram of Q (bottom); geomagnetic field intensity at Site 894 is 33×10^{-6}.

secular variation or tilt of the borehole is responsible for the steep observed I_{stable} values, although the latter mechanism may contribute to the steepening of I_{stable} values with depth. A more reasonable model is that the crustal section sampled at Hole 894G acquired its remanent magnetization parallel to the Earth's magnetic field (i.e., with an inclination near zero) shortly after emplacement at the East Pacific Rise. Subsequently, the crustal section experienced significant tectonic rotation, of up to 40°, about a horizontal axis. Because ODP drill core is not azimuthally oriented, we were not able to constrain tectonic rotation that may have occurred about a vertical axis.

The lack of azimuthal orientation also prevented us from using magnetic declination to distinguish whether this section is normal or reversely magnetized. Additionally, the lack of well-defined magnetic anomalies over Hess Deep prohibits inference of the polarity of the magnetization at this site (i.e., normal or reversed) from the magnetic field observed at sea surface. However, if we assume that the crustal section sampled at Site 894 was originally formed at the EPR and experienced normal seafloor spreading, the magnetic anomalies observed both to the north and south of Hess Deep would constrain the age of this section to approximately 1 Ma (Lonsdale, 1988). If this is true, and the NRM was acquired near the ridge axis, the in-situ magnetization should be reversed (pointing to the south).

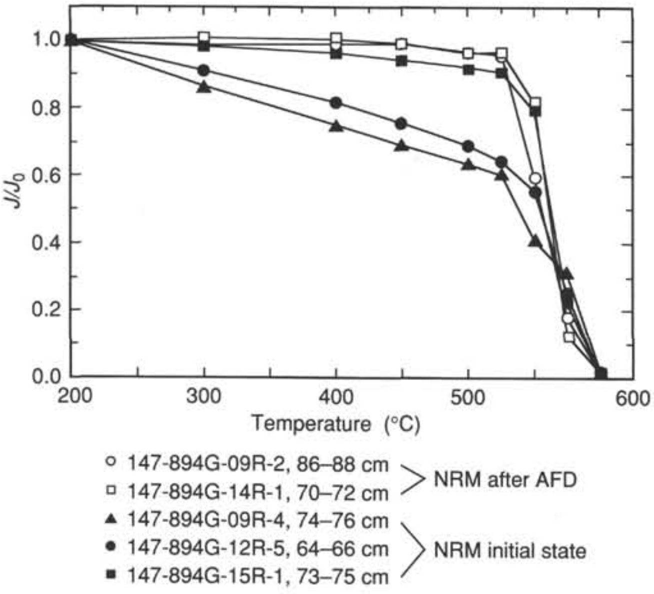

Figure 53. Thermal demagnetization curves of representative samples with either initial NRMs (solid symbols) or remanence remaining after AFD to 100 mT (open symbols). J is the remaining magnetization, and J_0 is the original NRM (or remanence after AFD to 100 mT). The decrease in magnetization between 550° and 600°C suggests that relatively pure magnetite is the dominant magnetic carrier.

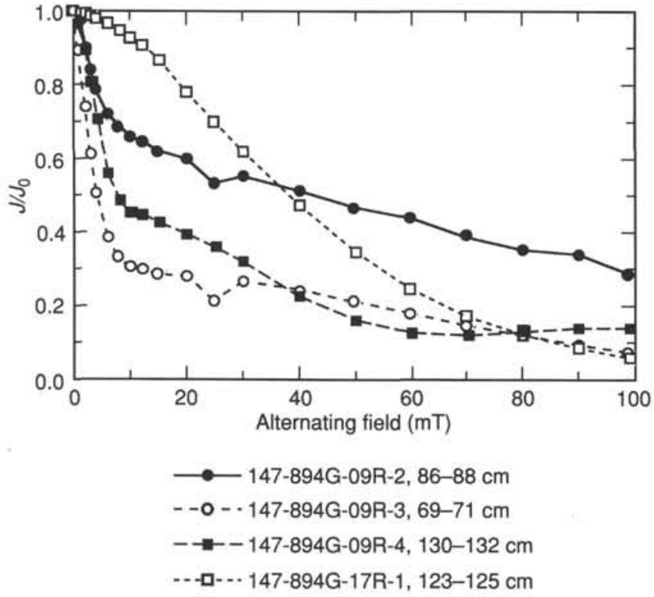

Figure 54. AFD curves of NRM representing the different characteristic behaviors observed in samples from Hole 894G. All samples are gabbronorites, with Sample 147-894G-9R-3, 69–71 cm, more altered than the others. Many samples had AFD curves similar to Sample 147-894G-9R-2, 86–88 cm, where a significant portion of the NRM remained after an AF of 100 mT.

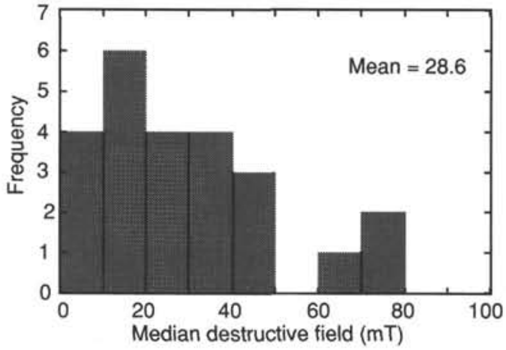

Figure 55. Histogram of the median destructive field (MDF) for all samples for which it could be calculated. The mean MDF of 28.6 mT confirms the general observation from Figure 53 that the samples are relatively resistant to AFD.

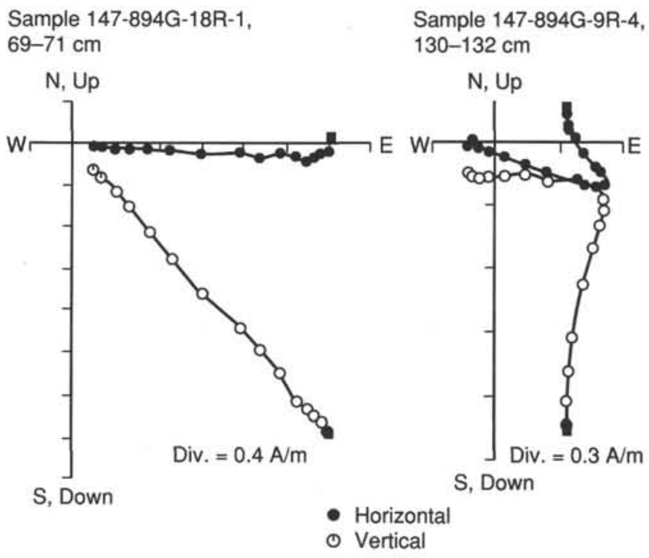

Figure 56. Zijderveld plots for two samples from Hole 894G. Sample 147-894G-18R-1, 69–71 cm (left) is typical of many 894G gabbroic rocks because it has one component of remanent magnetization that decays to the origin during progressive demagnetization. Sample 147-894G-9R-4, 130–132 cm (right) has two components of remanent magnetization, and the last component does not decay to the origin.

Magnetic Fabric

In weak magnetic fields (0.1–0.5 mT), the intensity of the induced magnetization (J_i) of a rock is a linear function of the intensity of the applied external field (H):

$$J_i = k_{ij}H_j,$$

where the dimensionless proportionality factor k_{ij} is a second-rank tensor and referred to as the magnetic susceptibility tensor (anisotropy of magnetic susceptibility [AMS], e.g., Hrouda, 1982) and used as a representation of the magnetic fabric. The eigenvalues of k_{ij} are the principal susceptibilities ($k_{max} \geq k_{int} \geq k_{min}$) and the eigenvectors are the principal directions. The tensor is graphically represented by an ellipsoid. The AMS of a mineral aggregate is the result of the magnetic anisotropy effects of all phases and particles present. AMS is, therefore, a function of the mineral composition (Borradaile et al., 1987), grain shape (Uyeda et al. 1963), and mineral preferred orientation. AMS measures grain shape if dominated by magnetite, and crystallographic preferred orientations if not dominated by magnetite. The magnetic fabric is related to deformational, sedimentary, or magmatic features, and their directions and magnitudes (see reviews by Hrouda, 1982, and Borradaile, 1988).

Low temperature magnetic susceptibility measurements were done on minicore Samples 147-894G-2R-3, 118–120 cm, and 147-894G-6R-1, 26–28 cm (Fig. 59). The low temperature curves of both

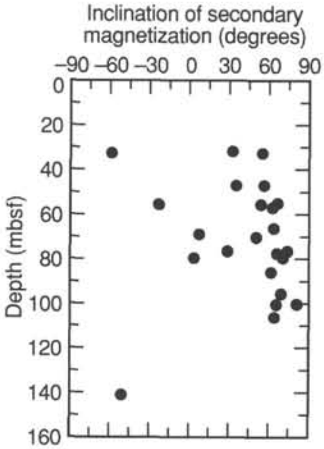

Figure 57. Inclination values of secondary components of magnetization are plotted vs. depth for Hole 894G and show that, in general, the secondary components are steep and positive. In addition, secondary components of magnetization are more often observed in the upper part of the hole than in the lower part.

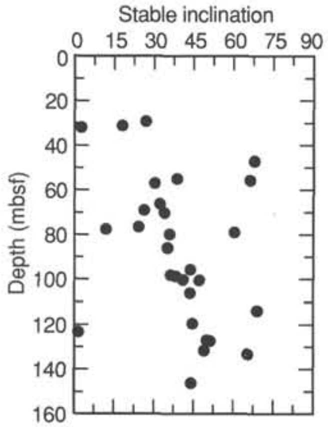

Figure 58. Stable magnetic inclination plotted vs. depth for Hole 894G. The inclination values appear to steepen with depth in the hole.

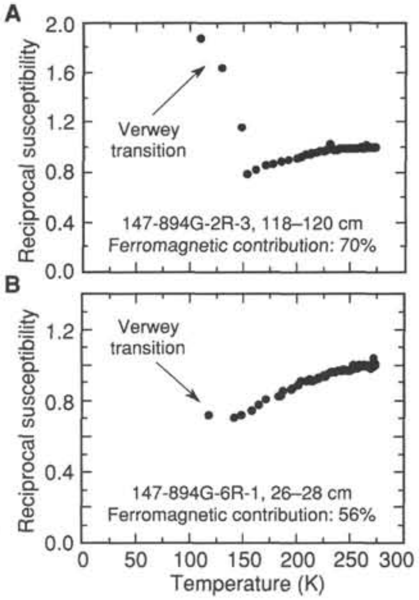

Figure 59. Temperature dependence of the magnetic susceptibility (118–273 K). The Verwey transition (120–130 K) is a characteristic lattice transition of magnetite. The reciprocal susceptibility curves are used to quantify the relative contribution of the paramagnetic and the ferromagnetic susceptibility. The ferromagnetic (magnetite) contribution dominates for both samples.

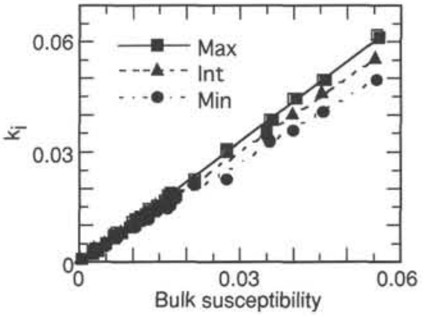

Figure 60. Plot of the principal susceptibility axes vs. the bulk susceptibility shows that the regression lines meet in the origin of the diagram.

specimens have a slightly bent, convex shape typical for a contribution of both paramagnetic and ferromagnetic minerals. The susceptibility jump at approximately 118 K, which occurs in both samples, is caused by a lattice transition in magnetite (the Verwey transition, in which magnetite changes from being orthorhombic to cubic; Verwey and Haayman, 1941). The quantitative analysis of the two curves shows that this magnetite contributes 70% of the susceptibility of Sample 147-894G-2R-3, 118–120 cm, and 56% of the susceptibility of Sample 147-894G-6R-1, 26–28 cm, which has a considerably lower bulk susceptibility. The remaining contribution to the magnetic susceptibility, and hence the AMS, is likely due to paramagnetic minerals such as ilmenite, olivine, and pyroxene.

The AMS results of the minicores of Holes 894F and 894G are summarized in Table 16. The specimens have a well-defined anisotropy ellipsoid with a degree of anisotropy ($P = k_{max}/k_{min}$) ranging from 1.01 to 1.38, with a mean value of 1.12 and a standard deviation of 0.09. The degree of anisotropy, P, is not related to the bulk susceptibility (Table 16) and, hence, is not a function of the rock composition. A plot of the principal susceptibilities (k_{max}, k_{int}, k_{min}) vs. the bulk susceptibility (Fig. 60) shows that regression lines through the individual axes meet in the origin of the diagram. This suggests a simple mixture of paramagnetic and ferromagnetic minerals (Henry and Daly, 1983) in which the bulk susceptibility is a function of the relative concentration of both phases. The anisotropy is caused by the shape and orientation of magnetite grains and the crystallographic orientation of the paramagnetic minerals (olivine, pyroxene, and ilmenite). The susceptibility ellipsoids of all specimens are represented in two-dimensional space in a Flinn-type diagram (Fig. 61). The shape of the ellipsoids varies from nearly spherical, close to the origin of the Flinn diagram (Samples 147-894G-2R-1, 68–70 cm, and 147-894G-2R-2, 110–112 cm), to oblate (e.g., Samples 147-894G-12R-2, 50–60 cm, and 147-894G-18R-1, 69–71 cm) and prolate (e.g., Samples 147-894G-6R-1, 89–91 cm, and 147-894G-16W-1, 43–45 cm). Most ellipsoids, however, are triaxial. The triaxial to prolate shapes indicate the predominance of linear over planar petrofabrics. Figure 62 shows the variation of the degree of anisotropy as a function of depth below seafloor (Holes 894F and 895G). The plagioclase-olivine phyric basalt at 30 mbsf (Samples 147-894G-2R-1, 68–70 cm, and 147-894G-2R-2, 110–112 cm) suggests an isotropic petrofabric in contrast to the more anisotropic gabbronorites. Based on variations of the degree of anisotropy, three different intervals can be distinguished downhole (Fig. 62). Samples above 60 mbsf and below 130

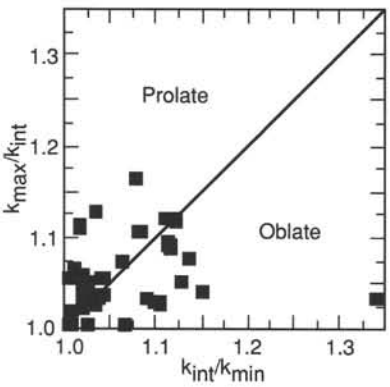

Figure 61. Flinn-type diagram of the AMS ellipsoid shapes of all specimens. Although the shape scatters between spherical, oblate, and prolate forms, most ellipsoids are triaxial, suggesting a predominantly linear petrofabric.

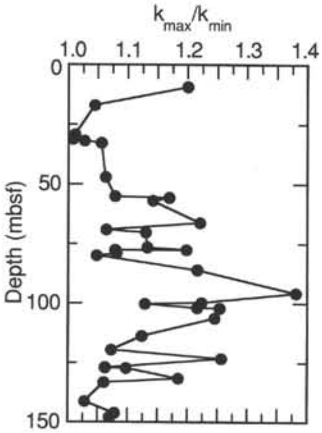

Figure 62. Degree of anisotropy ($P = k_{max}/k_{min}$) plotted as a function of depth. Anisotropy is high for samples recovered between 60 mbsf and 130 mbsf.

mbsf have very low anisotropies, and samples between 60 and 130 mbsf have high anisotropies.

The principal susceptibility directions are presented in lower hemisphere equal area stereograms in Figure 63, which also shows the orientation of the maximum and the minimum axes for samples with a stable paleomagnetic direction. The data are rotated under the assumption that the stable direction pointed to the south. Corrections for the inclination of the stable direction were not performed. The maximum susceptibility axis is defined by the overall orientation of the long axis of magnetite, the dominant contributor to AMS. The plunge of the maximum axes has a mean of 38°. A histogram of the plunge of the minimum axes (Fig. 64) shows that most axes are shallow, with a peak in frequency around 20°. The magnetic foliations (i.e., the planes of k_{min} and k_{int}) of all oblate ellipsoids are plotted in Figure 63 as great circles. The foliations are generally steeply dipping with a variable strike. The orientation of the magnetic lineation (k_{max}) in the foliation is intermediate to steep. The principal directions of the almost isotropic plagioclase-olivine phyric basalt show a steeply dipping, east–west striking magnetic foliation and shallow plunging maximum axes (Table 16). The scatter of the directional data likely results from error in the correction of the drilling-induced rotation of the core and from poorly defined axial orientations of weakly anisotropic samples.

The following generalizations can be made regarding the magnetic fabric:

1. The magnetic fabric results from the combination of the overall shape of magnetite and the preferred lattice orientation of paramagnetic ilmenite, pyroxene, and olivine.

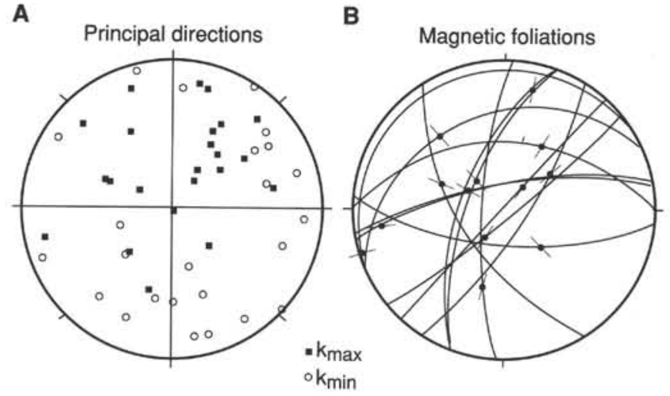

Figure 63. Orientation of the principal susceptibility directions in lower hemisphere equal area stereograms rotated under the assumption that the stable paleomagnetic direction points to the south. **A.** Maximum axes have an intermediate to steep plunge (mean value = 38°); minimum axes are shallow. **B.** The magnetic foliations ($k_{max} - k_{int}$) planes of the oblate ellipsoids; circles are magnetic lineations (k_{max}).

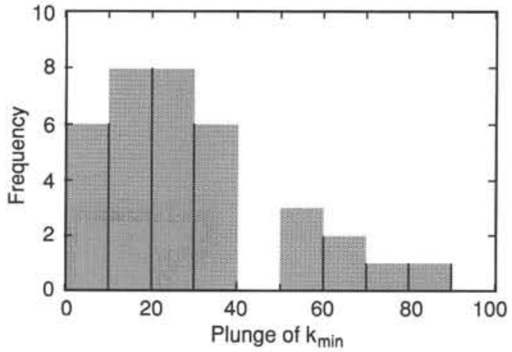

Figure 64. Histogram of the distribution of the plunge of k_{min}. Most samples have a fairly shallow plunging k_{min}.

2. The AMS ellipsoid shape is triaxial, mostly prolate, indicating a linear magmatic fabric. The anisotropy increases downhole to about 130 mbsf and is weak below that depth.

3. The orientation of the magnetic foliation is, where developed, steep (k_{min} has a shallow plunge), and the orientation of the lineation (k_{max}) is intermediate to steep.

Summary

Paleomagnetic measurements show that the average intensity of natural remanent magnetization and magnetic susceptibility of samples from Hole 894G are 2.0 A/m and 0.016, respectively. The ratio of these two parameters suggests that the in-situ magnetization of this crustal section is dominated by remanent magnetization, rather than instantaneous magnetization induced by the Earth's field. Overall, these magnetic properties are similar to those observed for previously studied oceanic gabbros (which have primarily been recovered from slow-spreading ridges) and also to those observed on most oceanic basalts. The remanent magnetization is very stable with respect to both alternating field and thermal demagnetization. The thermal demagnetization data indicate that magnetite is the carrier of remanence. The stable direction of magnetization dips downward at an average of 40° and is significantly different from the value expected for crust formed at this latitude (0°). Therefore, it seems likely that this crustal section experienced substantial tectonic rotation.

Low temperature susceptibility measurements indicate that magnetite dominates the magnetic susceptibility values, and a significant contribution is present due to paramagnetic minerals such as olivine, pyroxene, and ilmenite. The magnetic anisotropy increases downhole to about 130 mbsf and is weak below that depth.

PHYSICAL PROPERTIES

The physical properties of crystalline rocks exhumed from depth and measured at atmospheric pressures characteristically bear a significant overprint from both original porosity (O'Connell and Budianski, 1974; Toksöz et al., 1976) and secondary porosity brought on by stress unloading and coring processes. Matrix alteration and infilling of fractures and voids by secondary phases can also make a significant contribution to physical property measurements (Moos and Zoback, 1983). Bearing these factors in mind, the following section represents an attempt to interpret the physical property measurements from Site 894 as a function of lithologic type and degree of alteration for lower oceanic rocks from Hess Deep. Experimental procedures are given in the "Physical Properties" section of the "Explanatory Notes" chapter, this volume.

Index Properties

Measurements for index properties were performed on 40 samples from Site 894. Sample weights and volumes in both saturated and dry states were used to calculate bulk density, grain density, porosity, and water content. A salt correction assuming 3.5% interstitial fluid salinity was applied (Hamilton, 1971). Results are given in Table 17.

The average wet-bulk density of the samples recovered from Site 894 is 2.92 g/cm^3 with a standard deviation of 0.09 g/cm^3. The low mean value and large standard deviation correlate with a wide range of compositions found at this particular site. Samples with thin sections show that the low densities correspond to the most altered samples (e.g., Sample 147-894G-2R-3, 32–35 cm), whereas the olivine-bearing rocks have more typical values of Layer 3 rocks (e.g., Sample 147-894G-2R-3, 118–120 cm). Porosity values have a mean value of 1.19% with a median of 0.43%, whereas the water content mean value is 0.43% with a median of 0.15%. The significant range in porosity and water content values corresponds to the amount of alteration, with the most altered rocks having the highest porosity values.

Bulk-density-porosity systematics for the rocks from Site 894 show two significant trends (Fig. 65). One trend exhibits a decrease in bulk density with an increase in porosity, suggesting that many of the altered samples are heavily fractured. The second trend shows a set of low-density samples with low porosity values, implying that the alteration may have infilled any pre-existing porosity. Variations in density with depth for minicore data (Fig. 66) show discrete alteration zones that for the most part correlate well with high porosity values.

Both continuous and 2-min discrete gamma-ray attenuation porosity evaluator (GRAPE) density measurements were collected on the core from Hole 894G. Analysis of the continuous data showed it to be unsuitable for inclusion in this report because of a large scatter in the data and a lack of a correlation to the minicore results. The lack of correlation to the minicore results can be understood by examining the sensitivity to sample thickness in the equation used to convert GRAPE counts to bulk density. A 1-mm change in sample thickness, from 56 to 55 mm, will result in an apparent density change from 2.81 g/cm^3 to 2.86 g/cm^3 in a typical sample. The core normally has diameter changes of 2 mm for continuous core and commonly has much greater sample thickness variability when the core is fractured or broken. The scatter in the data is thought to be considerably increased by the short counting times used when the core is measured continuously relative to the 2-min count time used with the discrete measurements.

The 2-min discrete GRAPE measurements appear to be a useful method of supplementing the minicore density measurements after comparison and calibration of the GRAPE data with minicore densities. The data set from Hole 894G includes 13 discrete GRAPE measurements that have minicore density measurements within 5 cm.

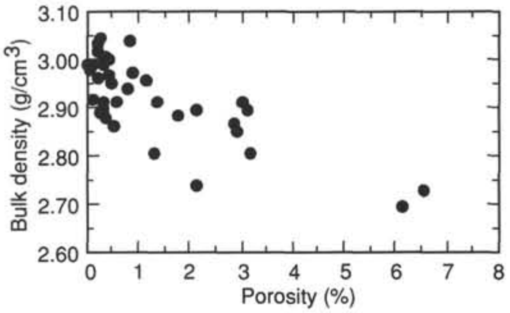

Figure 65. Density-porosity relationships for the crystalline rocks from Site 894. The mean density value for these samples is 2.922 g/cm^3, whereas the porosity values have a mean of 1.19%.

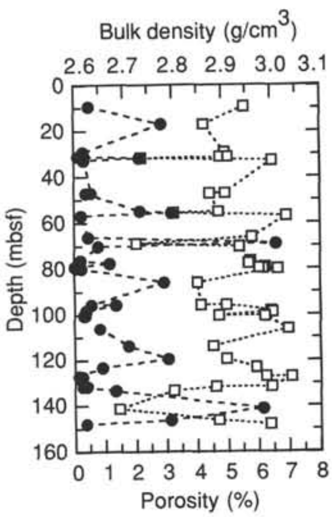

Figure 66. Density (squares) and porosity (filled circles) values as a function of depth for minicore data from Hole 894G.

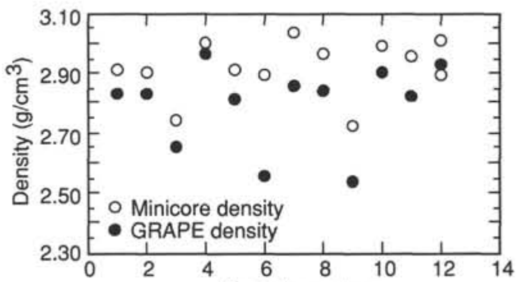

Figure 67. GRAPE density evaluation diagram showing a comparison with minicore bulk density data for similar depth intervals.

A correlation is seen between the GRAPE and minicore bulk densities (Fig. 67), although a shift is observed between the two. This shift is thought to be caused by the beam striking the core slightly above the median line for which the diameter measurement is made. The quartz and air calibrations (discussed in the "Explanatory Notes" chapter, this volume) were very consistent throughout, giving a Compton attenuation coefficient (Qtz_{μ}) of 0.07834. The quartz calibration sample thickness of 50.15 mm is considered sufficiently close to the 55-mm typical core thickness, such that no sample diameter correction is needed. The minicore wet-bulk densities are higher by an

Table 17. Index properties of the crystalline rocks recovered from Site 894.

Core, section, interval (cm)	Piece number	Depth (mbsf)	Bulk density (g/cm^3)	Grain density (g/cm^3)	Porosity (%)	Water content (%)	Comments
147-894F-							
2R-1, 5–7	1	9.35	2.946	2.956	0.50	0.18	Gabbro (60% altered)
3R-1, 27–29	5	17.06	2.865	2.921	2.87	1.02	Olivine gabbro (55% altered)
147-894G-							
2R-1, 68–71	9	29.28	2.907	2.913	0.30	0.11	Plagioclase-olivine-phyric basalt
2R-2, 105–109	15	31.15	2.897	2.904	0.34	0.12	Plagioclase-olivine-phyric basalt
2R-2, 110–113	15	31.20	2.913	2.915	0.14	0.05	Plagioclase-olivine-phyric basalt
2R-3, 32–35	5	31.87	2.737	2.775	2.14	0.80	Olivine gabbro (70% altered)
2R-3, 118–121	14	32.73	3.003	3.009	0.32	0.11	Olivine gabbro (40% altered)
4R-2, 71–75	10	47.05	2.908	2.919	0.57	0.20	Gabbronorite (20% altered)
4R-2, 76–78	10	47.10	2.876	2.884	0.39	0.14	Gabbronorite (20% altered)
6R-1, 26–28	4A	55.06	2.894	2.936	2.16	0.77	Gabbronorite (35% altered)
6R-1, 89–91	8A	55.69	2.803	2.863	3.19	1.17	Gabbronorite (30% altered)
6R-2, 78–80	6	57.01	3.032	3.037	0.23	0.08	Gabbronorite (20% altered)
7R-2, 6–8	1	66.26	2.962	2.971	0.45	0.16	Gabbronorite (25% altered)
8R-1, 54–57	5A	69.04	2.726	2.849	6.57	2.47	Gabbronorite (85% altered)
8R-2, 31–33	4	70.31	2.936	2.952	0.78	0.27	Gabbronorite (20% altered)
9R-2, 86–88	5A	76.51	2.959	2.963	0.21	0.07	Gabbronorite (35% altered)
9R-3, 69–71	5C	77.60	2.956	2.980	1.17	0.41	Gabbronorite (35% altered)
9R-4, 74–76	6	79.07	2.989	2.990	0.03	0.01	Olivine gabbronorite (30% altered)
9R-4, 123–127	11	79.56	2.984	2.986	0.09	0.03	Olivine gabbronorite (30% altered)
9R-4, 130–132	11	79.63	2.976	2.978	0.09	0.03	Olivine gabbronorite (30% altered)
10R-1, 81–83	13A	79.91	3.014	3.019	0.24	0.08	Gabbro (15% altered)
11R-2, 45–47	5	86.01	2.850	2.906	2.93	1.06	Gabbronorite (50% altered)
12R-2, 46–50	4E	95.72	2.857	2.868	0.55	0.20	Gabbronorite (50% altered)
12R-2, 50–52	4E	95.76	2.909	2.936	1.35	0.48	Gabbronorite (50% altered)
12R-3, 147–149	8B	98.20	3.000	3.007	0.38	0.13	Gabbronorite (30% altered)
12R-4, 51–53	4C	98.74	3.003	3.011	0.38	0.13	Gabbronorite (20% altered)
12R-5, 64–66	7D	100.37	2.894	2.900	0.30	0.11	Gabbronorite (20% altered)
12R-5, 79–81	9	100.52	2.987	2.993	0.34	0.12	Gabbronorite (20% altered)
13R-3, 5–7	1A	106.28	3.035	3.053	0.84	0.29	Gabbronorite (30% altered)
14R-1, 70–72	11	113.80	2.882	2.916	1.77	0.63	Gabbronorite (50% altered)
15R-1, 73–75	12	119.53	2.909	2.970	3.05	1.07	Gabbronorite (50% altered)
16W-1, 43–45	7	123.23	2.969	2.987	0.91	0.31	Gabbronorite (60% altered)
17R-1, 123–125	14	127.03	2.989	2.991	0.13	0.05	Gabbronorite (25% altered)
17R-2, 7–9	1A	127.31	3.041	3.046	0.25	0.09	Gabbronorite (35% altered)
18R-1, 69–71	10A	131.59	3.000	3.008	0.41	0.14	Gabbronorite (20% altered)
18R-1, 72–76	10A	131.62	2.887	2.892	0.26	0.09	Gabbronorite
18R-2, 94–96	14	133.26	2.805	2.829	1.33	0.49	Gabbronorite (75% altered)
19R-1, 72–74	12	141.22	2.691	2.803	6.14	2.34	Moderately olivine-plagioclase phyric basalt
20R-1, 60–62	10	146.20	2.893	2.955	3.13	1.11	Gabbronorite (40% altered)
20R-3, 56–58	9	147.98	2.998	3.006	0.37	0.13	Gabbronorite (60% altered)
			2.922	2.945	1.191	0.431	Mean
			0.085	0.066	1.540	0.575	Standard deviation

Note: Alteration percentages were obtained from visual core descriptions.

average of 0.11 g/cm^3 or a median shift of 0.09 g/cm^3. The GRAPE densities in Table 18 have been corrected with a shift of 0.10 g/cm^3.

Compressional-wave Velocities

During sampling, care was taken to avoid major veins and fractures to determine the effect of mineral composition on compressional-wave velocities (V_p); in some instances this proved to be a difficult task because of the abundance of microfractures and veins throughout the core. Minicore samples were cut horizontally and vertically with respect to the drilled core (see Fig. 20, "Paleomagnetism" section, "Explanatory Notes" chapter, this volume) to examine the effects of mineral properties and proportions, porosity (especially fracture porosity), and rock textures on seismic velocities. Also, V_p can vary with direction in rocks that are layered or that have preferred mineral as well as microfracture orientations.

Compressional-wave velocities were measured at atmospheric pressures and temperatures, in both horizontally and vertically oriented, water-saturated samples. The horizontal minicores have a mean velocity of 6587 m/s with a standard deviation of 564 m/s and values ranging from 5330 m/s to 7335 m/s (Table 19). V_p measurements indicate that seismic velocities decrease with increasing porosity values for the gabbroic rocks of Hole 894G (Fig. 68). This trend is consistent with the correlation observed between atmospheric pressure velocities and porosity measurements obtained on similar samples during Leg 118 (Robinson, Von Herzen, et al., 1989).

As is the case of all shallow oceanic drill holes, fracture porosity is thought to be a major factor influencing the velocity structure of Hole 894G. Throughout the core a large population of 40° to 60° dipping fractures and veins pre-dates a smaller set of nearly vertical fractures and veins. The latter set may have developed because of the unloading of stresses during the uplift of the intrarift ridge. Large variations in V_p with depth (Fig. 69) correlate with fluctuations in porosity as well as changes in bulk densities. Additional post-cruise studies of velocity as a function of confining pressure will reduce the effect of open fractures and will give better estimates of in-situ velocities.

Velocity-bulk density systematics for the cores from Site 894 show low V_p values correlating with low density measurements (Fig. 70). Low velocities correspond to low density values within the most altered zones, whereas the higher velocity values are representative of the least altered rocks. Study of thin sections revealed that chlorite and perhaps secondary plagioclase are the main low-density mineral assemblages that may be causing these variations, whereas the high-density and high-velocity mineral assemblages are olivine, clinopyroxene, and amphiboles (after Christensen, 1982). Further correlation of mineral assemblages with physical properties was mainly limited by the availability of thin-section modal analyses for all the physical properties samples. In later studies, modal analyses for all of the

Table 18. Minicore bulk density and 2-min GRAPE data obtained for rocks drilled in Hole 894G.

Core, section, interval (cm)	Depth (mbsf)	GRAPE density (g/cm^3)	Bulk density (g/cm^3)
147-894G-			
2R-1, 66–68	29.26	2.832	2.907
2R-2, 38–40	30.48	2.794	
2R-2, 105–107	31.15	2.826	2.897
2R-3, 36–38	31.91	2.652	2.737
2R-3, 115–117	32.70	2.963	3.002
4R-1, 56–58	45.40	2.760	
4R-1, 116–118	46.00	2.870	
4R-2, 55–57	46.89	2.890	
4R-2, 71–73	47.05	2.816	2.908
6R-1, 23–25	55.03	2.555	2.894
6R-1, 114–116	55.94	2.557	
6R-2, 12–14	56.35	2.717	
6R-2, 78–80	57.01	2.857	3.032
7R-1, 93–95	65.63	2.690	
7R-2, 9–11	66.29	2.841	2.962
8R-1, 52–54	69.02	2.540	2.726
8R-2, 102–104	71.02	2.806	
9R-1, 114–116	75.29	2.806	
9R-2, 10–12	75.75	2.709	
9R-2, 116–118	76.81	2.722	
9R-3, 7–9	76.98	2.657	
12R-1, 103–105	94.79	2.764	
12R-2, 111–113	96.37	2.780	
12R-3, 66–68	97.39	2.901	
12R-5, 82–84	100.55	2.901	2.987
13R-1, 111–113	104.34	2.877	
13R-2, 67–69	105.40	2.883	
13R-3, 44–46	106.67	2.883	
13R-3, 128–130	107.51	2.964	
15R-1, 75–77	119.55	2.819	
18R-1, 72–74	131.62	2.924	
18R-1, 5–7	130.95	2.920	
18R-2, 95–97	133.25	2.736	

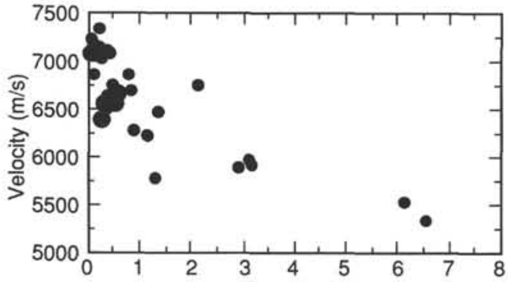

Figure 68. Velocity-porosity relationship for the crystalline rocks from Hole 894G.

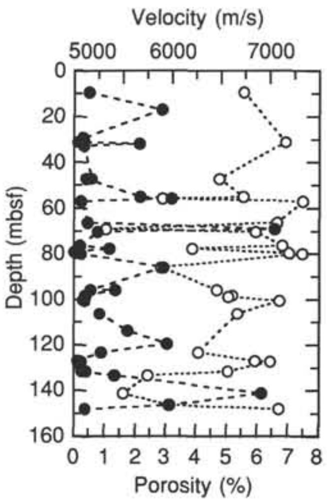

Figure 69. Velocity (open circles) and porosity (filled circles) values as a function of depth for the crystalline rocks from Hole 894G.

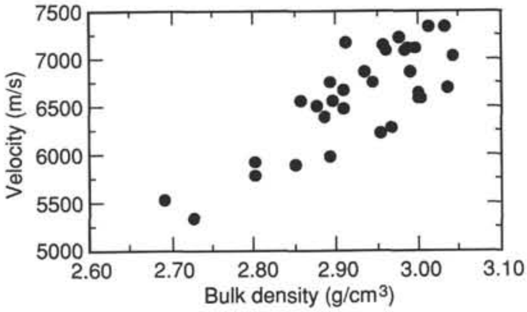

Figure 70. Velocity-density systematics for the crystalline rocks from Hole 894G.

physical properties samples will provide more useful information in the interpretation of velocity and index property data.

Velocities measured in several vertical and horizontal samples do not show any significant anisotropy (Table 19). The differences observed in directional velocities are mostly due to significant variations in densities and perhaps the presence of oriented microcracks caused by the release of in-situ stresses. At low confining pressures, oriented microfractures can generate large degrees of anisotropy or can interfere with anisotropic properties from preferred mineral orientation (Birch and Bancroft, 1940; Birch, 1960, 1961; Hyndman and Drury, 1976; Iturrino et al., 1991). Therefore, the directional velocity variations will be difficult to analyze until additional data is collected.

Thermal Conductivity

Core samples from Hole 894G were measured nondestructively for thermal conductivity in the shipboard laboratory using a needle probe placed between the sample and a slab of low-conducting material as described in the "Explanatory Notes" chapter (this volume). The data were carefully edited to remove the early nonlinear transient heating component, and only the linear portions of the temperature vs. ln time relationships were used. The variability of this time range between measurements probably indicates differences in the details of placing the sample in the apparatus, with consequent variability in boundary conditions near the needle probe. Geometrical differences and variations in thickness of the edges close to the base and the tip of the needle probe also may have contributed to some of the observed variations.

The average thermal conductivity of the samples from Hole 894G is 2.22 W/m°C with a standard deviation of 0.18 W/m°C (Table 20). Measurements on three fine-grained dikes have an average value of 1.78 W/m°C with a standard deviation of 0.11 W/m°C. The gabbroic samples have a mean thermal conductivity of 2.26 W/m°C and a standard deviation of 0.11 W/m°C. These values are within the variability of previously reported gabbroic samples (Clark, 1966; Robinson, Von Herzen, et al., 1989). Separating the samples by compositional variations, the mean for highly altered gabbronorite samples is 2.19 W/m°C with a standard deviation of 0.09 W/m°C, whereas the mean value for the least altered gabbronorites is 2.35 W/m°C with a standard deviation of 0.04 W/m°C.

The variability in the results is significantly greater than the experimental uncertainty, which reflects real differences in conductivity due to variations in density and the degree of alteration. A general systematic correlation between density and thermal conductivity has been previously suggested for oceanic rocks with basaltic compositions (Robertson and Peck, 1974; Hyndman et al., 1984).

Table 19. Directional compressional-wave velocity and resistivity measurements of the crystalline rocks from Site 894.

Core, section, interval (cm)	Piece number	Depth (mbsf)	Velocity(h) (m/s)	Velocity(v) (m/s)	Resistivity (ohm-m)	Comments
147-894F-						
2R-1, 5–7	1	9.35	6734			Gabbro
147-894G-						
2R-2, 105–109	15	31.15		6536		Plagioclase-olivine phyric basalt
2R-2, 110–113	15	31.20	7161			Plagioclase-olivine phyric basalt
4R-2, 71–75	10	47.05		6643		Gabbronorite
4R-2, 76–78	10	47.10	6485		501.61	Gabbronorite
6R-1, 26–28	4A	55.06	6732			Gabbronorite
6R-1, 89–91	8A	55.69	5903		51.15	Gabbronorite
6R-2, 78–80	6	57.01	7335		701.97	Gabbronorite
7R-2, 6–8	1	66.26	7076		718.59	Gabbronorite
8R-1, 54–57	5A	69.04	5330		19.80	Gabbronorite
8R-2, 31–33	4	70.31	6858		309.07	Gabbronorite
9R-2, 86–88	5A	76.51	7120			Gabbronorite
9R-3, 69–71	5C	77.60	6214		290.05	Gabbronorite
9R-4, 123–127	11	79.56		7071		Olivine gabbronorite
9R-4, 130–132	11	79.63	7200		10747.49	Olivine gabbronorite
10R-1, 81–83	13A	79.91	7334		1056.18	Gabbro
11R-2, 45–47	5	86.01	5889		64.58	Gabbronorite
12R-2, 46–50	4E	95.72		6556		Gabbronorite
12R-2, 50–52	4E	95.76	6465		283.11	Gabbronorite
12R-3, 147–149	8B	98.20	6621		953.03	Gabbronorite
12R-4, 51–53	4C	98.74	6578			Gabbronorite
12R-5, 79–81	9	100.52	7098		880.50	Gabbronorite
13R-3, 5–7	1A	106.28	6671		405.36	Gabbronorite
16W-1, 43–45	7	123.23	6278		441.70	Gabbronorite
17R-1, 123–125	14	127.03	6855		3284.43	Gabbronorite
17R-2, 7–9	1A	127.31	7008		1982.55	Gabbronorite
18R-1, 69–71	10A	131.59	6576		1109.38	Gabbronorite
18R-1, 72–76	10A	131.62		6390		Gabbronorite
18R-2, 94–96	14	133.26	5757		222.98	Gabbronorite
19R-1, 72–74	12	141.22	5504			Moderately olivine-plagioclase phyric basalt
20R-1, 60–62	10	146.20	5969		131.48	Gabbronorite
20R-3, 56–58	9	147.98	7093		1729.44	Gabbronorite

Notes: Velocity(h) = horizontal samples; Velocity(v) = vertical samples.

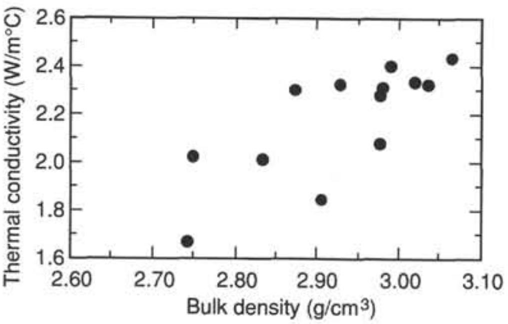

Figure 71. Thermal conductivity-grain density systematics for samples with minicore density information.

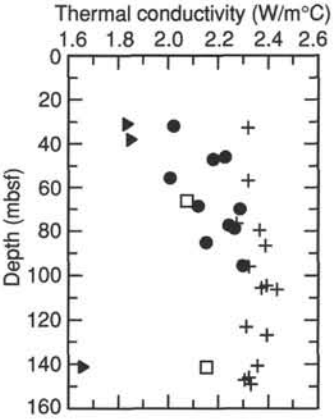

Figure 72. Thermal conductivity as a function of depth for samples from Hole 894G. Plus signs = relatively fresh gabbronorites, circles = altered gabbronorites, triangles = fine-grained dikes, squares = a fractured and relatively fresh gabbronorite sample and a coarse-grained sample with well-defined magmatic foliation.

During Leg 147, density values obtained from minicore samples on the same pieces that were used for conductivity measurements tend to show a similar relationship between the two parameters (Fig. 71). In this case, the decrease in thermal conductivity with a decrease in density can be attributed to the degree of alteration and perhaps to the amount of fresh olivine present in the rocks, although the latter has not been confirmed. Overall, the thermal conductivity at this site increases with depth to approximately 80 mbsf (Fig. 72).

Figure 72 also shows two relatively fresh samples with lower conductivity values than the unaltered samples (Table 20). One of the samples has a series of fractures, whereas the second sample shows a well-defined magmatic foliation. The presence of fractures will significantly decrease the thermal conductivity of the sample (Hyndman et al., 1984; Dick, Erzinger, Stokking, et al., 1992), and preferred plagioclase orientation might be responsible for the other low conductivity value. Finally, these lower values for the altered samples suggest that the heat flux through altered zones is mostly controlled by convective rather than conductive heat flow.

Electrical Resistivity

Measurements of the electrical resistivity of oceanic rocks are useful for the interpretation of oceanic electromagnetic induction data and borehole resistivity logs as well as for providing a measure of the type of porosity in the rock. Natural electromagnetic induction data

Table 20. Summary of thermal conductivity data from Hole 894G.

Core, section, interval (cm)	Piece number	Depth (mbsf)	TC (W/m°C)	Comments
147-894G-				
2R-2, 95–104	15	31.05	1.838	Plagioclase-olivine phyric basalt
2R-3, 30–46	5	31.85	2.022	Altered olivine gabbro
2R-3, 114–122	14	32.69	2.319	Olivine gabbro
3R-1, 1–7	1	38.20	1.853	Plagioclase-olivine phyric basalt
4R-1, 113–122	16	46.13	2.229	Moderately altered medium-grained gabbronorite
4R-2, 80–92	11	47.14	2.181	Moderately altered medium-grained gabbronorite
6R-1, 82–92	8	55.62	2.007	Moderately altered medium-coarse grained gabbronorite
6R-2, 71–88	6	56.94	2.319	Olivine gabbronorite
7R-1, 75–84	13	65.55	2.197	Medium-coarse grained olivine gabbronorite
7R-2, 1–15	1	66.20	2.075	Fractured olivine gabbronorite
8R-1, 7–17	2	68.57	2.120	Fractured moderately altered gabbronorite
8R-1, 140–150	11	69.90	2.287	Highly altered gabbronorite
9R-2, 97–107	5D	76.62	2.273	Medium-grained olivine gabbronorite
9R-3, 47–56	4	77.38	2.243	Altered olivine gabbronorite
9R-4, 50–60	4	78.83	2.266	Slightly altered olivine gabbronorite
10R-1, 60–72	11B	79.70	2.365	Medium-grained olivine gabbronorite (slight magmatic foliation)
11R-1, 109–119	16	85.19	2.153	Highly altered olivine gabbronorite (veins)
11R-2, 115–122	12	86.71	2.389	Medium-grained olivine gabbronorite
12R-2, 38–45	4E	95.64	2.298	Slightly altered olivine gabbronorite
12R-2, 87–98	9	96.13	2.323	Medium-coarse grained olivine gabbronorite (slight magmatic foliation)
12R-5, 76–89	9	100.49	2.151	Coarse-grained gabbronorite (well-defined magmatic foliation)
13R-1, 125–136	14	104.65	2.393	Medium-coarse grained gabbronorite (slight magmatic foliation)
13R-2, 87–97	8	105.77	2.372	Medium-grained gabbronorite (magmatic foliation)
13R-3, 16–24	1B	106.39	2.434	Medium-grained gabbronorite
16W-1, 38–47	7	123.18	2.312	Coarse-grained olivine bearing gabbronorite
17R-1, 115–127	14	126.95	2.395	Medium-grained gabbronorite
19R-1, 29–39	7	140.79	2.356	Medium-grained gabbronorite
19R-1, 70–79	12	141.20	1.660	Fractured phyric basalt with sulfides and olivine phenocrysts
19R-1, 85–95	13	141.35	2.153	Coarse-grained highly altered gabbronorite
20R-1, 53–63	10	146.13	2.323	Medium-grained gabbronorite with large orthopyroxene oikocrysts
20R-2, 9–20	2	147.19	2.306	Coarse-medium grained moderately altered gabbronorite with oxides
20R-3, 51–62	9	149.11	2.331	Medium-grained gabbronorite with coarse-grained patches
		Mean	2.217	
		Std dev	0.180	

previously have been used to estimate the resistivity beneath the ocean floor (Cox et al., 1970; Poehls and Von Herzen, 1975) and beneath oceanic islands (Hermance and Garland, 1968; Klein, 1971; Hermance, 1973), but direct resistivity values of lower oceanic crust samples with known compositions are sparse (Hyndman and Drury, 1977; Cann and Von Herzen, 1983; Hyndman et al., 1984; Smith and Vine, 1987; Pezard et al., 1991). During Leg 147, the resistivities of a series of altered and unaltered samples were obtained at atmospheric pressure and temperature.

Electrical resistivity measurements performed in several water-saturated minicores show a strong inverse correlation with porosity, which suggests that ionic pore fluid conduction dominates in these samples. Values ranging from 10,700 Ωm to 20 Ωm fall within the range previously measured for this type of oceanic rocks (Hyndman and Drury, 1977; Robinson, Von Herzen et al., 1989).

Previous workers (Hyndman and Drury, 1977; Kirkpatrick, 1979; Cann and Von Herzen, 1983; Hyndman et al., 1984; Smith and Vine, 1987; Broglia and Moos, 1988; Pezard et al., 1991) have examined the relationship between porosity and resistivity in oceanic basalts, gabbros and peridotites using Archie's Law:

$$R_0 = (a\, R_w) \,/\, (\phi m),$$

where R_0 is the measured resistivity of the saturated sample, R_w is the resistivity of the pore fluid, ϕ is the porosity expressed as a ratio of the rock volume, a is an empirical constant, and m is the cementation exponent. To compare our results with those of previous workers, we plot the formation factor (R_0/R_w) vs. porosity as a ratio where R_w equals 0.20 Ωm, the resistivity of seawater at laboratory temperature (Fig. 73). Rearranging Archie's Law,

$$m = \log(a\, R_w/R_0) \,/\, \log(\phi),$$

we can see that m is the slope on a log-log plot and a is a shift of the line, which is allowed to vary to best fit the data. The most recent studies (Broglia and Moos, 1988; Pezard et al., 1991) attach no significance to the value of a, whereas earlier studies (Hyndman et al., 1984; Smith and Vine, 1987) held a fixed at 1, a common value for sedimentary rocks. The best fit line gives m a value of 1.23 and a a value of 4.8, as compared with an m of 1.08 and an a of 8.04 for the gabbros drilled at Site 735 (Pezard et al., 1991). The determination of m may be useful in that theoretical modelling using arrays of resistors (Shankland and Waff, 1974) suggests m should be 1 for conduction through narrow fluid-filled cracks, whereas m should be 2 for conduction through spherical, randomly connected pores. Problems with this type of analysis include the effects of more highly conductive "bound water" or highly conductive minerals lining the pore spaces. Such problems have been addressed with more complex models for sedimentary rocks (Serra, 1984) and for oceanic gabbros from Site 735 (Pezard et al., 1991). A plot of m vs. depth (Fig. 74) shows a trend towards higher computed m values with depth. This could be caused by a change in porosity type with depth, a decrease in the abundance of clay minerals lining the pore spaces with depth, or a decrease in the salinity of the pore fluid with depth, although the samples were dried and resaturated with seawater before measurements. There is no apparent trend in measured resistivity values with depth.

DOWNHOLE MEASUREMENTS

Because of the poor hole conditions in all of the Leg 147 boreholes, downhole logging was restricted to a short interval of Hole 894G only. Logging was done in two phases, the first immediately after drilling the hole and the second at the end of the leg (see "Operations" section, this chapter).

In the first phase of logging, a stripped-down version of the "quad-combo" was run, consisting of the long-spacing sonic digital tool (LSS-SDT), the high-temperature lithodensity tool (HLDT), the natural gamma-ray spectrometry tool (NGT) and the temperature logging tool (TLT). The borehole televiewer (BHTV) also was de-

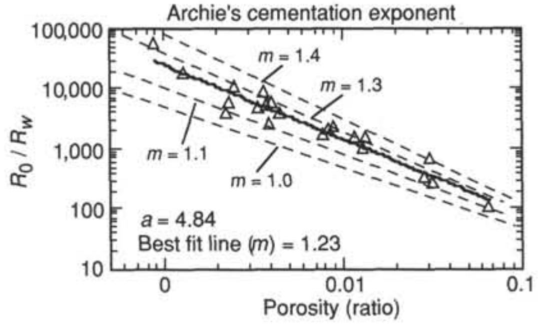

Figure 73. Resistivity-porosity relationship for the crystalline rocks from Hole 894G.

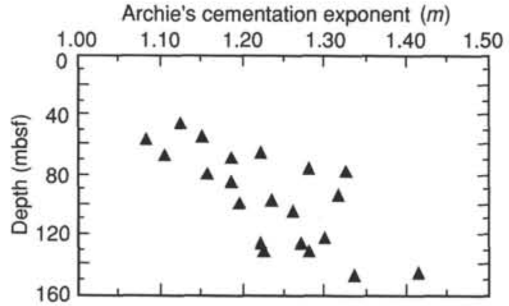

Figure 74. Archie's cementation exponent *m* vs. depth for the crystalline rocks from Hole 894G.

ployed, but the tool failed while being lowered through the pipe, and the run was aborted. The LSS-SDT-NGT-HLDT-TLT combination was run without a radioactive source in the HLDT, because hole conditions were judged to be too bad to risk deploying a source. The HLDT tool was retained to get some information (from its single-arm caliper) about hole size and roughness before a decision was made concerning the more delicate tools, such as the Formation MicroScanner (FMS).

For the first phase of logging, the pipe was held at 34 mbsf. The bottom of the pipe was detected by the sonic tool at a loggers' depth of 3062 m below rig floor (mbrf), giving a logging mud line depth of 3028 mbrf. Depths on all of the above logs are therefore shifted by 3028 m to yield depths in mbsf. The main log with the LSS-SDT-NGT-HLDT-TLT string was recorded from 90 to 6 mbsf, of which the interval 90 mbsf to 34 mbsf was in open hole, 34 mbsf to 33 mbsf was through pipe, and 33 mbsf to 6 mbsf was through pipe in cased hole. A repeat section was recorded from 63 mbsf to 35 mbsf entirely in open hole. A ledge at approximately 90 mbsf prevented the lowermost 60 m or so of Hole 894G from being logged.

Data obtained from the NGT are shown in Figure 75 for the interval 90 mbsf to 6 mbsf. The standard gamma-ray (SGR) curve is a record of the total gamma-ray count, whereas the computed gamma-ray (CGR) is a computed value of gamma-ray counts minus the contribution of uranium. U, Th, and K abundances are computed from the counts from different windows (see "Explanatory Notes" chapter, this volume; Figs. 75C, -D, -E). The negative values in some of the logs indicate that further processing is required to correct for hole conditions.

The HLDT single-arm caliper data (Fig. 76) show that the borehole is extremely rough, with rapid changes in diameter. Much of the hole is close to, or in excess of, the maximum width of the caliper (i.e., 18 in. [45 cm] or greater).

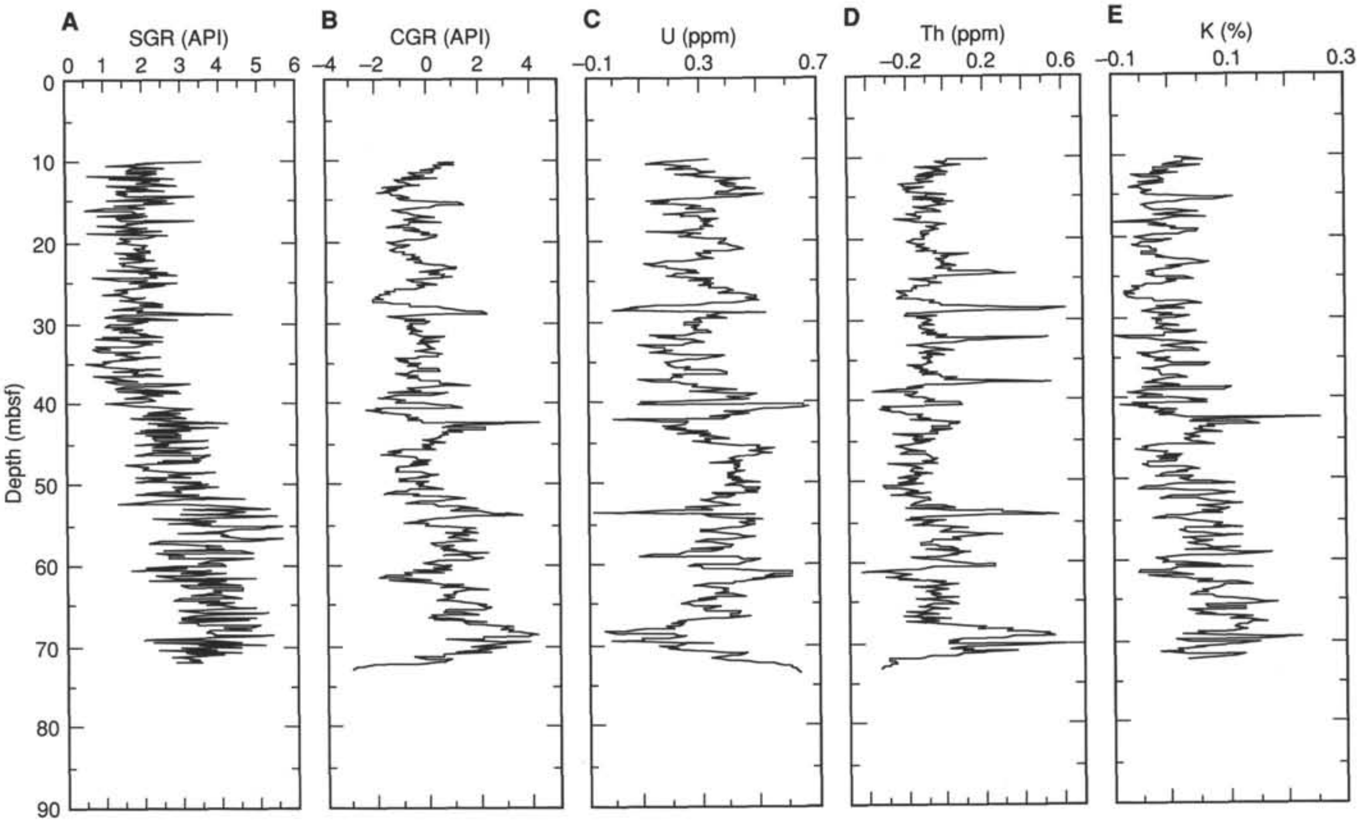

Figure 75. NGT data, Hole 894G: **A.** Standard gamma ray (SGR). **B.** Computed gamma ray (CGR). **C.** U content. **D.** Th content. **E.** K content.

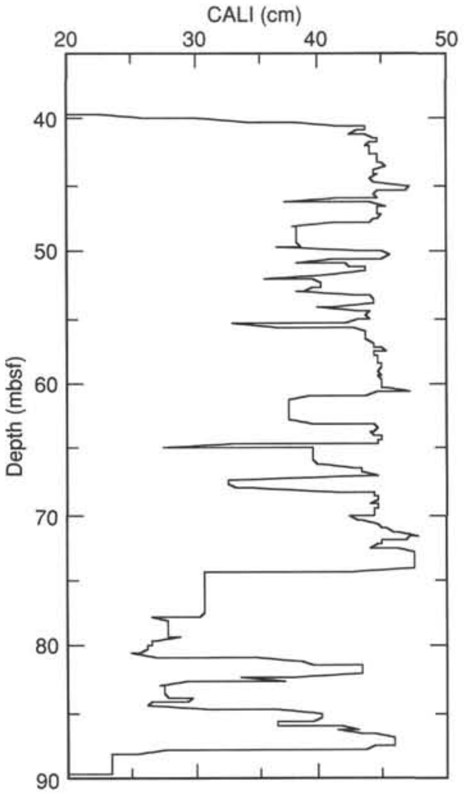

Figure 76. HLDT caliper data for Hole 894G.

The LSS-SDT recorded data from 90 mbsf to 6 mbsf; however, the data are of extremely poor quality and require further processing to compensate for the large and irregular hole diameter. The unprocessed data are not shown here.

The TLT data from the slow thermistor as a function of depth (Fig. 77) show that the water temperature is approximately 1.2°C at mud line and approximately 2°C at 90 mbsf. The fast-response thermistor did not work. The depth conversion of the pressure data used the formula:

$$z = (p - 4267)\, 0.67475 + 7.47$$

where z is in mbsf and p the recorded pressure in psi. This pressure coefficient of 0.67475 assumes a density of hole seawater of 1.0422, corresponding to a salinity of 3.5%, pressure of 305 bars, and temperature of about 0°C. The pressure offset of 4267 psi corresponds to the pressure that was recorded when the tool was held for 3 min at the expected mud line at the logging depth of 3034 mbrf. The depth offset of 7.47 m corresponds to the difference of 6 m between 3034 mbrf and the real mud line, plus the sensor offset of 1.47 m with the logging depth. The scattered temperature values at 7.47 mbsf are probably a consequence of the slowness of the response of the sensor.

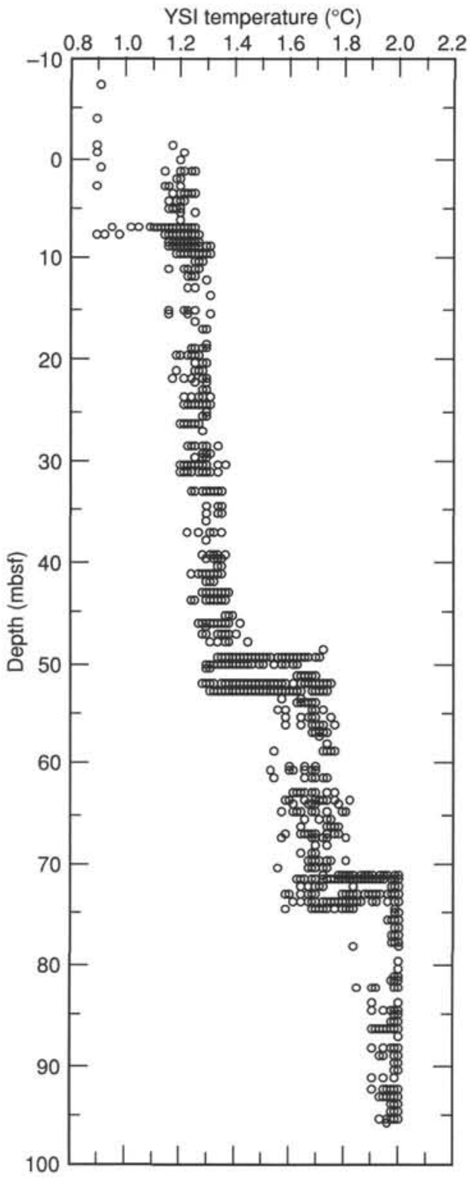

Figure 77. TLT data for Hole 894G.

Because the HLDT caliper data (Fig. 76) showed that most of the borehole was significantly larger than the 15 in. (38 cm) maximum diameter of the FMS calipers, we decided that it would not be productive to deploy the FMS tool string (general purpose inclinometry tool [GPIT]-micro electrical scanning tool [MEST]-NGT-TLT), and the first phase of logging was terminated. When it became clear, however, that the BHTV could not be made to work on board ship, and that no logging would be possible at any of the holes at Site 895, we decided to make a further attempt at obtaining some FMS data from Hole 894G. It had become obvious from structural studies of the Site 894 cores (see "Structure" section, this chapter) that acquisition of oriented structural data from downhole images (and hence opportunity to reorient structural measurements from the core: see "Structural Geology" section, "Explanatory Notes" chapter, this volume) would be crucial to models for the spreading geometry of the East Pacific Rise and formation of Hess Deep.

Hole 894G was reentered after drilling operations at Site 895 had ceased, and the FMS (GPIT-MEST-NGT-TLT) tool string was deployed. The heave compensator was not used because of the shallow depths involved. Five logging passes were recorded successfully between 82 mbsf and 45 mbsf. We were unable to get below the ledge at 82 mbsf that we had penetrated in the first phase of logging (Fig. 76). At the end of the fifth pass, we found that the calipers would not retract properly, and we were only able to recover the FMS tool by jamming it into the bottom of the pipe and using a Kinley cutter (see "Operations" section, this chapter).

Correlation of the five passes with each other and to the data from the previous phase of logging was difficult because of the extremely low gamma-ray values encountered, the lack of heave compensation, and the relatively high logging speeds used. Furthermore, a difference of approximately 10.5 m was recognized between the drillers' depths and loggers' depths. Drillers' depths to drill pipe and mud line, respectively, were 3039 mbrf and 3035 mbrf (the mud-line depth is slightly greater than during the first logging phase because of the increased elevation of the rig floor), in contrast to the loggers' depths of 3029 mbrf to the bottom of the pipe (the depth at which the tool became stuck), and hence 3025 mbrf to the mud line. The logs illustrated in Figures 78, 79, and 80 are therefore shifted to depths in mbsf by the subtraction of 3025 m.

Although, as expected, the FMS data are of poor quality overall, the GPIT data (Fig. 78) show that the calipers were not at maximum extent (~15 in., or ~38 cm) for the entire logged interval. Examination of the FMS images shows that the pads made sufficient contact over several short sections of the borehole for some low-resistivity features (almost certainly fractures) to be recognizable. Further processing and careful depth matching are necessary, however, before any geological interpretation of the FMS images can be made.

Differences of up to 7 cm between the two borehole diameters (e.g., 69 to 72 mbsf) at constant pad azimuth (Fig. 78) suggest that the borehole may be elliptical in cross section. Such elongations are often induced by unequal in-situ horizontal stresses; once again, however, further analysis of the data from all five passes is necessary before the significance of this observation can be established. Magnetic field data (Fig. 79) and hole orientation data (Fig. 80) are consistent between passes and show the magnetic field to be inclined at 19°, and a hole inclined at 4° toward the west–southwest.

REFERENCES*

Allan, J.F., Batiza, R., Perfit, M.R., Fornari, D.J., and Sack, R.O., 1989. Petrology of lavas from the Lamont seamount chain and adjacent East Pacific Rise, 10°N. *J. Petrol.,* 30:1245–1298.

Beiersdorf, H., and Natland, J.H., 1983. Sedimentary and diagenetic processes in the Central Panama Basin since the late Miocene: the lithology and composition of sediments from Deep Sea Drilling Project Sites 504 and 505. *In* Cann, J.R., Langseth, M.G., Honnorez, J., Von Herzen, R.P., White, S.M., et al., *Init. Repts. DSDP,* 69: Washington (U.S. Govt. Printing Office), 343–383.

Berger, W.H., and Winterer, E.L., 1974. Plate stratigraphy and the fluctuating carbonate line. *In* Hsü, K.J., and Jenkyns, H.C. (Eds.), *Pelagic Sediments on Land and Under the Sea.* Spec. Publ. Int. Assoc. Sedimentol., London (Blackwell Scientific), 11–48.

Berthé, D., Choukrome, P., and Jegouzo, P., 1979. Orthogenesis, mylonite and non-coaxial deformation and granites: the examples of South American shear zone. *J. Struct. Geol.,* 1:31–42.

Birch, F., 1960. The velocity of compressional waves in rocks to 10 kilobars, 1. *J. Geophys. Res.,* 65:1083–1102.

————, 1961. The velocity of compressional waves in rocks to 10 kilobars, 2. *J. Geophys. Res.,* 66:2199–2224.

Birch, F., and Bancroft, D., 1940. The effect of pressure on the rigidity of rocks. *J. Geol.,* 46:59–87, 113–141.

Bird, D.K., Manning, C.E., and Rose, N.M., 1988. Hydrothermal alteration of Tertiary layered gabbros, East Greenland. *Am. J. Sci.,* 288:405–457.

Bird, D.K., Rogers, R.D., and Manning, C.E., 1986. Mineralized fracture systems of the Skaergaard intrusion. *Medd. Groenl.: Geosci.,* 16:68.

Blum, N., 1991. Structure and composition of oceanic crust and upper mantle exposed in Hess Deep of the Galapagos Microplate (Equatorial East Pacific) [Ph.D.dissert.]. Univ. (TH) Karlsruhe, Germany.

Borradaile, G.J., 1988. Magnetic susceptibility, petrofabrics and strain. *Tectonophysics,* 156:1–20.

Borradaile, G.J., Keeler, W., Alford, C., and Sarvas, P., 1987. Anisotropy of magnetic susceptibility of some metamorphic minerals. *Phys. Earth Planet. Inter.,* 48:161–166.

Broglia, C., and Moos, D., 1988. *In-situ* structure and properties of 110-MA crust from geophysical logs in DSDP Hole 418A. *In* Salisbury, M.H., Scott, J.H., et al., *Proc. ODP, Sci. Results,* 102: College Station, TX (Ocean Drilling Program), 29–47.

Cann, J.R., and Von Herzen, R.P., 1983. Downhole logging at Deep Sea Drilling Project Sites 501, 504, and 505, near the Costa Rica Rift. *In* Cann, J.R., Langseth, M.G., Honnorez, J., Von Herzen, R.P., White, S.M., et al., *Init. Repts. DSDP,* 69: Washington (U.S. Govt. Printing Office), 281–300.

Cannat, M., 1991. Plastic deformation at an oceanic spreading ridge: a microstructural study of Site 735 gabbros (southwest Indian Ocean). *In* Von Herzen, R.P., Robinson, P.T., et al., *Proc. ODP, Sci. Results,* 118: College Station, TX (Ocean Drilling Program), 399–408.

Cannat, M., Mével, C., and Stakes, D.S., 1991. Stretching of the deep crust at the slow spreading SW Indian Ridge. *Tectonophysics,* 190:73–95.

Chester, F.M., Friedman, M., and Logan, J.L., 1985. Foliated cataclasites. *Tectonophysics,* 111:139–146.

Christensen, N.I., 1982. Seismic velocities. *In* Carmichael, R.S. (Ed.), *Handbook of Physical Properties of Rocks:* Boca Raton, FL (CRC Press), 2:1–228.

Clark, S.P. (Ed.), 1966. *Handbook of Physical Constants.* Mem.—Geol. Soc. Am., 97.

Cox, C.S., Filloux, J.H., and Larsen, J.C., 1970. Electromagnetic studies of ocean currents and electrical conductivity below the ocean floor. *In* Maxwell, A.E. (Ed.), *The Sea* (Vol. 4, Pt. 2): New York (Wiley-Interscience), 637–693.

Day, R., Fuller, M., and Schmidt, V.A., 1977. Hysteresis properties of titanomagnetites: grain-size and compositional dependence. *Phys. Earth Planet. Inter.,* 13:260–267.

Dick, H.J.B., Erzinger, J., Stokking, L.B., et al., 1992. *Proc. ODP, Init. Repts.,* 140: College Station, TX (Ocean Drilling Program).

Dick, H.J.B., Robinson, P.T., and Meyer, P.S., 1992. The plutonic foundation of a slow-spreading ridge. *In* Duncan, R., and Rea, D. (Eds.), *The Indian Ocean: A Synthesis of Results from the Ocean Drilling Program.* Am. Geophys. Union, Geophys. Monogr., 70:1–39.

Dunlop, D.J., and Prevot, M., 1982. Magnetic properties and opaque mineralogy of drilled submarine intrusive rocks. *Geophys. J. R. Astron. Soc.,* 69:763–802.

Eckhardt, J.-D., 1992. Geochemische Untersuchungen an jungen Sedimenten von der Galapagos-Mikroplatte: Hydrothermale und stratigraphisch signifikante Signale [Ph.D. dissert.]. Univ. (TH) Karlsruhe, Germany.

Fox, P.J., and Opdyke, N.D., 1973. Geology of the oceanic crust: magnetic properties of oceanic rocks. *J. Geophys. Res.,* 78:5139–5154.

Francheteau, J., Armijo, R., Cheminee, J.L., Hekinian, R., Lonsdale, P., and Blum, N., 1990. 1 Ma East Pacific Rise oceanic crust and uppermost mantle exposed by rifting in Hess Deep (equatorial Pacific Ocean). *Earth Planet. Sci. Lett.,* 101:281–295.

Gillis, K.M., Thompson, G., and Kelley, D.S., in press. A view of the lower crustal component of hydrothermal systems at the Mid-Atlantic Ridge. *J. Geophys. Res.*

Hamilton, E.L., 1971. Prediction of *in-situ* acoustic and elastic properties of marine sediments. *Geophysics,* 36:266–284.

Harrison, C.G.A., 1987. Marine magnetic anomalies—the origin of the stripes. *Annu. Rev. Earth Planet. Sci.,* 15:505–543.

Hekinian, R., Bideau, D., Francheteau, J., Lonsdale, P., and Blum, N., 1993. Petrology of the East Pacific Rise crust and upper mantle exposed in the Hess Deep (eastern equatorial Pacific). *J. Geophys. Res.,* 98:8069–8094.

Henry, B., and Daly, L., 1983. From qualitative to quantitative magnetic anisotropy analysis: the prospect of finite strain calibration. *Tectonophysics,* 98:327–336.

Hermance, J.F., 1973. An electrical model for the Icelandic crust. *Geophysics,* 38:3.

Hermance, J.F., and Garland, G.D., 1968. Magnetotelluric deep-sounding experiments in Iceland. *Earth Planet. Sci. Lett.,* 4:469–474.

Hrouda, F., 1982. Magnetic anisotropy of rocks and its application in geology and geophysics. *Geophys. Surv.,* 5:37–82.

Hyndman, R.D., Christensen, N.I., and Drury, M.J., 1984. The physical properties of basalt core samples from Deep Sea Drilling Project Leg 78B Hole 395A. *In* Hyndman, R.D., Salisbury, M.H., et al., *Init. Repts. DSDP,* 78 (Pt. 2): Washington (U.S. Govt. Printing Office), 801–810.

Hyndman, R.D., and Drury, M.J., 1976. The physical properties of oceanic basement rocks from deep drilling on the Mid-Atlantic Ridge. *J. Geophys. Res.,* 81:4042–4052.

————, 1977. Physical properties of basalts, gabbros and ultramafic rocks from DSDP Leg 37. *In* Aumento, F., Melson, W.G., et al., *Init. Repts. DSDP,* 37: Washington (U.S. Govt. Printing Office), 395–402.

Iturrino, G.J., Christensen, N.I., Kirby, S., and Salisbury, M.H., 1991. Seismic velocities and elastic properties of oceanic gabbroic rocks from Hole 735B. *In* Von Herzen, R.P., Robinson, P.T., et al., *Proc. ODP, Sci. Results,* 118: College Station, TX (Ocean Drilling Program), 227–244.

---

* Abbreviations for names of organizations and publication titles in ODP reference lists follow the style given in *Chemical Abstracts Service Source Index* (published by American Chemical Society).

Johnson, H.P., and Pariso, J.E., 1993. Variations in oceanic crustal magnetization: systematic changes in the last 160 million years. *J. Geophys. Res.,* 98:435–445.

Kelley, D.S., and Delaney, J.R., 1987. Two-phase separation and fracturing in mid-ocean ridge gabbros at temperatures greater than 700°C. *Earth Planet. Sci. Lett.,* 83:53–66.

Kelley, D.S., Gillis, K.M., and Thompson, G., in press. Fluid evolution in submarine magma-hydrothermal systems at the Mid-Atlantic Ridge. *J. Geophys. Res.*

Kent, D.V., Honnorez, B.M., Opdyke, N.D., and Fox, P.J., 1978. Magnetic properties of dredged oceanic gabbros and source of marine magnetic anomalies. *Geophys. J. R. Astron. Soc.,* 55:513–537.

Kikawa, E., and Ozawa, K., 1992. Contribution of oceanic gabbros to sea-floor spreading magnetic anomalies. *Science,* 258:796–799.

Kikawa, E., and Pariso, J.E., 1991. Magnetic properties of gabbros from Hole 735B, Southwest Indian Ridge. *In* Von Herzen, R.P., Robinson, P.T., et al., *Proc. ODP, Sci. Results,* 118: College Station, TX (Ocean Drilling Program), 285–308.

Kirkpatrick, R.J., 1979. Results of downhole geophysical logging Hole 396B, DSDP Leg 46. *In* Dmitriev, L., Heirtzler, J., et al., *Init. Repts. DSDP,* 46: Washington (U.S. Govt. Printing Office), 401–407.

Klein, D.P., 1971. Geomagnetic time variations on Hawaii Island and mantle electrical conductivity. *Eos,* 52:824.

Lonsdale, P., 1988. Structural pattern of the Galapagos microplate and evolution of the Galapagos triple junction. *J. Geophys. Res.,* 93:13551–13574.

MacLeod, C.J., and Rothery, D.A., 1992. Ridge axial segmentation in the Oman ophiolite: evidence from along-strike variations in the sheeted dyke complex. *In* Parson, L.M., Murton, B.J., and Browning, P. (Eds.), *Ophiolites and Their Modern Oceanic Analogues.* Geol. Soc. Spec. Publ. London, 60:39–64.

Manning, C.E., and Bird, D.K., 1986. Hydrothermal clinopyroxenes of the Skaergaard intrusion. *Contrib. Mineral. Petrol.,* 92:437–447.

McFadden, P.L., and Merrill, R.T., 1975. Geomagnetic secular variation over the past 5 m.y. *Rev. Geophys. Space Phys.,* 13:687–708.

Merrill, R.T., and McElhinny, M.W., 1983. *The Earth's Magnetic Field: Its History, Origin, and Planetary Perspective:* London (Academic Press).

Mével, C., and Cannat, M., 1991. Lithospheric stretching and hydrothermal processes in oceanic gabbros from slow-spreading ridges. *In* Peters, T., et al. (Eds.), *Ophiolite Genesis and Evolution of the Oceanic Lithosphere:* Dordrecht (Kluwer), 293–312.

Moore, D.M., and Reynolds, R.C., Jr., 1989. *X-ray Diffraction and the Identification and Analysis of Clay Minerals:* Oxford (Oxford Univ. Press).

Moore, T.C., Jr., Heath, G.R., and Kowsmann, R.O., 1973. Biogenic sediments of the Panama Basin. *J. Geol.,* 81:458–472.

Moos, D., and Zoback, M.D., 1983. In-situ measurements of the properties of fractured crystalline rocks. *J. Geophys. Res.,* 80:2345–2354.

Morel, J.M., and Hekinian, R., 1980. Compositional variation of volcanics along segments of recent spreading ridges. *Contrib. Mineral. Petrol.,* 72:425–436.

Murdmaa, I.O., and Rozanova, T.V., 1976. Hess Deep bottom sediments. *In Geological-Geophysical Researches in the Southeastern Part of the Pacific Ocean:* Moscow (Nauka), 252–260. (in Russian)

Nagata, T., 1967. Principles of the ballistic magnetometer for the measurements of remanence. *In* Collinson, D.W., Creer, K.M., and Runcorn, S.K. (Eds.), *Methods in Palaeomagnetism:* Amsterdam (Elsevier).

Natland, J.H., 1980. Effect of axial magma chambers beneath spreading centers on the composition of basaltic rocks. *In* Rosendahl, B.R., Hekinian, R., et al., *Init. Repts. DSDP,* 54: Washington (U.S. Govt. Printing Office), 833–850.

————, 1989. Partial melting of a lithologically heterogeneous mantle: inferences from crystallization histories of magnesian abyssal tholeiites from the Siqueiros Fracture Zone. *In* Saunders, A.D., and Norry, M.J. (Eds.), *Magmatism in the Ocean Basins.* Geol. Soc. Spec. Publ. London, 42:41–70.

Natland, J.H., Adamson, A.C., Laverne, C., Melson, W.G., and O'Hearn, T., 1983. A compositionally nearly steady-state magma chamber at the Costa Rica Rift: evidence from basalt glass and mineral data, Deep Sea Drilling Project Sites 501, 504, and 505. *In* Cann, J.R., Langseth, M.G., Honnorez, J., Von Herzen, R.P., White, S.M., et al., *Init. Repts. DSDP,* 69: Washington (U.S. Govt. Printing Office), 811–858.

Nehlig, P., and Juteau, T., 1988. Flow porosities, permeabilities and preliminary data on fluid inclusions and fossil thermal gradients in the crustal sequence of the Sumail ophiolite (Oman). *Tectonophysics,* 151:199–221.

Nicolas, A., Reuber, I., and Benn, K., 1988. A new magma chamber model based on structural studies in the Oman ophiolite. *Tectonophysics,* 151:87–105.

O'Connell, R.J., and Budianski, B., 1974. Seismic velocities in dry and saturated cracked solids. *J. Geophys. Res.,* 79:5412–5426.

Pariso, J.E., and Johnson, H.P., in press. Do oceanic gabbros contribute to marine magnetic anomalies? Magnetic properties and downhole magnetic measurements from ODP Hole 735B at the Southwest Indian Ridge. *J. Geophys. Res.*

Pezard, P.A., Howard, J.J., and Goldberg, D., 1991. Electrical conduction in oceanic gabbros, Hole 735B, Southwest Indian Ridge. *In* Von Herzen, R.P., Robinson, P.T., et al., *Proc. ODP, Sci. Results,* 118: College Station, TX (Ocean Drilling Program), 323–332.

Poehls, K.A., and Von Herzen, R.P., 1975. Electrical conductivity structure in the northwest Atlantic. *Eos,* 56:451.

Prell, W.L., Gardner, J.V., et al., 1982. *Init. Repts. DSDP,* 68: Washington (U.S. Govt. Printing Office).

Robertson, E.C., and Peck, D.L., 1974. Thermal conductivity of vesicular basalt from Hawaii. *J. Geophys. Res.,* 79:4875–4888.

Robinson, P.T., Von Herzen, R., et al., 1989. *Proc. ODP, Init. Repts.,* 118: College Station, TX (Ocean Drilling Program).

Rudnik, G.B., 1976. Magmatic and metamorphic rocks in Hess Deep. *In Geological-Geophysical Research in the Southeastern Part of the Pacific Ocean:* Moscow (Nauka), 116–125. (in Russian)

Schmitz, W., Singer, A., Bäcker, H., and Stoffers, P., 1982. Hydrothermal serpentine in a Hess Deep sediment core. *Mar. Geol.,* 46:M17–M26.

Serra, O., 1984. *Fundamentals of Well Log Interpretation* (Vol. 1): *The Acquisition of Logging Data:* Amsterdam (Elsevier).

Shankland, T.J., and Waff, H.S., 1974. Conductivity in fluid-bearing rocks. *J. Geophys. Res.,* 79:4863–4868.

Smith, G.C., and Vine, F.J., 1987. Seismic velocities in basalts from CCSP Drill Holes CY-2 and CY-2a at Agrokipia Mines, Cyprus. *In* Robinson, P.T., Gibson, I.L., and Panayioutou, A. (Eds.), *Cyprus Crustal Study Project: Initial Report, Holes CY-2 and CY-2a.* Geol. Surv. Can., 339–346.

Stakes, D., Mével, C., Cannat, M., and Chaput, T., 1991. Metamorphic stratigraphy of Hole 735B. *In* Von Herzen, R.P., Robinson, P.T., et al., *Proc. ODP, Sci. Results,* 118: College Station, TX (Ocean Drilling Program), 153–180.

Toksöz, M.N., Cheng, C.H., and Timur, A., 1976. Velocities of seismic waves in porous rocks. *Geophysics,* 41:621–645.

Tullis, J., and Yund, R.A., 1987. The brittle ductile transition in feldspathic rocks. *Eos,* 68:1464.

Usselman, T.M., and Hodge, D.S., 1978. Thermal control of low-pressure fractionation processes. *J. Volcanol. Geotherm. Res.,* 4:265–281.

Uyeda, S., Fuller, M.D., Belshé, J.C., and Girdler, R.W., 1963. Anisotropy of magnetic susceptibility of rocks and minerals. *J. Geophys. Res.,* 68:279–291.

van Andel, T.H., Heath, G.R., et al., 1973. *Init. Repts. DSDP,* 16: Washington (U.S. Govt. Printing Office).

Verwey, E.J.W., and Haayman, P.W., 1941. Electronic conductivity and transition point in magnetite. *Physica,* 8:979–982.

Zijderveld, J.D.A., 1967. AC demagnetization of rocks: analysis of results. *In* Collinson, D.W., Creer, K.M., and Runcorn, S.K. (Eds.), *Methods in Palaeomagnetism:* New York (Elsevier), 254–286.

Ms 147IR-103

NOTE: For all sites drilled, core-description forms (barrel sheets) and core photographs have been reproduced on coated paper and can be found in Section 3, beginning on page 163. Thin-section data are given in Section 4, beginning on page 309. Conventional-log and FMS data can be found in CD-ROM form (back pocket).

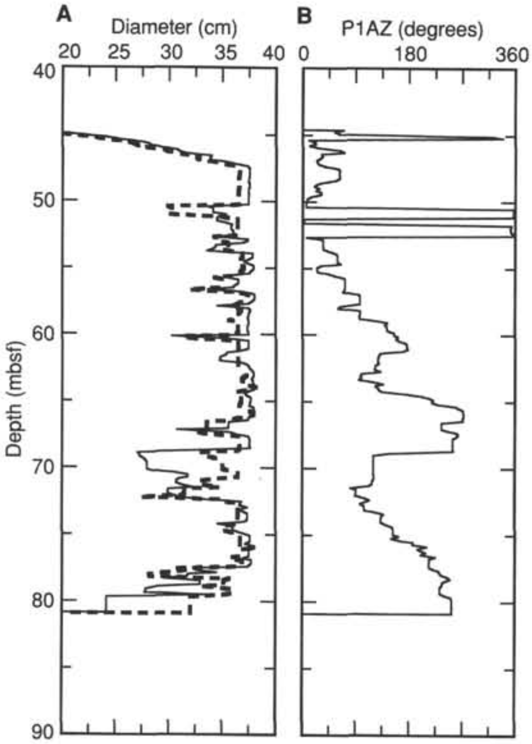

Figure 78. FMS caliper data (second pass) for Hole 894G: **A.** C1 (solid line) and C2 (broken line) orthogonal borehole diameters. **B.** Pad 1 azimuth.

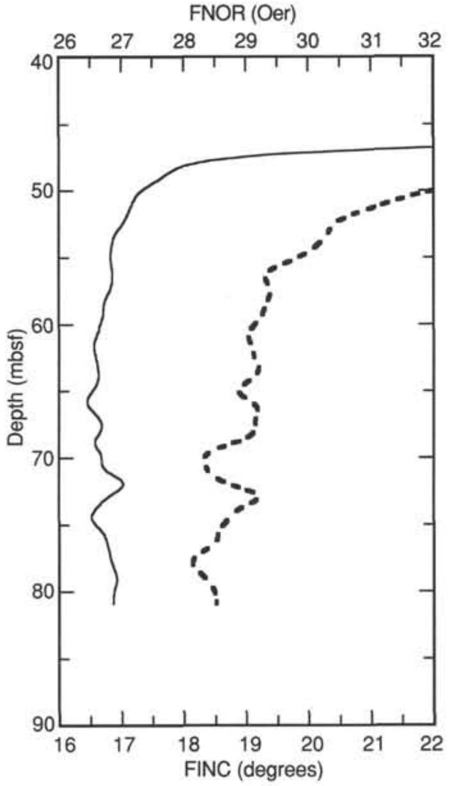

Figure 79. FMS downhole magnetic data (second pass) for Hole 894G: azimuth (FINC, broken line) and total moment (FNOR, solid line) of the magnetic field. The data above 55 mbsf are influenced by the casing.

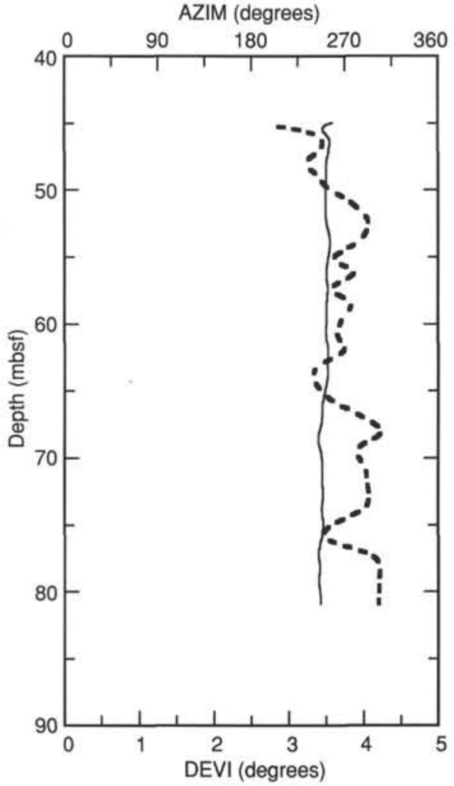

Figure 80. FMS inclinometry data (second pass) for Hole 894G: hole deviation (DEVI, broken line) and azimuth (AZIM, solid line).

Hole 894G: Natural Gamma Ray Log Summary